COMPARATIVE ANALYSIS OF METHODS FOR CALCULATING WHOLE BODY ANGULAR MOMENTUM

With special reference to body segment inertial parameters

Sakari Vekki

Master`s Thesis in Biomechanics
Faculty of Sport and Health Sciences
University of Jyväskylä
Autumn 2024
Supervisors: Mikko Virmavirta & Janne Avela

TIIVISTELMÄ

Vekki, S. 2024. Comparative analysis of methods for calculating whole body angular momentum: with special reference to body segment inertial parameters. Liikuntatieteellinen tiedekunta, Jyväskylän yliopisto, Biomekaniikan pro gradu -tutkielma, 78 s., 4 liitettä.

Koko kehon pyörimismäärän määrittäminen on olennainen osa biomekaniikkaa. Sitä voidaan hyödyntää laajasti, alkaen monimutkaisten akrobaattisten liikkeiden analysoinnista aina kävelyn aikana tapahtuvan tasapainon säätelyn ymmärtämiseen. Koko kehon pyörimismäärän laskentaan on olemassa kaksi erilaista lähestymistapaa: kinematiikkaan perustuva menetelmä sekä impulssiin perustuva menetelmä. Kummallakin näistä menetelmistä on omat virhelähteensä, ja ne ovat myös riippuvaisia kehon hitausominaisuuksien arvioista. Menetelmien laajasta käytöstä huolimatta niiden välisiä eroja ei ole vielä tutkittu. Tämän tutkimuksen tarkoituksena oli selvittää mahdollisia eroja kinematiikka- ja impulssimenetelmien kautta lasketuissa koko kehon pyörimisliikemäärissä.

Tutkimuksessa kaksi miespuolista telinevoimistelijaa suorittivat erilaisia ponnistavia liikkeitä, joiden ajalta koko kehon pyörimismäärää laskettiin sagittaalitasossa. Suoritusten analysointia varten dataa kerättiin Vicon liikekaappausjärjestelmää hyödyntäen 16:lla kameralla 200 Hz:n taajuudella yhdessä AMTI voimalevyn kanssa. Kolmea regressioyhtälöihin perustuvaa kehon hitausominaisuuksia arvioivaa segmenttimallia käytettiin yhdessä kinematiikka- ja impulssimenetelmien kanssa arvioimaan menetelmien välisiä eroja koko kehon pyörimismäärän laskennassa.

Tutkimuksen tulokset osoittivat, että kinematiikka- ja impulssimenetelmillä lasketuissa koko kehon pyörimismäärissä on tilastollisesti merkittäviä eroja. Lisäksi segmenttimallien väliset erot vaikuttivat tilastollisesti laskettuihin arvoihin. Kuitenkin laskentamenetelmän valinnalla havaittiin olevan suurempi vaikutus koko kehon pyörimismäärän laskennallisiin arvoihin kuin segmenttimallin valinnalla. Kinematiikkamenetelmän tuottamat pyörimismäärän arvot olivat johdonmukaisempia eri segmenttimallien välillä verrattuna impulssimenetelmän tuottamiin arvoihin. Nämä tulokset viittaavat siihen, että kinematiikkamenetelmä saattaa olla impulssimenetelmää soveltuvampi tapa arvioimaan koko kehon pyörimismäärää biomekaniikan tutkimuksissa.

Asiasanat: pyörimismäärä, segmenttimalli, kinematiikka

ABSTRACT

Vekki, S. 2024. Comparative analysis of methods for calculating whole body angular momentum: with special reference to body segment inertial parameters. Faculty of Sport and Health Sciences, University of Jyväskylä, Master's thesis in Biomechanics, 78 pp., 4 appendices.

Quantifying whole body angular momentum (WBAM) is important in many aspects of biomechanics, from analysing the dynamics of complex acrobatic maneuvers to understanding balance in everyday activities such as walking. Two calculation methods – the kinematic method and the impulse method – can be used to determine WBAM. Both methods have inherent sources of error, and they also depend on estimates of inertial properties of body segments. Despite their widespread use, these methods have not been thoroughly compared. The aim of this study was to investigate the potential differences in WBAM values derived from these two computational approaches.

In this study, two male gymnasts performed different jumping tasks where WBAM was calculated in the sagittal plane. Data were collected using a Vicon motion capture system at 200 Hz with 16 cameras together with an AMTI force plate. Three regression equation-based body segment inertial parameter (BSIP) models were used together with the kinematic and the impulse methods to evaluate the differences between these methods in calculating WBAM.

The findings revealed statistically significant differences in WBAM values between the kinematic and impulse methods. Variations between the BSIP models also significantly influenced the WBAM values. However, the choice of calculation method had a larger impact on the WBAM values than the choice of BSIP model. The kinematic method yielded more consistent results between different BSIP models than the impulse method. This suggests that the kinematic method may be more suitable for WBAM assessment in biomechanical research than the impulse method.

Key words: angular momentum, body segment parameters, kinematics

ABBREVIATIONS

2D	two-dimensional
3D	three-dimensional
BSIP	body segment inertial parameter
COM	center of mass
COP	center of pressure
CT	computed tomography
DEXA	dual energy X-ray absorption
GCS	global coordinate system
GRF	ground reaction force
MRI	magnetic resonance imaging
WBAM	whole body angular momentum

CONTENTS

1 INTRODUCTION

Whole body angular momentum (WBAM) is a measure of rotational momentum of the human body. Determination of WBAM is important for analysing the dynamics of activities that involve complex rotations such as gymnastics and diving (Yeadon 2017). It is equally important for understanding the mechanics of balance maintenance in more routine tasks, such as walking (Herr & Popovic 2008).

WBAM can be calculated using two primary methods: the kinematic method and the impulse method (Robertson et al. 2014, 89 - 90). The kinematic method calculates WBAM based on movement of the body segments along with their inertial properties, while the impulse method relies on external forces and moments acting on the body. Each method's effectiveness also depends on the precision of the estimates of the inertial properties of the body segments. Despite their widespread use, the results from these two calculation methods have not been compared, particularly in terms of how each method's inherent sources of error impact the WBAM calculations. This gap in research leaves questions unanswered regarding the reliability of WBAM values across studies. Moreover, the existence of multiple approaches for estimating the inertial properties of body segments adds complexity to the matter.

This study aims to conduct a thorough investigation into how the two computational methods for determining WBAM influence the results when different published estimates of inertial parameters of body segments are used. By analysing the variations in WBAM calculations that originate from different inertial parameter estimations and computational methods, this study seeks to clarify the impact of the methodological choice on the accuracy and comparability of biomechanical analyses regarding WBAM.

2 BODY SEGMENT INERTIAL PARAMETERS

In biomechanical studies focusing on human motion, the human body is commonly modeled as a series of interconnected, rigid segments. This approach overlooks the reality that body segments undergo deformation during movement, but it removes the need to quantify the changes in mass distribution that occur due to tissue deformation and movement of bodily fluids. For kinetic analysis of human movement using rigid body modelling, it's essential to accurately determine the physical characteristics and inertial properties of each body segment. These properties are collectively known as body segment inertial parameters (BSIPs), which include mass, position of center of mass (COM), and mass moment of inertia for each segment of the human body. (Robertson et al. 2014, 63 - 69)

In BSIP models, the human body is conceptualized as being comprised of varying number of segments, typically ranging from 14 to 16. The segments included can be head, trunk, thighs, shanks, feet, upper arms, forearms, and hands, where the trunk can be considered to be either a single segment or subdivided into multiple segments. While these configurations are common, both simpler and more complex models also exist, accommodating different levels of detail and analysis requirements (de Leva 1996; Dempster 1955; Dumas & Wojtusch 2018; Hatze 1980).

BSIPs for the human body can be determined through various methods. Direct measurements of BSIPs have been made on cadavers (Chandler et al. 1975; Clauser et al. 1969; Dempster 1955), but for living subjects the estimates can be made indirectly using methods such as medical imaging (Cheng et al. 2000; de Leva 1996; Dumas et al. 2005), photogrammetry (Ackland et al. 1988; Dumas et al. 2007; R. H. Sanders et al. 2015), geometric modelling (Hatze 1980; Jensen 1978; Yeadon 1990) and dynamic analysis (Chen et al. 2011; Hansen et al. 2014). Generally, regression equations based on these measurements are the more traditional approach to estimate BSIPs, where the assumption is made that the distribution of segmental mass is consistent across a specific population (Dumas & Wojtusch 2018; Robertson et al. 2014, 63 - 69).

The accuracy of BSIP estimates is influenced by factors such as individual's morphology, age and gender (Chambers et al. 2010). BSIP estimations are typically more accurate for older Caucasian males without any pathological conditions, due to this group being the primary focus of most BSIP studies so far (Dumas & Wojtusch 2018). However, recent research has begun to address this gap by publishing inertial parameters for different populations (Cheng et al. 2000;

Cicchella 2020; Ho et al. 2013). BSIP estimations obtained from regression equations contain errors particularly when applied to subjects who are physically different from the sample on which the regressions equations are based on. Hence, it's been recommended that regression equations should not be applied to populations other than the ones from which they were derived from. (Dumas et al. 2007; Durkin & Dowling 2003)

The following chapters explore the different methods for estimating BSIPs, starting from historical cadaver studies to advanced medical imaging and modern scanning techniques. The accuracy and practical implications of each method are considered, so that the reader can gain an overall understanding of the BSIPs used in biomechanics.

2.1 BSIP estimation techniques

Cadaver studies. According to Drillis et al. (1964) the earliest published studies quantifying human BSIPs from cadavers date back to the 19th century. Significant advancements in the field were made in mid-20th century by Dempster (1955), who analysed BSIPs directly from eight complete cadavers. He segmented the cadavers and determined the center of mass, segmental mass, and moment of inertia for each of the segments. From this data, Dempster created tables that demonstrated the segmental masses as proportions of the total body mass, as well as the locations of centers of gravity and lengths of the radii of gyration relative to the lengths of the segments. Subsequent noteworthy studies include those by Clauser et al. (1969) who segmented 13 male cadavers, and Chandler et al. (1975), who measured six male cadavers. To this day, the research conducted by Dempster, Clauser et al., and Chandler et al. remains among the most comprehensive cadaver studies of BSIPs.

Cadaver studies provide a direct method to measure human segment inertial parameters, but they face several obstacles. Acquiring specimens from diverse age and sex groups is challenging, which complicates the generalization of the findings to various populations. Furthermore, combining data from different studies is problematic due to the varied methodologies employed. (Durkin 2008) Additionally, questions have been raised concerning the potential discrepancies between the properties of cadaveric tissues and those of living tissues (Pearsall & Reid 1994). While Pearsall and Reid (1994) note that inertial parameters derived from cadavers have been the foundation for rigid body modelling, the relatively small sample sizes in these

studies limits their ability to capture the extensive diversity in human morphologies. As a result, it remains uncertain how well cadaver based BSIPs can be generalized across different demographic groups, including infants, adolescents, young adults, or individuals from diverse racial backgrounds.

Medical imaging techniques. Medical imaging techniques such as gamma mass scanning, two-dimensional (2D) biplanar X-ray computed tomography (CT), magnetic resonance imaging (MRI), and dual energy X-ray absorption (DEXA) have been recognized as reliable methods for generating subject specific BSIP estimations (Cicchella 2020; Durkin 2008). Gamma mass scanning was used by Zatsiorsky and Seluyanov (1983) to measure BSIPs in 100 young Caucasian males, with a subsequent study by Zatsiorsky et al. (1990a) involving 100 male and 15 female subjects. The 1990 study also developed geometrical models and regression equations for BSIP calculations. Other researchers, such as Erdmann (1997), Reid (1984) and Pearsall et al. (1996) have used CT to assess trunk inertial parameters, where Pearsall et al. (1996) provided information about the BSIPs at the vertebrae level. Measurement of BSIPs using gamma mass scanning and CT imaging is considered highly accurate and reliable, but they are constrained by their expense and the radiation exposure to the subjects, albeit in minimal doses (Durkin 2008). Furthermore, as gamma mass scanning is a 2D imaging technique, it allows the estimation of segment inertial properties in only one plane (Durkin 2008).

Using MRI allows for the acquisition of three-dimensional (3D) mass distribution data from axials scans, with the significant advantage of not exposing participants to radiation (Durkin 2008). It has been utilized in several BSIP studies, such as those by Mungiole and Martin (1990) for adult male athletes, Pearsall et al. (1994) for trunk body segment parameters in males, Cheng et al. (2000) for Chinese males, and Bauer et al. (2007) for children. However, MRI systems are not widely accessible to most researchers, and both the data acquisition and processing are costly and time-consuming, leading some to consider BSIP measurements with MRI impractical (Durkin 2008).

DEXA scanning has been utilized in many studies for the determination of BSIPs in human segments (Costa Moreira et al. 2021; Durkin et al. 2002; Ganley & Powers 2004; Laschowski & McPhee 2016; Rossi et al. 2013; Whittaker et al. 2021; Winter et al. 2018), demonstrating a high degree of accuracy for the method. Similarly with gamma mass scanning, DEXA can be used to determine the BSIPs in a single plane only (Durkin 2008). Main difference between

DEXA and gamma mass scanning is that DEXA allows the measurement of bone and soft tissues separately (Rossi et al. 2013). DEXA has also been considered to be faster to analyse than gamma mass scanning (Rossi et al. 2013). According to Durkin (2008) determination of BSIPs using DEXA is rapid and safe, although some have raised concerns regarding the potential risks associated with low-dose irradiation (Cicchella 2020). Furthermore, Cicchella (2020) has noted that replicating DEXA measurements can be challenging due to the complexities involved in subject positioning.

Photogrammetry and surface scanning. 2D photogrammetry (Baca 1996; McConville et al. 1980; R. H. Sanders et al. 2015; Young et al. 1983) and 3D surface scanning (Kudzia et al. 2022; Lu & Wang 2008; Norton et al. 2002; Pandis & Bull 2017; Peyer et al. 2015; Sheets et al. 2009; Smith & Bull 2018) have also been used to obtain subject specific BSIPs. From these two methods, 3D surface scanning is the more recent one which is often utilized by using laser scanners, where 3D representation of a person's body surface is generated using laser triangulation. This process involves a technique known as Poisson surface reconstruction, where the laser scanners produce a complete triangular mesh of the human body. From this mesh, it's possible to calculate volumes, surface areas, centers of volumes, and inertia tensors of the body segments. (Rossi et al. 2013) An example of segmented 3D body scan used for BSIP calculations is presented in figure 1.

Other surface scanning methods, such as time-of-flight based cameras and structured light projection can also be used to reconstruct human bodies in 3D for BSIP estimations (Kudzia et al. 2022). Challenges associated with both 2D photogrammetry and 3D surface scanning include the necessity to presume the density of the segments. Numerous studies have opted for assuming a uniform density between the segments, relying on values obtained from existing literature (Kudzia et al. 2022; Peyer et al. 2015; Smith & Bull 2018), which can produce further errors in estimation of BSIPs (Ackland et al. 1988).

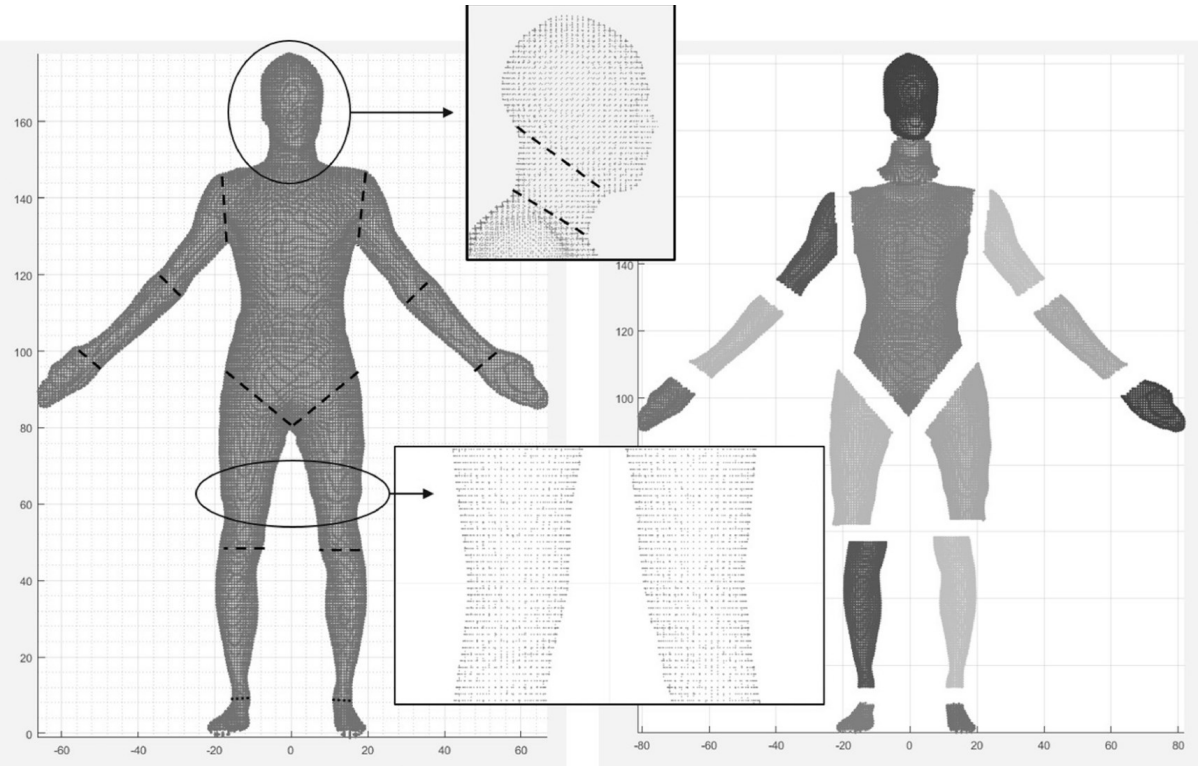

FIGURE 1. Segmented 3D body scan used for BSIP calculations (Smith & Bull 2018).

Geometric models. Geometric models of varying complexity have been developed to reflect differences more accurately in individual morphologies (Durkin 2008). Like other methods for estimating BSIPs, geometric models segment the human body into various parts. Each of these segments, either as a whole or divided into smaller sections, is represented by a specific geometric shape. The BSIPs for these segments are subsequently determined using geometric equations. Generally, these calculations assume of uniform density throughout each segment. Hanavan's (1964) model is one of the original widely used geometrical models of the human body, utilizing a variety of shapes including spheres, ellipsoids, circular cylinders, and frusta. COMs of segments were reported to be predicted within 1.8 cm and moments of inertia within 10 %.

Jensen's (1978) geometrical model, which was based on photogrammetry derived data, modeled the human body as multiple horizontal elliptical slices, and was able to estimate total body mass with an error of 1.8 % according to the authors. Hatze's 1980 development stood as one of the most complex geometric models of the human body, requiring 242 anthropometric measurements to determine BSIPs. Hatze stated that this model is adaptable to a wide range of human morphologies, and that the model would provide BSIPs with maximum error of 5 %, irrespective of the individual's specific characteristics.

In Yeadon's (1990) geometric model, the human body was represented using 40 geometric solids, defined by 95 anthropometric measurements, and density values from Dempster (1955). The maximal error of the total body mass estimates was reported to be 2.3 %, although only three subjects were considered in the study. Zatsiorsky et al. (1990a) created geometric models for human body segments and validated these models against gamma-mass data. This approach required the input of limb circumferences and lengths, with distinct coefficients supplied for male and female populations. These geometric models were found to be 1.5 times less accurate compared to those derived from regression equations using the same dataset.

Nikolova and Dantchev's (2020) contribution to the field is among the more recent advancements, presenting an advanced geometric model based on the anthropometric measurements of 2 435 Bulgarian males aged between 30 and 40 years. This model segments the human body into 20 distinct parts, with each segment assigned a unique density value. Another recent population specific geometrical BSIP model was developed by Jagadale et al. (2022) for female agricultural workers of Central India, where a 14-segment model was developed based on anthropometric data of 180 participants. Figure 2 displays a graphical illustration of the Hatze (1980) model together with the Jagadale et al. (2022) model.

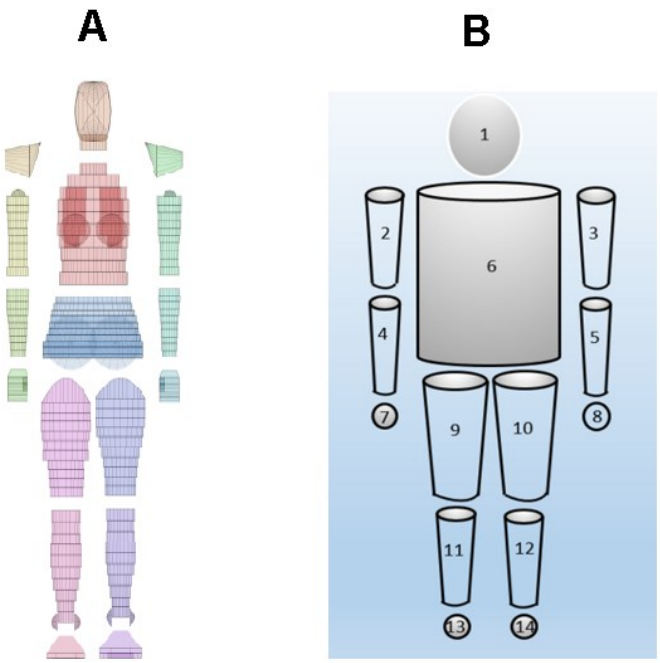

FIGURE 2. A) Hatze (1980) geometric model (edited from Robertson (2013)). B) Jagadale et al. (2022) geometric model.

Regression equations. Regression equations derived from different BSIPs studies are often used to estimate subject specific values in biomechanical studies (Dumas & Wojtusch 2018). Regression equations have been derived from a diverse range of data sources (Clauser et al. 1969; de Leva 1996; Dumas et al. 2007; Dumas & Wojtusch 2018; Durkin & Dowling 2003; V. Zatsiorsky & Seluyanov 1983). These equations are constrained by the limitations inherent in the methods employed to collect the data, and they are primarily applicable to the specific populations from which their data were obtained (Dumas & Wojtusch 2018; Durkin 2008). Regression equations can be linear or non-linear of nature, where non-linear equations should be preferred (Dumas et al. 2007). Nevertheless, due to their convenience, linear regressions such as scaling equations, which rely on overall body mass and segment length, are more frequently used (Dumas et al. 2007). Classically regression equations assume that the COM of the segments is aligned on the axis linking the joint centers, and the principal axes of inertia are also often assumed to be on this axis and on two axes orthogonal to the longitudinal axis (Dumas & Wojtusch 2018). Sometimes, the regression equation-based BSIP models refer the frontal, transverse, and sagittal planes of the segments, even though these planes may not be distinctly defined (Dumas et al. 2007). This ambiguity can lead to uncertainty when applying these BSIP models in 3D analyses withing the traditional coordinate systems of segments (Cappozo et al. 1995; Wu et al. 2002; Wu et al. 2005).

For 3D studies of human motion, the most comprehensive and practical regression equations to date are the original data from Zatsiorsky et al. (1990a) and Zatsiorsky et al. (1990b), as adjusted by de Leva in 1996, and the original photogrammetry-based data from McConville et al. (1980) and Young et al. (1983), as adjusted by Dumas et al. in 2007 and subsequently by Dumas and Wojtusch in 2018. However, while de Leva's adjustments provide moments of inertia in the frontal, sagittal, and horizontal planes, these planes are not always precisely defined for all segments. The distal and proximal endpoints of many segments are designated to lie along the segment's longitudinal axis, even when this axis is not explicitly defined. Additionally, the equations provided by de Leva (1996) consistently assumed that the COM lies along this longitudinal axis, which might be an oversimplification. When employing these values for defining three dimensional BSIPs, certain assumptions are necessary, as noted by Dumas and Wojtusch (2018). The adjustments to BSIPs of McConville et al. (1980) and Young et al. (1983) by Dumas et al. (2007), and later by Dumas and Wojtusch (2018), present BSIPs directly within

clearly defined segment coordinate systems. These adjustments also formulate scaling equations that do not limit the position of the center of mass or the orientation of the principal inertia axes.

Other methods. Various other methods that are not described in detail in this work have been employed to estimate human BSIPs, each characterized by distinct approaches and levels of accuracy. The water immersion technique and the quick release method, as detailed in Drills et al. (1964), represent early foundational methods in this area. More recent advancements, such as dynamic analysis, have been investigated, for instance, in the studies by Chen et al. (2011), Doane and Quesada (2009) and Hansen et al. (2014). Dynamic analysis, where force plate data and kinematics are recorded simultaneously, has shown potential in optimization of subject specific BSIPs. However, the results are not always easily adapted to elsewhere as dynamic analysis does not directly measure masses of body segments (Merrill et al. 2019).

2.2 Errors in mathematical BSIP models

As medical imaging techniques have become more widely used and their accuracy more evident, several researchers have utilized these approaches to analyse the errors in popular predictive regression and geometric models cited in academic literature. This chapter reviews some of studies where these errors have been examined.

Rossi et al. (2013) evaluated the accuracy of five mathematical BSIP models by comparing them across three groups: 10 male swimmers, 8 female swimmers, and 10 healthy young Caucasian non-swimmers. The errors were assessed based on the deviation from individual BSIPs derived from DEXA scans. The BSIP models evaluated included those developed by Chandler et al. (1975), Yeadon (1990), Zatsiorsky and Seluyanov (1983), Zatsiorsky and Seluanov (1985), and Zatsiorsky et al. (1990a). Errors were evaluated for head, trunk, upper arm, forearm, thigh, and shank segments. Each of the five BSIP models showed errors exceeding 10 % for at least one parameter (segment mass, segment COM position or segment inertia) across all participant groups. The Percentage Root Mean Square Errors (%RMSE) for segment longitudinal COM positions, as reported by Rossi et al. (2013), are depicted in figure 3.

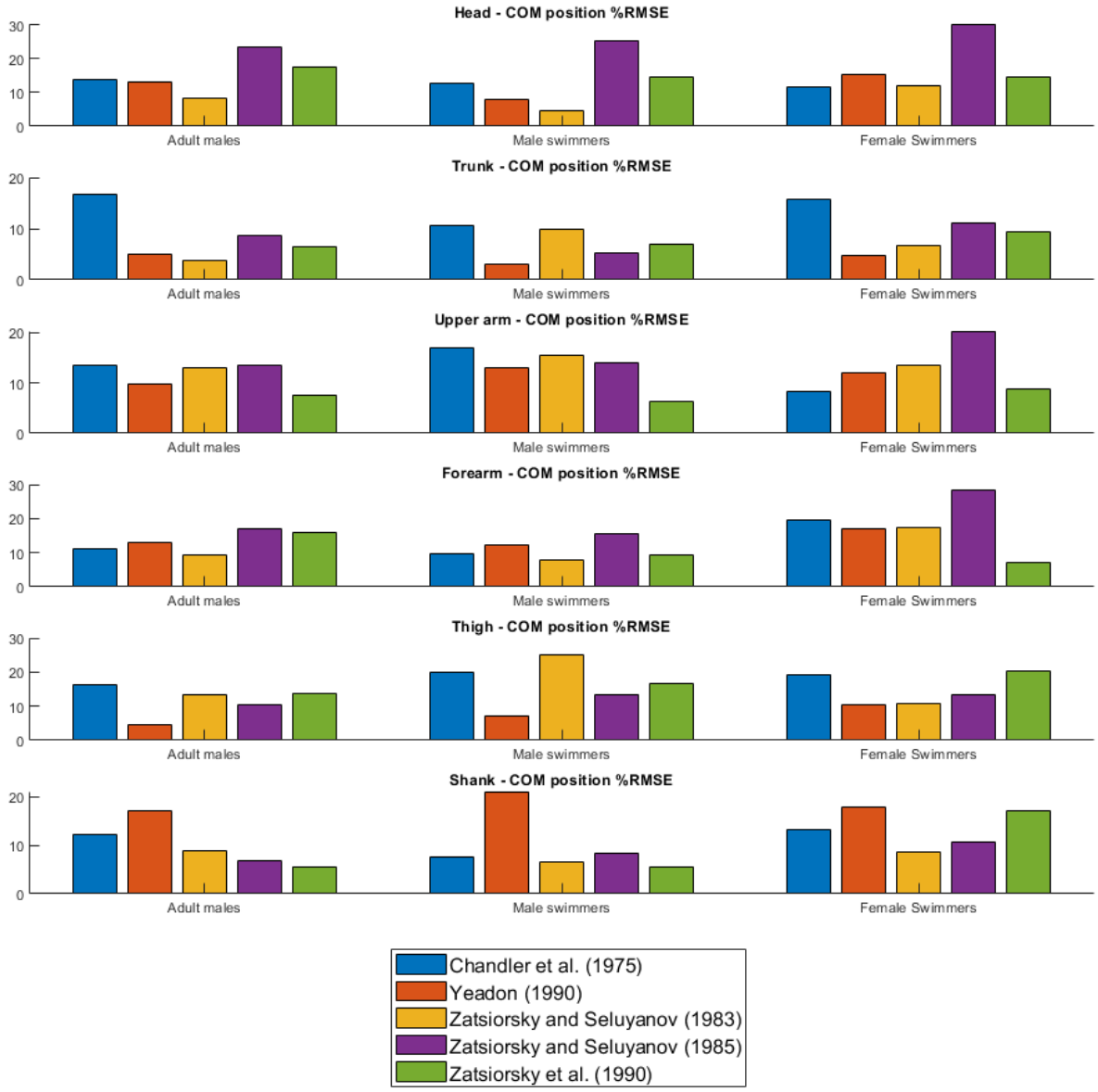

FIGURE 3. Percentage Root Mean Square Errors (%RMSE) in BSIP models for segment COM position for non-swimmers (adult males), male swimmers and female swimmers as reported by Rossi et al. (2013). Figure created from Rossi et al. (2013) data.

Durkin and Dowling (2003) analysed the effectiveness of four well-known mathematical models in estimating BSIPs in four different human groups. This study involved comparing linear regression equations of Dempster (1955) multiple regression equations of Zatsiorsky et al. (1990b), geometric models of Zatsiorsky et al. (1990a) and of Hanavan (1964). Data was collected for each participant using DEXA, from which a new set of regression equations was created and evaluated against these four well-known mathematical models. The results from

the DEXA scans revealed significant differences in BSIPs among the populations studied, emphasizing the need for BSIP predictors tailored to specific populations. All BSIP models evaluated in Durkin and Dowling (2003) showed significant inaccuracies, primarily due to these significant individual differences within the groups. The study also discovered ineffectiveness of geometric BSIP models, potentially because of assuming uniform density or using overly simplistic shapes. Durkin & Dowling (2006) subsequent study also showed large errors in Dempster (1955), Hanavan (1964), Zatsiorsky et al. (1990a) multiple regression equations, and Zatsiorsky et al. (1990b) geometric model estimations for lower leg BSIPs.

Cheng et al. (2000) compared five sources of estimates for BSIPs, including Dempster (1955) and Clauser et al. (1969), to MRI-derived data of eight Chinese males. Errors for trunk segment COM estimates were found to range from 12.2 % to 20.2 %. The errors for the foot segment ranged from 11.1 % to 9.1 %, for the shank from 0.9 % to 7.1 %, and for the thigh, from 1.4 % to 7.5 %. The authors highlighted that these notable differences in trunk estimates might be caused by different boundary definitions between data sources.

Virmavirta and Isolehto (2014) evaluated the accuracy of Dempster (1955) and de Leva (1996) models in estimating the COM position longitudinally in various physically active groups. Using a high-precision reaction board as a benchmark, they found that in general, for male participants in the study, the de Leva model underestimated, and Dempster model overestimated the COM in the longitudinal direction. Specifically, the measured COM position for male participants with the reaction board was 57.03±0.79 %, while de Leva and Dempster models predicted 56.20±0.76 % and 57.60±0.76 %. Further subgroup analysis of male athletes involved in the study revealed that for gymnasts and throwers, Dempster's prediction closely matched the reaction board measurement, while for high jumpers, the de Leva model provided more accurate results. These findings again underscore the influence of population-specific factors on the accuracy of BSIP models.

2.3 Effects of BSIP errors in biomechanical studies

Errors in BSIP models, as demonstrated by Durkin and Dowling (2003), Durkin and Dowling (2006), Virmavirta and Isolehto (2014), Rossi et al. (2013), and many others, all point to the conclusion that accuracy of well-known and widely used mathematical BSIP models, such as

those by Dempster (1955) and Zatsiorsky et al. (1990a), are subject depended. Errors in in these BSIP estimates can significantly impact the results of the biomechanical measurements (Andrews & Mish 1996; Camomilla et al. 2017; Fritz et al. 2019; Köhler et al. 2024; Kwon 1996; Pearsall & Costigan 1999; Rao et al. 2006). It's been shown, however, that even slight optimizations and individualisations in BSIPs can lead to enhanced accuracy in obtained results (Fritz et al. 2019; Köhler et al. 2024; Rao et al. 2006).

The acceptable margin of error in BSIP estimations depends on the specific calculation methods in which these parameters are used, as values from various BSIP models used show a wide range of variability based on the chosen calculation approach (Durkin 2008). Researchers have emphasized the importance of reporting the BSIP estimation method used in studies (Köhler et al. 2024; Kwon 1996) for assessing the comparability of results across different studies.

3 WHOLE BODY ANGULAR MOMENTUM

WBAM is a measure of rotational momentum of the entire body. It is a scalar quantity in planar analyses, and vector quantity in 3D analyses, that represents the amount and direction of rotational momentum of the body about a specified point, typically the body's COM (Robertson et al. 2014 89 - 90), and it plays a significant role in understanding the human movement. WBAM control is crucial for maintaining balance, ensuring efficient locomotion, adapting to disturbances during various activities, and for executing precise and controlled rotational movements (Herr & Popovic 2008; Pijnappels et al. 2005; Yeadon 1993).

Two different calculation approaches exist to determine WBAM – the kinematic and the impulse method. This chapter reviews the differences between these two calculation methods and provides information about potential error sources related to each of the methods. Also, the relationship between angular momentum and moment of inertia is discussed.

3.1 Kinematic method to determine angular momentum

Kinematic data together with inertial properties of the body segments can be used to determine the angular momentum (L) of a segment. Kinematic based angular momentum of a segment rotating about its COM can be defined as follows:

$$L = I\omega \tag{1}$$

where I is the moment of inertia (in kgm^2) of the segment about its center of gravity, and ω is the angular velocity of the segment. For planar analyses, moment of inertia is a single scalar quantity, but for 3D analyses moment of inertia tensor $\bar{I}$ must be used. Moment of inertia tensor is a 3x3 matrix:

$$\bar{I} = \begin{bmatrix} I_x & P_{xy} & P_{xz} \\ & I_y & P_{YZ} \\ sym. & & I_z \end{bmatrix}$$

where the diagonal elements are referred to as the principal mass moments of inertia and off-diagonal elements are the mass products of inertia. Similarly, for planar analyses angular velocity ω is a scalar quantity, but in three dimensions it is a 1x3 vector describing the rotation of the system in 3D space. (Robertson et al. 2014, 70 - 78, 89 - 90)

The angular momentum of whole body can be determined by summing the angular momentum values for each segment (Zatsiorsky, 1998). To calculate WBAM about the whole body COM, the axis of rotation of each segment must also be considered as the segments are not solely rotating around their COM, but also around the whole body COM. To calculate the angular momentum of a segment about whole body COM, the determination of the associated moment of momentum (L_{mofm}) of each segment is necessary. L_{mofm} of a segment is based on the parallel axis theorem, and it is defined for planar analyses as:

$$L_{mofm} = [\vec{r_s} \times m_s\vec{v_s}] = m_s(r_x v_y - r_y v_x) \tag{2}$$

where r_x and r_y represent X and Y components of the position vector that extends from the axis of rotation (total body COM) to the segment's COM, m_s is the segment's mass, and v_x and v_y are the X and Y components of the linear velocity of the segment. For three dimensional analyses, the Z components of $\vec{r_s}$ and $\vec{v_s}$ must also be considered. The sum of all the segment angular momenta plus their associated moments of momentums is the total WBAM (L_{total}), and it can be calculated with the following equation:

$$L_{total} = \sum_{s=1}^{S} I_s\omega_s + [\vec{r_s} \times m_s\vec{v_s}] \tag{3}$$

where S denotes the number of segments, I_s is the centroidal moment of inertia of segment S, and ω_s is the angular velocity of segment S. In literature, the moment of momentum associated with the movement of body segment relative to a fixed point (such as the COM of the whole body) is often referred to as the **remote term**. Conversely, the **local term** refers to the angular momentum generated by the segment's rotation about its own COM. (Robertson et al. 2014, 89 - 90)

3.2 Impulse method to determine angular momentum

An alternative method for determining the WBAM (or more precisely, the change in WBAM, ΔL) is the angular impulse method, which involves determining the force applied over a time period that causes the body to rotate. Angular impulse is integral of the moment of force, also known as torque τ, about the whole body COM over the time interval during which the force acts. To determine the angular impulse, the external forces acting on the body and the body's COM trajectory must be recorded simultaneously. (Robertson et al. 2014, 89 - 90) The formula to calculate the angular impulse is:

$$\Delta L = \int (\vec{r} \times \vec{F} + \tau_v) dt \tag{4}$$

where $\vec{F}$ is the applied force, $\vec{r}$ is the position vector from body COM to the force's point of application and τ_v is the torque at the force's point of application due to friction (Negishi & Ogihara 2023a). The cross product of $\vec{r}$ and $\vec{F}$ in this equation equals to the torque caused by the external forces. It should be noted that τ_v can only have vertical component if the force's point of application is the ground, thus having effect only about the transverse plane (Negishi & Ogihara 2023a). The L_{total} can be then expressed as:

$$L_{total} = \Delta L + L_{initial} \tag{5}$$

where $L_{initial}$ is the initial angular momentum before the angular impulse. Thus, if the $L_{initial}$ is zero, the angular impulse will be equal to L_{total}. (Robertson et al. 2014, 89 - 90)

3.3 Moment of inertia

The law of conservation of angular momentum states that the amount of angular momentum stays constant if the applied moments are zero. Thus, if no external forces are present, or if the acting external force passes through the total body COM (as gravitational force does), WBAM will remain constant. Therefore, when the human body is airborne, the WBAM remains un-changed (excluding the possible effects of aerodynamic forces). This does not, however, mean

that the angular velocity of the body will remain constant. (Robertson et al. 2014, 89) Adjustments in body configuration can alter the total body moment of inertia, which can lead to changes in angular velocity about different axes. This can be seen in sports such as gymnastics and diving, where athletes gracefully control the rotation of their bodies by adjusting their body configuration whilst airborne. (Yeadon 1993) To give the reader a better understanding of this phenomenon, a brief explanation of moment of inertia is provided in this chapter.

The mass moment of inertia, often simply referred to as the moment of inertia, represents a system's resistance to change in its rotational movement. Traditionally, it's described as the second moment of mass, calculated as the integral of the product of mass particles and the square of their distances from a specific axis, expressed mathematically as:

$$I_{axis} = \int r^2 dm \tag{6}$$

where I_{axis} is the moment of inertia for single axis, and r denotes the distance of each mass particle, denoted as dm, from an axis of rotation. To calculate the moment of inertia for body segments, a derived measure known as the radius of gyration can be utilized in the biomechanical analysis of BSIPs. The radius of gyration is a measure that indicates the hypothetical distance at which the entire mass of a rigid body would need to be concentrated, assuming it were to be located at a single point, to have the same rotational inertia. Essentially, a body segment can be considered as a point mass located at this specific distance, known as the radius of gyration (k), from the axis of rotation. Unlike the COM position, which is independent of the axis of rotation, the radius of gyration varies depending on the axis around which the body segment is rotating. The value of radii of gyration can be made proportional to a segment's length, which simplifies the determination of segmental moments of inertia for any axis. The centroidal moment of inertia, representing the radius of gyration for a segment rotating about its COM can by calculated by using the formula:

$$k_{cg} = K_{kg} L \tag{7}$$

where k_{cg} is the radius of gyration in meters, K_{cg} is the proportion of the segment's length that corresponds to the radius of gyration, and L is the length of the segment in meters. (Robertson et al. 2014, 70 - 78)

From k_{cg} the segment's centroidal moment of inertia can be calculated from:

$$I_{cg} = mk_{cg}^2 \tag{8}$$

where I_{cg} is the segment's moment of inertia rotating about its own COM and m is the mass of the segment in kilograms. The calculation of the segment's moment of inertia about any other axis, the whole body COM for example, can be done by using the formula:

$$I_{axis} = I_{cg} + mr^2 \tag{9}$$

where I_{axis} is the moment of inertia about chosen axis, and r is the distance from the axis to the segments' COM. From here, the total body centroidal moment of inertia can be calculated by summing the centroidal moments of inertia and the transfer terms of each segment:

$$I_{total} = \sum_{s=1}^{S} I_{cg} + \sum_{s=1}^{S} m_s r_s^2 \tag{10}$$

where S denotes the number of segments and r_s is the distance from total body COM to each segments' COM. (Robertson et al. 2014, 70 - 78)

Understanding the relationship with WBAM and total body moment of inertia clarifies how changes in body configuration can affect the angular velocity while maintaining constant angular momentum. Since the formula to calculate the total body centroidal moment of inertia includes the distance between the whole body COM to the COM of each segment, it follows that moving any segment's COM closer to the whole body COM will reduce the moment of inertia, and vice versa. Given that the angular momentum of a system is the product of its moment of inertia and angular velocity, as described in chapter 3, any alterations in the system's moment of inertia must inversely impact the system's angular velocity if the system's angular momentum is constant. Even seemingly minor adjustments in body posture, such as maintaining the head down in a tucked position while executing somersaults, can have a considerable impact on the moment of inertia, and therefore to the angular velocity of the body, as demonstrated in figure 4 (Schueler et al. 2018).

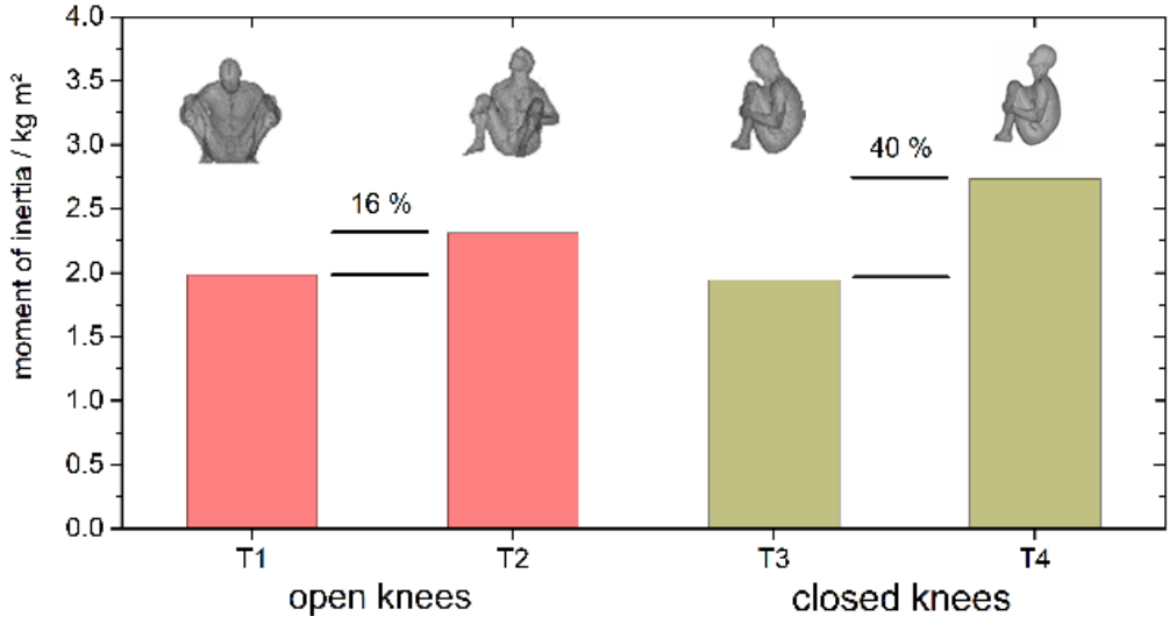

FIGURE 4. Calculated moments of inertia in a tucked position from a single subject, utilizing a 3D surface scanning. T1 denotes the moment of inertia with knees open and head down, T2 with knees open and head up, T3 with knees closed and head down, and T4 with knees closed and head up (modified from Schueler et al. 2018).

3.4 Error sources in WBAM calculations

As discussed in previous chapters, there are two primary ways to determine WBAM: the kinematic method and the impulse method. When these methods are used, it is important to understand the potential sources of error associated with them. This chapter discusses the potential sources of error between these two calculation methods.

Error sources in kinematic method. To calculate WBAM using the kinematic method, kinematic data must first be collected, typically by using video or motion capture systems. This data is used for the tracking of the positions of the body segments, thereby allowing the determination of segmental orientations together with their angular and linear velocities (Dapena 1978; Herr & Popovic 2008; R. Sanders & Wilson 1988). In addition to this, each segment's inertial parameters, including mass, moment of inertial and position of COM relative to the segment's endpoints must be known or estimated. These parameters are usually obtained from regression equations or can be measured individually for the subjects, as detailed in chapter 2.

Combining kinematic data with BSIPs enables the calculation of WBAM with the kinematic method using the equations presented in chapters 3.1 and 3.2. The potential for significant errors arising from BSIP estimation has already been established in chapter 2. Furthermore, additional errors may accumulate due to various factors, including inaccuracies in the motion capture system used (Nagymáté & Kiss 2018; van der Kruk & Reijne 2018), the impact of soft tissue artefact (Cappozzo et al. 1996), errors in marker placement (Osis et al. 2016), and misalignment of segment endpoints in accordance with the BSIP model used (Dumas & Wojtusch 2018). As the kinematic method requires linear and angular velocities of the segments, segment position data obtained with the 3D motion capture system must be differentiated. This differentiation amplifies any existing errors in the positional data, which can significantly affect obtained WBAM values. However, proper filtering of the kinematic data can help minimize these errors. (Winter 2009, 35 - 38)

Error sources in impulse method. To determine WBAM with the impulse method, the external forces and their point of application acting on the body must be measured. Additionally, the total body COM must be determined. Typically, the total body COM is determined using similar approaches to those in kinematic method: a motion capture system is used to obtain the positions of body segments, and based on these the weighted average of the segment COM position is used to determine the total body COM (Mathiyakom et al. 2023). While segmental masses and their COM positions relative to their endpoints are necessary for these calculations, the moment of inertia is not required. This eliminates one potential source of error arising from the BSIPs that is present in the kinematic method.

Similar errors in obtaining the motion capture data apply between the kinematic and the impulse methods, but with the impulse method the differentiation of linear or angular velocities of the segments are not necessary, which in theory, can reduce errors associated with these calculations.

External forces acting on the body and their point of application are typically obtained by using force plates. The average point representing the location where the force is being applied is referred to as the center of pressure (COP), and the external forces acting on the body are referred to as ground reaction forces (GRFs). When using force plates, errors can be introduced in the magnitude and direction of the GRFs, as well as to the COP (Chockalingam et al. 2002; Schmiedmayer & Kastner 1999).

4 ANGULAR MOMENTUM IN SPORTS AND HUMAN MOVEMENT

The WBAM is regulated by musculoskeletal system. This regulation involves adjusting the body COM in relation to the point of contact with the ground and fine-tuning the direction of the GRFs. These adjustments are essential for fulfilling requirements related to WBAM for any given tasks, be it a complex acrobatic manoeuvre, or a simpler task such as regulation of WBAM during walking to avoid falling. (Mathiyakom et al. 2023; Pijnappels et al. 2005)

This chapters reviews some of the studies where the management and generation of WBAM has been explored during different tasks. The focus of this chapter is on sports involving airborne movements, where the control and generation of WBAM is not only essential but also widely studied.

4.1 Angular momentum in sports involving airborne movements

The phenomenon of angular momentum has been extensively studied across a range of sports-related activities, especially in sports involving airborne movements such as diving, gymnastics, ski jumping and triple jump. Study of You and Hay (1995) is considered as a breakthrough in complex dynamic movement quantification, as it was the first paper to report WBAM in all three dimensions during a highly complicated motion. In this study, three-dimensional WBAM was examined in triple jump during 1992 U.S. Olympic. Significant nonlinear correlation was identified between the mediolateral WBAM during the support phase of a step and the resulting jump distance ($r=0.86$). The results also suggested that the necessary WBAM in the mediolateral direction should be generated during the support phase of the hop preceding the take-off, and that the change in WBAM during the support phase of the step should be kept minimal.

WBAM during acrobatic airborne tasks. Despite extensive research, defining optimal levels of WBAM for tasks involving acrobatic airborne rotations can be challenging, or even impossible, as achieving the objectives related to these tasks often requires balancing several key factors. For instance, generating WBAM for complex movements, such as a somersaulting dive or a high bar dismount at the end of a gymnastics routine, comes at the expense of COM vertical velocity. Due to reduced vertical velocity at take-off, this trade-off results in shorter airtime and limits the athlete's ability to complete the necessary rotations and prepare for a safe landing.

Therefore, both linear and angular momentum must be generated sufficiently to successfully perform the skill. The sufficient levels of angular and linear momentum do not only depend on the nature of the skill, but also on the individual inertial characteristics such as body weight, limb length, and body mass distribution. Additionally, different techniques can be used to control the moment of inertia by altering the body configuration, which together with WBAM affects the rotation of the body during the performance of the task. Therefore, there are infinite number of different linear and angular momentum combinations that can be used for a successful performance of a task. (Hiley & Yeadon 2005; McNitt-Gray 2018)

Springboard diving exemplifies a sport where precise control of angular and linear momentum is essential. Divers must generate significant angular and linear momentum at take-off and adjust their angular velocity mid-air by controlling their inertia. Hamill et al. (1986) together with Miller and Munro (1985) have demonstrated that the rotational demands of a dive are directly correlated with an increase in WBAM at take-off. While the contributions of body segments to the total WBAM vary across different types of dives, the segments most distal to the whole body COM provided the greatest contribution to the WBAM at take-off (Hamill et al. 1986). Dives without twists generally require less WBAM around the somersault axis at take-off, as dives that include twists must redistribute some of the angular momentum to different axes (R. Sanders & Wilson 1988), a technique that has been thoroughly explained by Yeadon (1993). Segmental local terms contribute minimally to the overall WBAM in springboard diving, accounting for only about 10 % to 20 %, while the majority of WBAM is derived from remote terms (Hamill et al. 1986; Miller & Munro 1985).

The techniques used for generating WBAM in diving vary with each type of dive due to their unique linear and angular momentum demands. For instance, in backward and reverse backward somersault dives, while WBAM is consistently generated in the backward direction, the horizontal velocity must be generated in opposite directions. The generation of linear and angular momentum is dependent on the GRFs magnitude and direction, and COM position relative to the GRFs point of application. Since the GRFs must be directed differently for both types of dives to account for the linear momentum needs of the dive, the control of COM position relative to resultant GRFs must then be adjusted accordingly to account for the angular momentum demands on the dive. (Mathiyakom et al. 2023) Example on the differences between resultant GRF's direction and COM's position relative to the GRFs point of application between these two types of dives are demonstrated in figure 5. Both the kinematic and the impulse

method have been employed to examine WBAM generated during take-off in diving (Mathiyakom et al. 2007; Mathiyakom et al. 2021; Mathiyakom et al. 2023; Miller et al. 1989; R. Sanders & Wilson 1988)

FIGURE 5. Differences in direction of resultant GRF and COM position during backward somersaulting dive and reverse backward somersaulting dive in generation of the required linear and angular momentum (modified from Mathiyakom et al. 2007).

WBAM has also been thoroughly examined during different gymnastics related skills (Gervais & Dunn 2003; Hiley et al. 2015; Hiley & Yeadon 2003; Hraski & Mejovsek 2004; Irwin et al. 2011; Kerwin et al. 1998; King & Yeadon 2004; Takei et al. 2003), highlighting its importance during acrobatic tasks. As an example, Hwang et al (1990) conducted an analysis on somersault axis WBAM about COM during different types of double backward somersaults performed at the 1988 Summer Olympics. In the study, kinematics based WBAM was calculated from three different non-twisting double back somersaults (tucked, piked, and layout position), which were performed from roundoff and backward handspring. WBAM mean values at take-off ranged from 122.02 kgm^2s^{-1} during layout double somersaults to 72.5 kgm^2s^{-1} during tucked double somersault. Local terms were shown to account between 26 % to 30 % of total WBAM for each type of double somersault.

The techniques used to generate WBAM during acrobatic tumbling skills are naturally completely different than of those performed without any initial linear or angular momentum, such as the backwards rotating dives mentioned earlier. In backwards rotating tumbling skills, the linear and angular momentum is generated prior to the somersaulting skill during the roundoff and back handspring. In the contact phase before the take-off, the horizontal velocity and WBAM tends to decrease, while vertical velocity increases. Decrease in WBAM is due to the

COM being anterior relative to the GRFs point of application during the final contact phase, as illustrated in figure 6, which leads to the vertical components of the GRFs to generate forward WBAM. Although the horizontal components of the GRFs increase the WBAM, the decrease in WBAM due to the vertical components is typically greater, which leads to net loss in WBAM. Thus, the objective of the athletes during the take-off phase is to minimize the loss of WBAM and to generate sufficient vertical linear velocity necessary to complete the task. (Yeadon 2017)

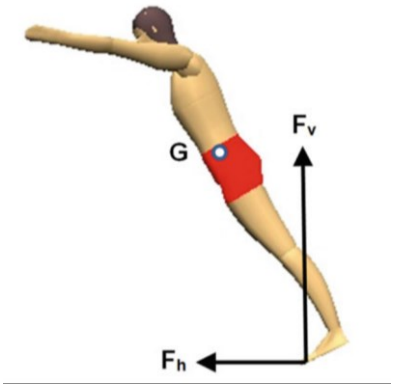

FIGURE 6. During the take-off in a backward somersault in tumbling, the COM (G) being anterior to the point of application of the GRFs causes the vertical components of the GRFs (F_v) decrease and horizontal components (F_h) increase the WBAM in the backwards direction (Yeadon 2017).

In tumbling skills, rapid arching during take-off has been shown to be a key factor in generating higher WBAM value in layout position double somersaults, in contrast to those performed in tucked and piked positions (Kerwin et al. 1998), as this technique minimizes the loss of WBAM at take-off (Yeadon 2017). Higher WBAM values necessary for the layout double somersault can be attributed to an increased moment of inertia in layout position compared to tucked position. The effect of significant decrease in WBAM between touch down and take-off in tumbling has been observed in numerous studies (e.g. Hraski & Mejovsek 2004; Hwang et al. 1990). WBAM values during standing tuck back somersaults have been analysed in a few studies, ranging from 57.9 kgm^2s^{-1} to 63.4 kgm^2s^{-1} (Król et al. 2016), and 53.1±8.2 kgm^2s^{-1} (Król et al. 2020). Naturally, these values are much smaller than the values obtained by Hwang et al. (1990), as the somersaults studied by Hwang et al. (1990) were performed following a roundoff and back handspring, during which considerable amounts of WBAM can be generated prior to the somersault take-off.

Ski jumping. The demand for WBAM generation in ski jumping can be considered unique compared to most sports due to significant aerodynamic forces present. The control of WBAM during take-off and flight is one of the most important factors in ski jumping performance (Virmavirta 2017). In ski jumping, the goal of the athlete to quickly achieve a stable flight position with optimal lift-to-drag ratio. To reach the optimal flight position, forward rotating WBAM must be generated at the take-off. This forward rotating WBAM produced at take-off is necessary to compensate the backward rotating WBAM produced by aerodynamic forces acting on the jumper's body during the take-off and at the early flight phase. Only if the forward rotating WBAM generated at take-off sufficiently compensates for the backward rotating WBAM, can the athlete reach an optimal and stable flight position (figure 7). (Schwameder 2008) Too low forward rotating WBAM at take-off can lead to disadvantageous flight position, while too much WBAM at take-off can increase the risk of falling. (Müller 2006)

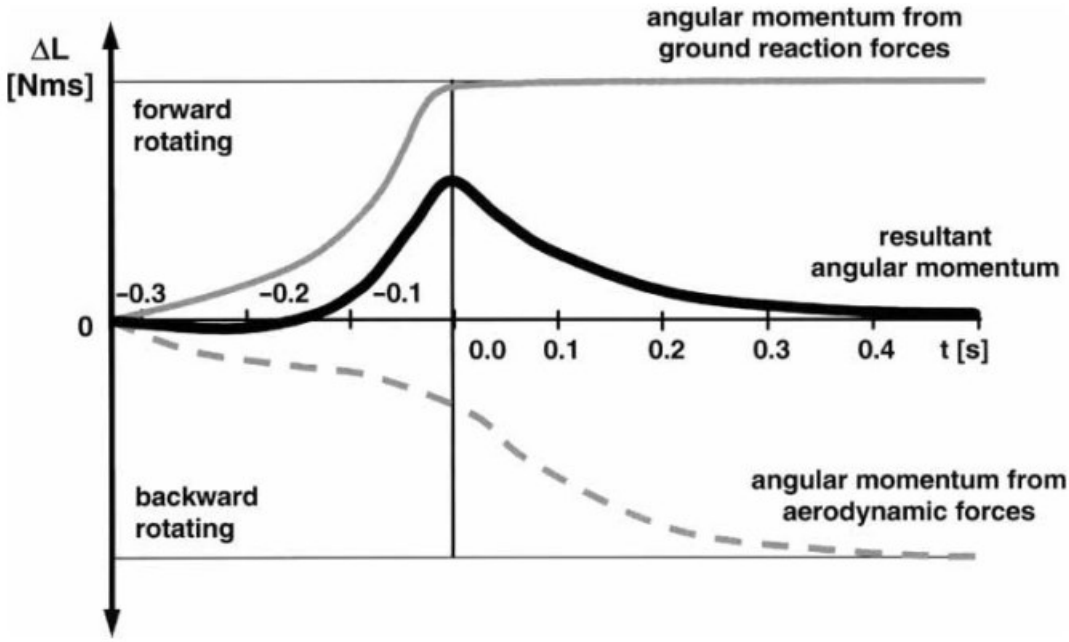

FIGURE 7. Change in angular momentum in ski jumping during take-off and early flight phase. Negative time represents take-off phase and positive time the flight phase. When the forward rotating angular momentum produced at take-off and backward rotating angular momentum produced by aerodynamic forces are in balance, the ski jumpers can reach a stable flight position (Schwameder 2008).

4.2 Angular momentum control during walking

In addition to acrobatic airborne tasks, the regulation of WBAM has been a key focus in investigation of human walking as it is correlated with stability and fall risk. Herr and Popovic (2008) used principal component analysis to examine how WBAM is managed during walking using kinematic data obtained by a custom 16 segment human body model. Their findings suggested that due to segment-to-segment cancellation – where angular momentum generated by one body segment is cancelled out by the momentum of one or multiple other segments – WBAM is maintained within a narrow range across the sagittal, frontal, and horizontal planes. On the contrary, Bennett et al. (2010) study found that although significant segment-to-segment cancellation occurs in the sagittal plane, for the frontal and horizontal planes the effect of segment-to-segment cancellation is not nearly as significant as previously thought. Negishi and Ogihara (2023b) concluded that as WBAM during walking is not zero, the GRFs present must also counteract WBAM, as only external forces can alter WBAM during movements. The authors examined regulation of WBAM during walking using kinematic data from a 13-segment human body model, where BSIPs presented in de Leva (1996) and Zatsiorsky (2002) were used. Their findings indicated that in the sagittal and horizontal planes segment-to-segment cancellation is the main contributing factor in minimizing WBAM, but in the frontal plane the contribution of segment-to-segment cancellation was found to be minimal. The study also reported variations in the calculated torques about the whole body COM when comparing results obtained from using only kinematic data against those calculated based on GRFs. From the kinematic data, the moment of force was obtained by calculating the rate of change in WBAM, which in theory should be equal to the torque caused by GRFs. Particularly in the sagittal plane during the double support phase, differences were obtained in torque values between these two methods, pointing to potential inaccuracies in the BSIPs estimations used in the study.

The influence of aging on WBAM control during walking was investigated by Begue et al. (2021), where full body kinematics of 18 older (68.4±4.30 yr.) and 15 young (25.0±3.20 yr.) adults were recorded during two different walking speed conditions. Older adults were shown to have larger angular moment for the trunk and leg segments in the sagittal plane, contributing to a higher range of total angular momentum in sagittal plane during both walking speeds. Older individuals at a higher risk of falling have been shown to be less able to counteract WBAM generated by tripping over an obstacle (Pijnappels et al. 2005), and fallers show generally lower

muscle strength (Pijnappels et al. 2008). It has been suggested that muscle weakness could be the underlying reason why fallers have difficulty in WBAM control (Silverman et al. 2012). In general, the probability of falling during walking has been shown to be greater on a decline surface compared to level or incline surface (Redfern et al. 2001). As a protection mechanism the WBAM is more controlled (the range of WBAM is more reduced) while walking on a decline surface compared to walking on level or incline surface (Silverman et al. 2012). Higher body mass index has been linked with greater WBAM range in transverse and frontal planes during walking, mainly due to wider step width (Kim et al. 2022). As larger frontal plane WBAM range has been shown to be related to greater fall risk (Browning 2012), it has been proposed that the increased step width could also be one of the reasons for challenges in adapting to external perturbations during walking, leading to increased fall risk (Kim et al. 2022).

4.3 Impact of BSIP model choice on WBAM values

Only a limited number of studies have explored the impact of the chosen BSIP model on the resulting WBAM values. Kwon (1996) investigated the impact of 10 different BSIPs estimation models on the calculation of WBAM during aerial phase of three collegiate gymnasts performing full twisting double back somersault high bar dismounts. In this study four cadaver based models (based on the work of Chander et al. (1975) and labeled as group C in figure 8), four gamma mass models (based on the work of Zatsiorsky and Seluanov (1983), Zatsiorsky and Seluanov (1985) and Zatsiorsky et al. (1990a) and labelled as group M in figure 8), and two geometric models (labelled as group G in figure 8), based on modified Hanavan (1964) and modified Yeadon (1990) model were compared. Figure 8 illustrates the variance among the 10 estimation models in terms of their impact on the average somersault axis WBAM values, revealing discrepancies exceeding 10 % among the models.

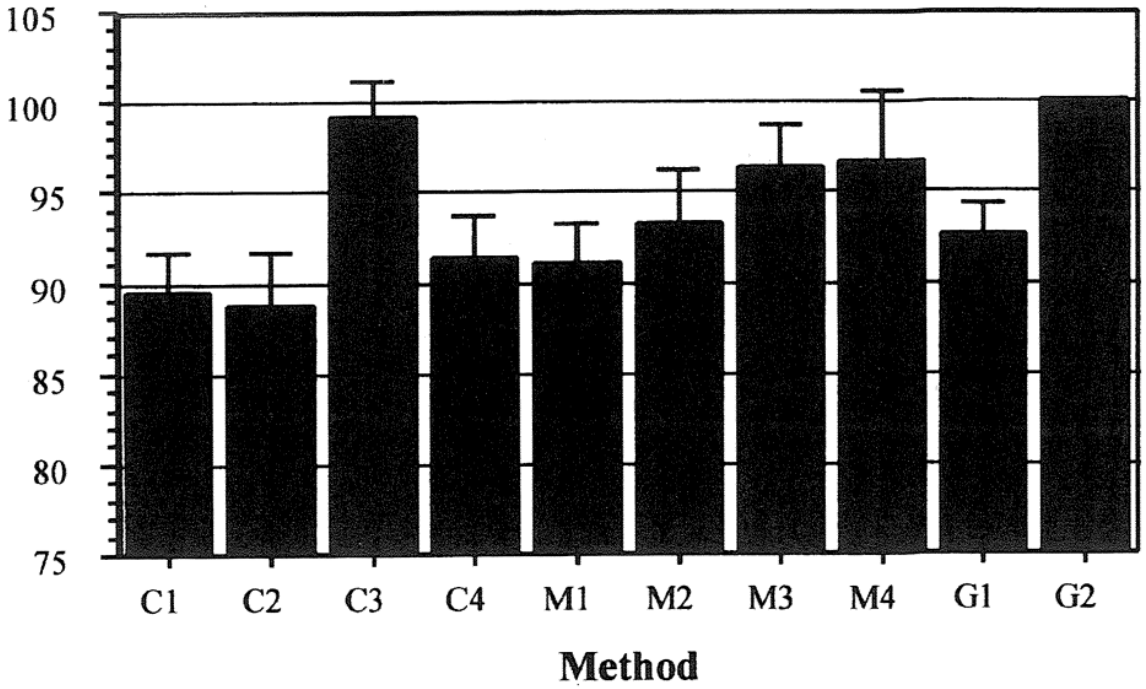

FIGURE 8. Mean somersault axis WBAM ratios for BSIP models, normalized to values obtained from using Yeadon (1990) geometric model (method G2) during high bar dismount. C1 – C4 ratios obtained from cadaver-based, M1 – M4 from gamma mass based, and G1-G2 from geometric based BSIP models. (Kwon, 1996)

Similarly, Schüler et al. (2016) compared two BSIPs estimation models on WBAM calculation from kinematic data recorded from three springboard divers performing 1½ tucked back somersaults. Hanavan (1964) BSIP model was compared to individualised BSIP model generated from 3D-laser scan between three subjects, where uniform density across the segments was assumed. Moderate to good Spearman's rank correlation coefficients were observed between the two models (between 0.538 to 0.742) for the remote term WBAM. Among the participants, the greatest average difference in the models for WBAM at take-off was 4.8 kgm^2s^{-1}, as values were 28.4±3.1 kgm^2s^{-1} for individualised model and 33.2±3.0 kgm^2s^{-1} for Hanavan model. Smallest difference was observed as 0.8 kgm^2s^{-1}, as WBAM values were 17.0±1.5 kgm^2s^{-1} for the individualised model and 16.2±1.5 kgm^2s^{-1} for the Hanavan model.

5 PURPOSE OF THE STUDY

WBAM is fundamental metric in the field of biomechanics, and it is essential for understanding and analysing human movement, particularly in activities involving rotation and balance. This study investigates the WBAM calculation through two computational methods – kinematic and impulse – using three regression equation-based BSIP models.

To date, the potential discrepancies between these two calculation approaches have not been examined. As there is no 'ground truth' for WBAM values, this study does not attempt to establish which method is more accurate but rather compare the results from both methods to understand their differences. This comparison is done by using different BSIP models during different types of jumping trials, each trial with their own requirements for WBAM. The research questions of this study are:

1) How do kinematic and impulse based calculation methods compare in determining WBAM when using the same BSIP model?

The hypothesis is that significant differences can be observed between the calculation methods, and that the magnitude of these differences are likely influenced also by the choice of the BSIP model. Ideally, with perfect motion capture and force plate data, and a perfectly matched BSIP model, the results from both methods should be identical. However, due to inherent sources of error in various BSIP models and the limitations of motion capture data, such consistency cannot be expected.

2) How do the results of kinematic and impulse calculation methods vary across different BSIP models when applied independently? Additionally, given the absence of 'ground truth' WBAM values, does either one of the calculation methods demonstrate greater consistency in WBAM values across the trials by yielding results that are closely aligned across different BSIP models?

The hypothesis is that significant differences will be observed in WBAM values when using different BSIP models with the same calculation method, as noted in previous studies based on the kinematic method (Kwon 1996; Schüler et al. 2015). Similar results are expected for the impulse method calculations, but the magnitudes of these differences are yet to be determined.

The impulse method is expected to provide more consistent results between the BSIP models considering the possible sources of error (as described in chapter 3.4.) between these two calculation methods. Although different BSIP models are expected to introduce variability in the results, it is assumed that the impulse method will still yield more consistent WBAM values.

In this study, the calculation of sagittal plane WBAM is based on the assumption that movements during the trials occurs strictly parallel to this plane and that the principal axis of rotation for the body segments is the medio-lateral axis. Given these assumptions, an additional research question was formulated:

3) Does the assumption that the movements during the jumps performed in the study occurred solely parallel to the sagittal plane, and that the medio-lateral axis was the principal axis of rotation for the segments, affect the obtained WBAM values?

Hypothesis is that the assumption regarding plane-specific movement and axis of rotation will not significantly influence the calculated WBAM values, due to the nature of the trials performed in the study.

6 METHODS

To answer the research questions, both the kinematic and the impulse methods were employed, together with three commonly used BSIP models, to calculate sagittal plane WBAM generated prior to take-off during three distinct types of jumping trials.

Given the nature of trials performed in this study, it was assumed that all movements occurred parallel to the sagittal plane and that the principal axes of rotation were the medio-lateral axes for each body segment. This assumption simplified the analyses and allowed for the calculation of WBAM for BSIP models where datasets were incomplete for some of the inertial properties of the segments.

To test the effect of the single plane assumption, WBAM was also calculated for one BSIP model without applying this assumption. This model, which had complete 3D inertial properties available, served as a basis for comparing the WBAM values obtained under different analytical conditions.

6.1 Participants

Two male gymnasts without musculoskeletal injuries were recruited for the study (table 1), both with over 15 years of experience in artistic gymnastics. Participation in the study was entirely voluntary. The participants were informed about the testing protocol, the risks involved, and their rights, both in written and oral forms. They were also made aware that they could withdraw from the study at any time without needing to provide a reason.

TABLE 1. Subject description

Subject	Height (cm)	Mass (kg)	Age (years)
1	182	81.3	33
2	177	75.4	26

6.2 Devices

Vicon-system (Oxford Metrics, Inc., Oxford UK) with 16 cameras (Vero v2.2) and Nexus (v.2.14) was used for marker-based 3D motion capture with sampling frequency of 200 Hz. A single floor mounted force plate (508x464mm, AMTI OR6-6-2000, AMTI Inc., Watertown, USA) was used to obtain GRF's and moment data during the trials at sampling frequency of 1000 Hz. Force plate data was collected in sync with the 3D marker data via the Vicon system using Vicon Lock Sync Box for analog devices.

Before the start of the data collection, all cameras of the Vicon system were zoomed and focused on the capture area, and unwanted reflections were masked. The cameras were calibrated with a T-shaped wand containing 5 reflective markers, and by using Vicon's default value of 1000 valid calibration frames for each camera. The Vicon system's volume origin was set to align with coordinate system of the force plate in a manner that kinematic and kinetic data was obtained in the same coordinate system. The floor level of Vicon system was calibrated to the surface of the force plate according to the Vicon manual to remove any possible offsets in the coordinate system of Vicon relative to the orientation and position of the force plate. The force plate was powered on an hour before starting the measurements to prevent force plate sensor values from drifting due to heating. Prior starting the data collection, force plate zero levels were calibrated through both the amplifier and Vicon system to eliminate any offset between the force plate's nominal output levels at rest and it's theoretical zero level.

6.3 BSIP models

In this study, three regression equation-based BSIP models included a 12-segment model (DEM) based on Dempster (1955) as reported by Winter (2009, 86), a 14-segment model (LEV) derived from data by Zatsiorsky et al. (1990a and 1990b) as adjusted by de Leva (1996), and a 16-segment model (DUM) presented by Dumas and Wojtusch (2018). The regression equations for these BSIP models are derived from data of different demographic groups: the DEM model is based on data from eight male cadavers with an average age of 69 years, the LEV model is based on gamma-mass scanning data from 100 active young males averaging 24 years of age, and the DUM model is developed from photogrammetry derived data of 31 individuals with an average age of 28 years. Among these three BSIP models, only the DUM model was used to

test the effect of the single plane assumption, as it is the only one that clearly defines all three segment axes and provides complete inertia tensors for each segment.

A total of 45 reflective markers with 14 mm diameter were placed on anatomical landmarks of the participants, and 18 virtual markers were calculated based on the physical markers. Physical marker placements and virtual marker calculations are provided in appendices 1 and 2. The marker data, including the virtual markers, were then used to define the endpoints, origins, and segment reference frames for each segment. Complete details of segment origins, endpoints, reference frames and their calculations are provided in appendix 3. For segment reference frames X-axis indicates anterior direction, Y-axis superior, and Z-axis lateral direction of the segment when standing in anatomical position. Only the longitudinal axes are reported for the segments of the DEM and LEV models, as the anterior and lateral axes are not clearly defined in these models for all the segments considering on how they should be applied for 3D studies (Dumas & Wojtusch 2018). Also, anterior and lateral axes were not necessary for these models in this study due to the assumption that the movement of the segments occurred solely parallel to the sagittal plane and that the medio-lateral axes were the principal axes of rotations.

In the BSIP models used in this study, there was a significant difference in the modelling of the trunk segment. In the DUM model, the trunk was divided into three segments: thorax, abdomen, and pelvis. In the DEM and LEV models, the trunk was modeled as a single segment. Although the original DEM and LEV models do offer inertial parameters for a multi-segment trunk, these parameters are not easily applicable for 3D motion analyses due to their inadequate endpoint or segment frame definitions based on anatomical landmarks. The definitions provided for single segment trunk however could be applied in 3D analyses for these models and were therefore used in this study.

In the DEM model, a decision was made to model the forearm and hand as a single segment, rather than separate segments. This approach was chosen because the markers did not adhere well to the originally defined position on the hand segments endpoint. Additionally, inertial values for the combined forearm and hand segment were available in Winter (2009, 86). Given that the hand segment accounts for only 0.6 % of the total body weight in the DEM model, using the combined segment was assumed to introduce minimal to no error to the overall analysis.

Segmental COM positions and masses data used for the DEM, LEV, and DUM models are reported in table 2. COM position of each segment is expressed as 3D vector in the segments' reference frame extending from the origin of the segment to the COM, scaled relative to the segment length. For the DEM and LEV models, where the COM of the segments is assumed to lie along the longitudinal axis, only the longitudinal percentages are provided. Y-axis refers to the longitudinal axis for all segments except for the foot segment, where X-axis is the longitudinal axis. For the DUM model, all three axes are reported, as for this model the COM is not assumed to lie solely on the longitudinal axis. Masses of the segments are reported as percentages of total body mass.

TABLE 2. Segment mass (percentage of total body weight), and segment COM (percentage of segment length) position in segment reference frames starting from segment origin for the DEM, LEV, and DUM models.

	DEM		LEV		DUM	
Segment	COM (Y-axis %)	Mass (%)	COM (Y-axis %)	Mass (%)	COM (X-, Y-, and Z- axis %)	Mass (%)
Head and neck	56.7[a]	8.1	49.98	6.94	2.0, 53.4, 0.1	6.7
Trunk	49.5	49.7	43.1	43.46	-	-
Thorax	-	-	-	-	0, -55.5, -0.4	30.4
Abdomen	-	-	-	-	17.6, -36.1, -3.3	2.9
Pelvis	-	-	-	-	-0.2, -28.2, -0.6	14.2
Upper arm	-43.6	2.8	-57.54	2.71	1.8, -48.2, -3.1	2.4
Forearm	-	-	-45.74	1.62	-1.3, -41.7, 1.1	1.7
Forearm and hand	-68.2	2.2	-	-	-	-
Hand	-	-	-79.0	0.61	8.2, -83.9, 7.5	0.6
Thigh	-43.3	10.0	-40.95	14.16	-4.1, -42.9, 3.3	12.3
Shank	-43.3	4.65	-43.95	4.33	-4.8, -41.0, 0.7	4.8
Foot	42.9[ab]	1.45	44.15[b]	1.37	50.2, -19.9, 3.4	1.2

[a] Adapted value from Dumas and Wojtusch (2018), [b] X-axis value

The radius of gyration values used in this study are reported in table 3, referenced to as K_{cg}, which is relative to the segment lengths as discussed in chapter 2.4. For the DEM and LEV models, the radius of gyration is reported only for the Z-axis, as for these models the WBAM values calculated were based on assumption that all motion occurred exclusively within the sagittal plane, and that the Z-axes of the segments were the principal axes of rotation. For the DUM model, complete inertia tensors are reported, including all three axes radius of gyration and the products of inertia for sagittal, transverse, and frontal planes.

TABLE 3. Segment radius of gyration (K_{cg}) values for the DEM, LEV, and DUM models

	DEM	LEV	DUM	
Segment	Z-axis K_{cg}	Z-axis K_{cg}	X-, Y-, and Z-axis K_{cg}	Sagittal (X, Y), transverse (X, Z) and frontal (X, Z) plane products of inertia
Head and neck	28.1[a]	30.3	28, 21, 30	-7, -2, 3
Trunk	40.6	38.4	-	-
Thorax	-	-	42, 33, 36	-11, 1, 3
Abdomen	-	-	54, 66, 40	11, -6, -5
Pelvis	-	-	102, 106, 96	-25, -12, -8
Upper arm	32.2	28.5	39, 13, 30	5, 3, -13
Forearm	-	27.6	28, 11, 28	8, -1, 2
Forearm and hand	46.8	-	-	-
Hand	-	62.8	61, 38, 56	22, 15, -20
Thigh	32.3	32.9	29, 15, 30	7, -2, -7
Shank	30.2	25.1	28, 10, 28	-4, -2 ,4
Foot	40.7[a]	25.7	22, 49, 48	17, -11, 0

[a] Adapted value from Dumas and Wojtusch (2018)

6.4 Protocol

Measurements were carried out in the biomechanics laboratory at the Faculty of Sport and Health Sciences in Jyväskylä. Both participants were instructed to perform three distinct types of jumps, completing 10 trials of each type after their own warm-up. The trial types included a counter movement jump (CMJ) with unrestricted movement of the upper extremities, a standing backwards somersault in tucked position (BF), and a standing forward somersault take-off mimicking jump (FJ), where negative WBAM is generated but a complete somersault is not performed. Figure 9 demonstrates a 3D motion capture-based stick figure illustration of each trial type. These trial types were selected based on their differing requirements for generating WBAM in the sagittal plane. CMJ was chosen because it theoretically requires no WBAM in the sagittal plane at take-off. BF was included due to strong positive WBAM requirement at take-off, and FJ for relatively strong negative WBAM at take-off. As the axes are defined by the right-hand rule, a positive WBAM indicates rotation that can be observed in the direction of a backward somersault, while a negative WBAM indicates rotation in the direction of a forward somersault in the sagittal plane.

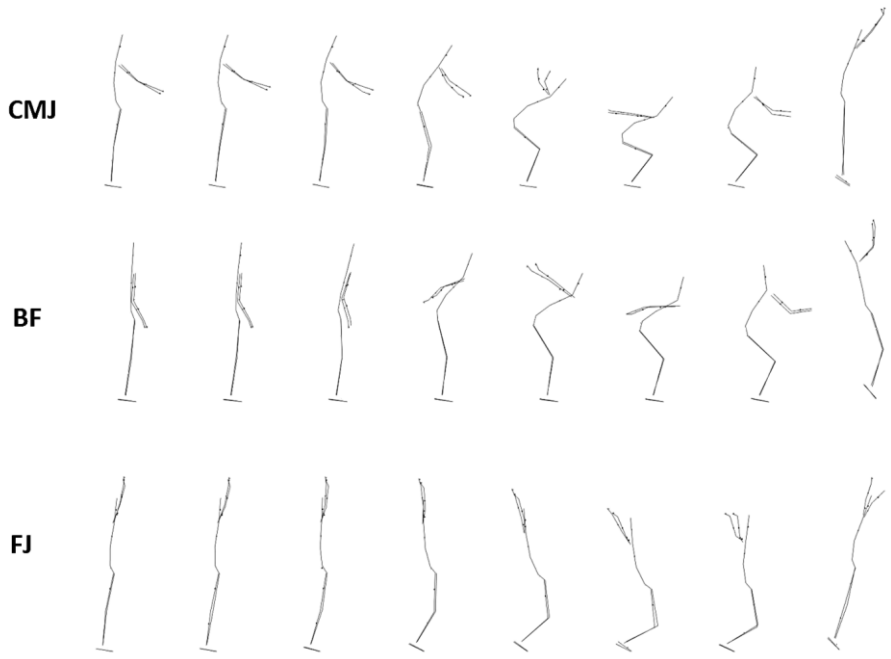

FIGURE 9**.** Sagittal plane illustrations of three different trial types used in the study**:** countermovement jump without restriction on the movement of upper extremities (CMJ), tucked backwards somersault (BF), and forward somersault take-off mimicking jump (FJ).

Participants were asked to execute each jump in a consistent manner across trials and to start the execution of the jumps from a stationary position. For the CMJ and FJ trials efforts were instructed to be comfortable and replicable rather than maximal, to ensure easier reproduction for the movements. For BF, participants were asked for their typical execution of the movement. To standardize the orientation of the participants during the trials, they were instructed to align their hip's medio-lateral axis as closely as possible with the Z-axis of the global coordinate system (GCS), the coordinate system in Vicon which had a fixed origin in laboratory space. The Y-axis of GCS was aligned vertically, and the X-axis was aligned in anterior-posterior direction relative to the participants' hip orientation. During the trials, the 3D trajectories of the attached markers and force plate data was captured with the Vicon system.

6.5 Data preprocessing

All marker trajectory data was initially labeled and gap filled in Vicon Nexus software. Following this, the force plate and marker data for all trials were exported as C3D files and imported into Matlab (R2023b) using custom C3D reader script. All subsequent preprocessing and analyses were conducted in Matlab with custom made scripts.

Kinematic data was filtered with fourth-order Butterworth filter with the cut-off frequency of 12 Hz after residual analysis (Winter 2009, 35 - 38). Force plate data was filtered with fourth-order Butterworth filter with a cut-off frequency of 50 Hz.

6.6 Kinematic method WBAM calculation

Kinematic method based total body WBAM, referred to as L_k, was calculated in the sagittal plane for all three BSIP models under the assumption that all motion occurred parallel to this plane. Segments were also assumed to be oriented in a way that the principal axis of rotation was the Z-axis during all the trials. L_k was calculated using the formula:

$$L_k = \sum_{s=1}^{S} I_s \omega_s + [\vec{r_s} \times m_s \vec{v_s}]$$

as described in chapter 2.1. equation 3. Sagittal plane was considered as the X-Y plane in the GCS.

For the DUM model, WBAM calculations in the sagittal plane were also conducted without relying on the single plane motion assumption. This approach was used to evaluate the accuracy of this assumption across trials performed in the study by using a BSIP model that clearly defines all three axes of the segments and provides complete inertia tensors for each segment. A full explanation of the methods used to calculate WBAM in the sagittal plane with and without the single plane assumption is provided in appendix 3. The main difference in calculations is that without the single plane assumption, the true orientation of the segments in considered in 3D space. This consideration can affect the moment of inertia values of the segments, impacting only the local terms of segmental angular momentum. Values obtained for the DUM model without relying on the single plane assumption are referred to as *DUM* $L_{k3d.}$

6.7 Trial onset definition

The definition of trial onset in this study involved using average WBAM values obtained by kinematic method using all three models. While vertical GRFs are commonly used for onset detection in various jumping activities (Conceição et al. 2022) they were not suitable for detecting the onset of WBAM generation during the trials of this study. WBAM generation was seen to accumulate prior to any significant observable changes in the GRFs, thus a customized onset definition method had to be used.

The onset for the trials was defined based on the WBAM values derived using the kinematic method. First, the average L_k values between the three BSIP models were calculated for each trial up to the moment of take-off. The trial-wise averages were then averaged again across all trials of each subject and trial type, producing a grand average representation of the signals for each subject. For the CMJ trials, the first point where the grand average L_k value crossed below a threshold of -1 kgm^2s^{-1} was then considered as the initial onset. The final onset for the CMJ trials was then defined as 100 ms prior to this initial onset (see figure 10).

For BF trials, a different approach was necessary for subject 2 due to the different technique used in generating WBAM compared to the CMJ trials. Unlike subject 1, who displayed a consistent L_k pattern at the beginning of both CMJ and BF trials, allowing the same onset method definition to be used for both, subject 2 showed an increase in L_k followed by a decline during BF trials. As a result, the threshold for defining the initial onset for subject 2's BF trials was set to 1 kgm^2s^{-1}. Final onset for subject 2 BF trials was then defined to be 100 ms prior to this initial onset (see figure 10).

In FJ trials, positive L_k values were observed in all trials by both participants, followed by a sharp decline. Therefore, a threshold of 1 kgm^2s^{-1} was used for defining the initial onset in FJ trials, with final onset 100 ms prior to this. Generally, the L_k values of FJ trials were observed to be less stable prior to the defined onset compared to those seen in CMJ and BF trials (see figure 10).

Take-off for all the trials was considered as the last sample where vertical GRF was greater than 100 N. As the accuracy of COP estimation derived from force plate data decreases when the vertical force is low (Chockalingam et al. 2002), a relatively high vertical force threshold was used in this study to keep the COP errors minimal. The durations of the trials using the described onset and take-off definitions were as follows for subject 1: 925 ms, 905 ms, and 795 ms for CMJ, BF, and FJ trials, respectively. For subject 2, these values were 1175 ms, 1865 ms, and 1140 ms for CMJ, BF, and FJ trials, respectively.

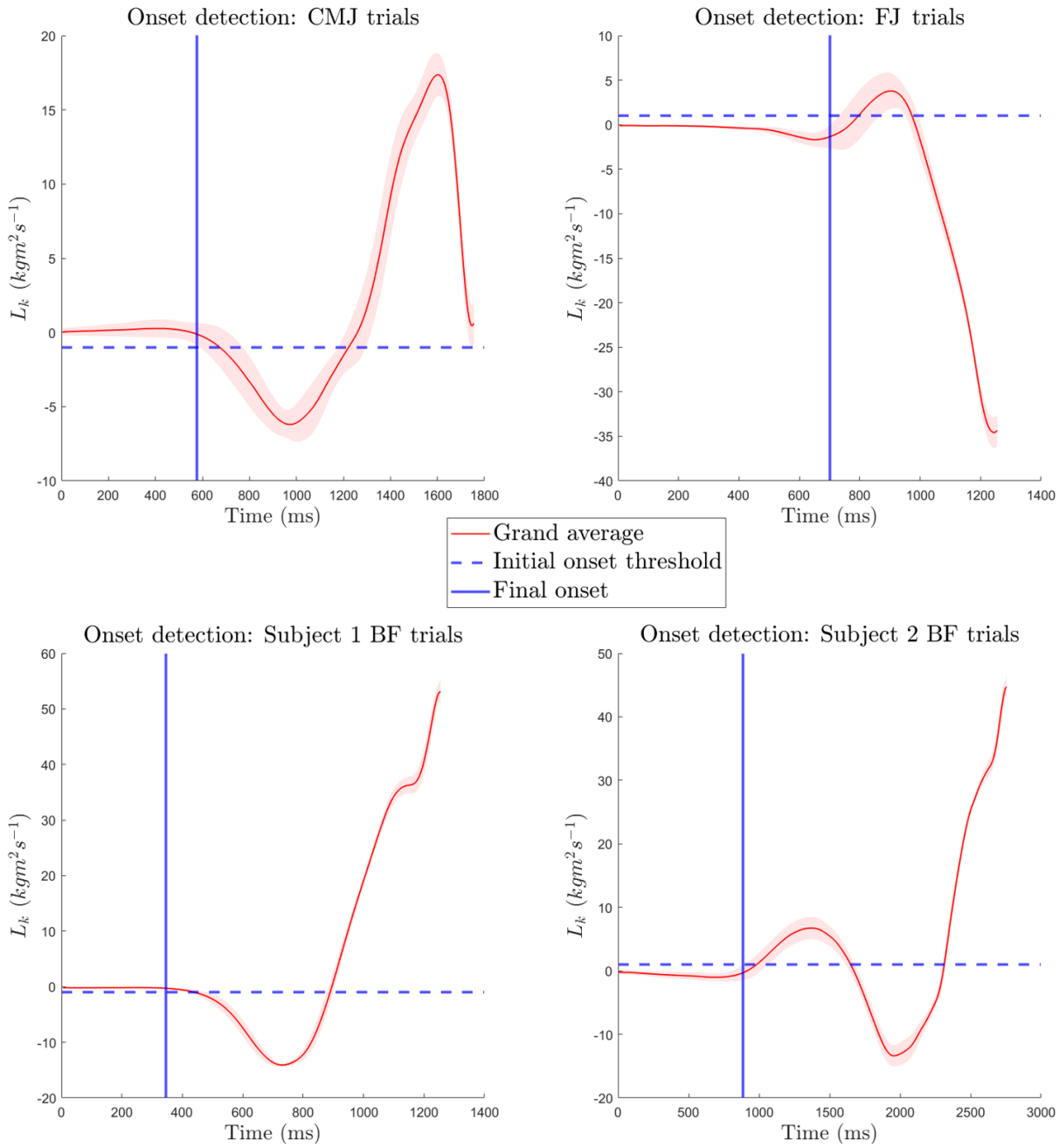

FIGURE 10. Definition of onset for CMJ trials, FJ trials, subject 1 BF trials, and subject 2 BF trials. The solid red line indicates the grand average WBAM across all trials obtained using the kinematic method, with the shaded red area indicating standard deviation. The blue dotted horizontal line marks the initial onset threshold, while the solid vertical blue line shows the final defined onset for each trial type. Data of subject 2 is presented for CMJ trials, and data of subject 1 for the FJ trials.

6.8 Impulse method WBAM calculation

To obtain torque generated by GRFs about the total body COM, COP position data was first calculated according to manufacturer's documentation based on the GRFs and moment data collected with the force plate. COP and GRF data were subsampled from 1000 Hz to 200 Hz to match the sampling frequency of the kinematic recordings.

Torque about total body COM in sagittal plane, denoted as τ, was calculated for all three BSIP models based on the recorded GRFs and the position vector extending from each models' estimation of total body COM to COP, represented as $\vec{r}$. The torque was calculated using the equation $\tau = r_x F_y - r_y F_x$, where r_x and r_y are the horizontal (X-) and vertical (Y-) components of $\vec{r}$, respectively, and F_x and F_y are the X- and Y-components of the GRFs. Examples of r_x and r_y time series data from BF trials are presented in figure 11.

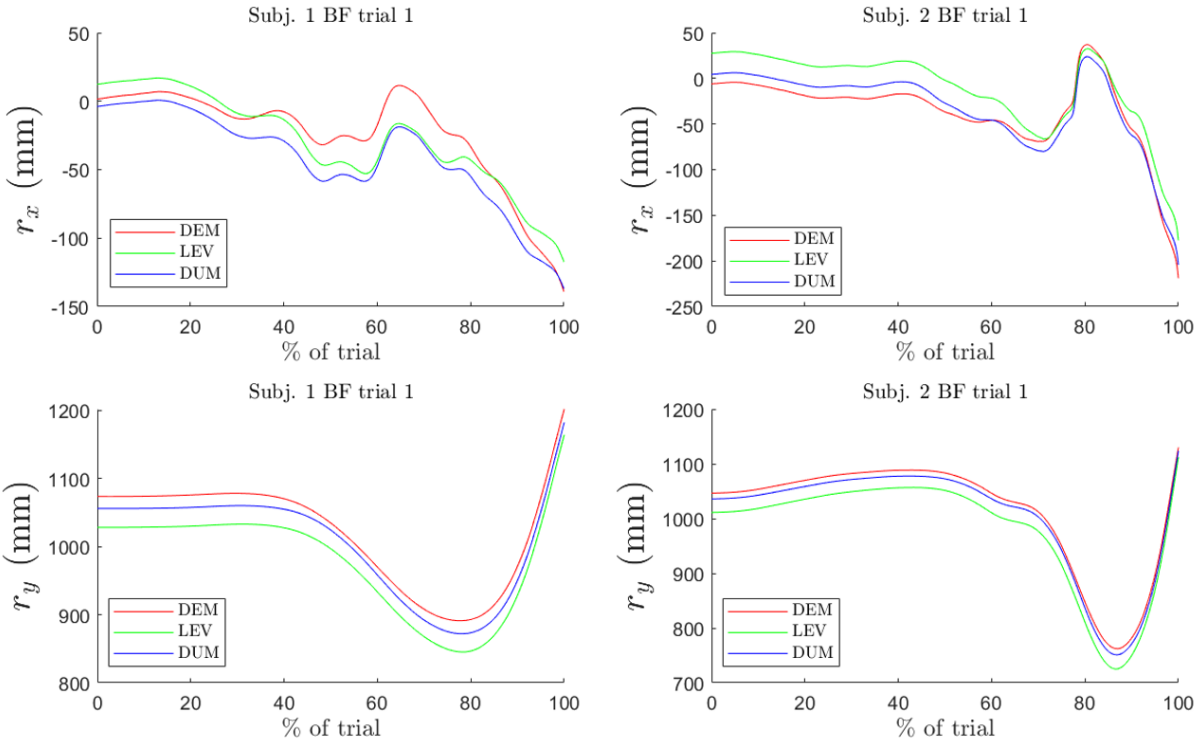

FIGURE 11. Timeseries r_x and r_y data from first BF trials of both subjects for the DEM, LEV, and DUM models. Positive r_x values indicate COM being positioned anteriorly relative to COP.

To obtain the change in WBAM about total body COM using the impulse method, referred to as L_t, torque was integrated over time from the defined onset until the take-off. To account for the residual WBAM observed at the onset of the trials due to the definition methods used, the initial WBAM at this moment was determined by averaging the values obtained from the DEM, LEV, and DUM models for each trial at that specific time point. These initial WBAM values were calculated based on the results from the kinematic method to ensure a standardized baseline for evaluating the changes in WBAM during the trials, as these values were not precisely zero at the moment of onset.

After calculating the kinematic and impulse derived WBAM values, the values were time normalized by scaling them from 0 to 100 % using linear interpolation in steps of 1 %. Time normalization was conducted between the defined onset until the take-off.

6.9 Statistical analysis

In the statistical analysis, differences between sagittal plane total body WBAM obtained with the kinematic and the impulse methods using the BSIP models of DEM, LEV, and DUM were compared. The use of three BSIP models and two calculation methods resulted in six unique model-method combinations for each trial type: *DEM* L_k, *LEV* L_k, *DUM* L_k, *DEM* L_t, *LEV* L_t, and *DUM* L_t, where L_k refers to kinematic method and L_t to the impulse method.

To determine the differences between *DEM* L_k, *LEV* L_k, *DUM* L_k, *DEM* L_t, *LEV* L_t, and *DUM* L_t WBAM values, the mean absolute differences (MAD) between each pair of WBAM time series signals were calculated, resulting in 15 pairwise MAD values per trial. These MAD values were then averaged across all trials of the same type for each subject individually, providing an overall measure of the differences between the model-methods for each trial type. To assess the impact of the single plane assumption, the MAD values were also calculated between the *DUM* L_k (single plane) and *DUM* L_{k3d} (true 3D orientation) values.

Statistical parametric mapping (SPM, Friston et al., 1994) was used to analyse the statistical differences in WBAM time series data between all the model-method combinations with a two-tailed paired t-test (α=0.05). In this approach, a t-test is performed at each time point, and Random Field Theory (Adler & Taylor 2007) is applied to determine a threshold test value, which

is calculated based on the significance level and the smoothness of the data. SPM in this context refers to the methodological approach, and SPM{t} to the scalar trajectory variable which is calculated at each individual time node. When the SPM{t} exceeds a predetermined threshold, it can be inferred that there is only a 5 % probability (α=0.05) that random curves could produce such crossing at that specific time. Rather than assigning a p-value to each time, an overall p-value is calculated for supra-threshold clusters. Supra-threshold clusters refer to a cluster of adjacent points which are exceeding the threshold value. The p-values for the supra-threshold clusters refer to the probability with which these clusters could have been produced by a random field process with the same temporal smoothness. SPM represents a relatively novel statistical technique in the field of biomechanics, and it allows the graphical presentation of time series data alongside statistical results, which makes the interpretation of the findings easier. All SPM analyses were conducted by using open-source SPM1D code (version M.0.4.10) in Matlab.

7 RESULTS

Take-off WBAM values of *DEM* L_k, *LEV* L_k, *DUM* L_k, *DEM* L_t, *LEV* L_t, and *DUM* L_t from CMJ, FJ, and BF trials for subject 1 and subject 2 are presented in figures 12 and 13.

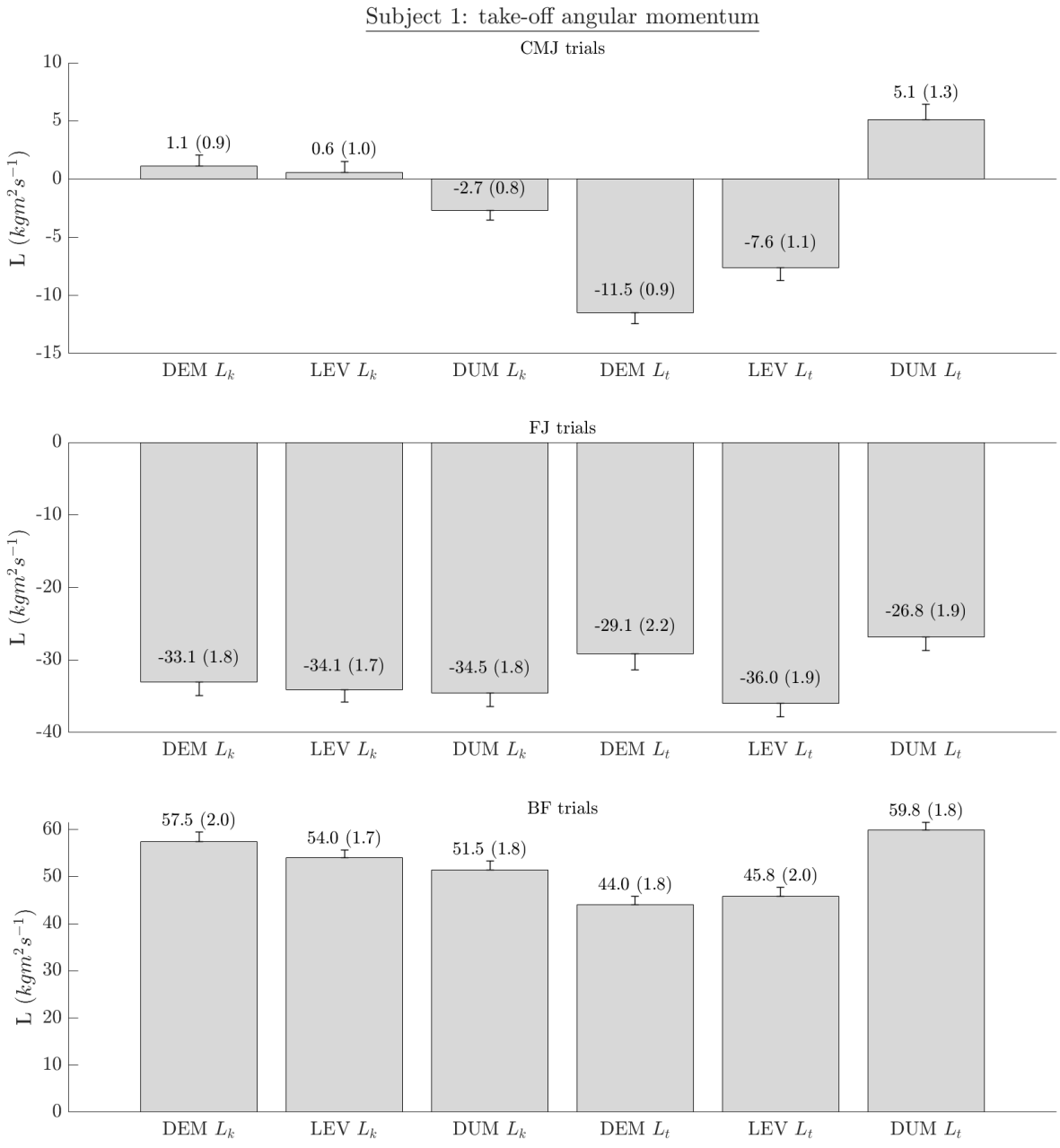

FIGURE 12. Subject 1 mean (SD) take-off WBAM values of *DEM* L_k, *LEV* L_k, *DUM* L_k, *DEM* L_t, *LEV* L_t, and *DUM* L_t from CMJ, FJ, and BF trials.

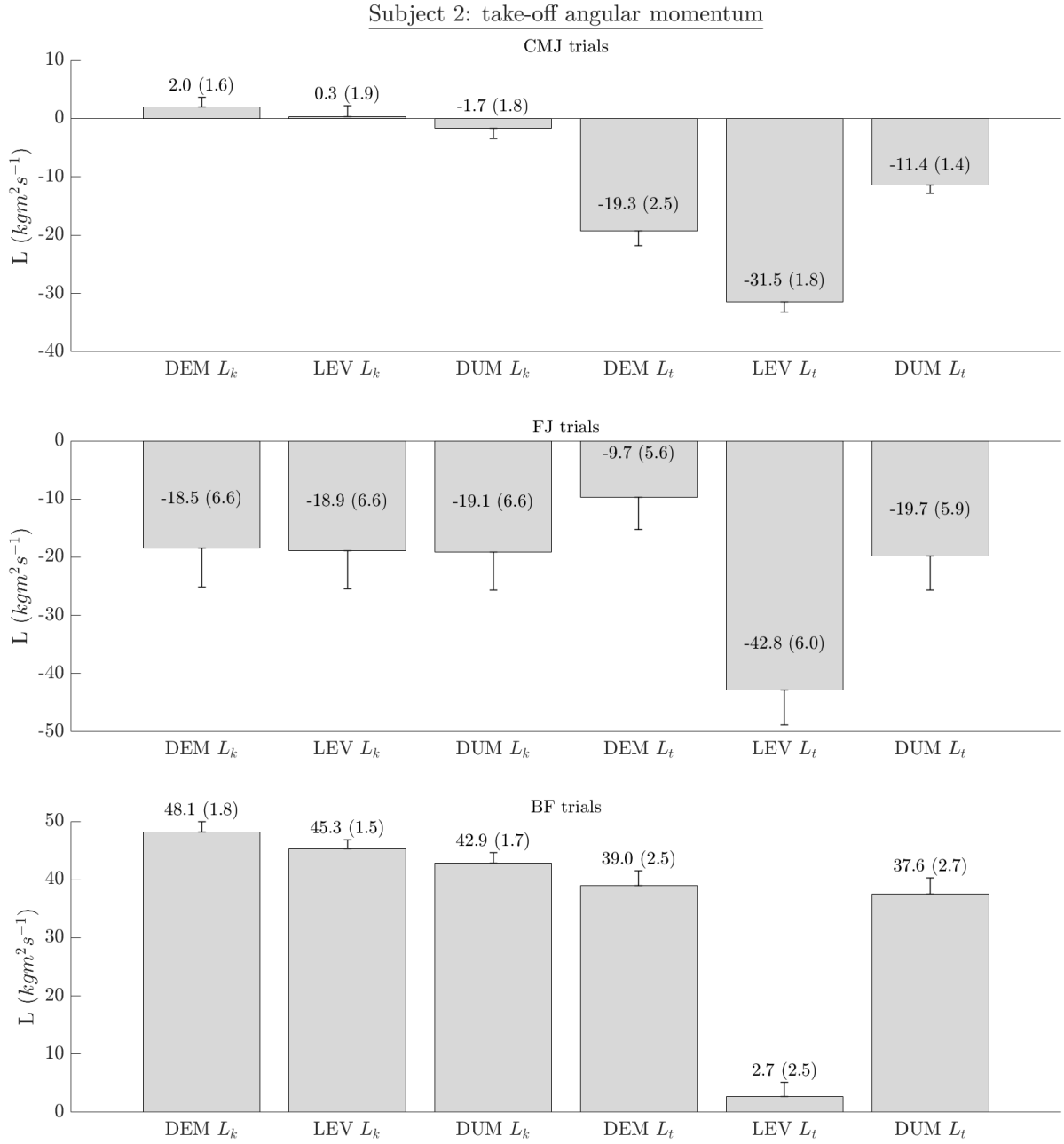

FIGURE 13. Subject 2 mean (SD) take-off WBAM values of *DEM L_k*, *LEV L_k*, *DUM L_k*, *DEM L_t*, *LEV L_t*, and *DUM L_t* from CMJ, FJ, and BF trials.

Figure 14 presents heatmaps of average MADs between *DEM L_k*, *LEV L_k*, *DUM L_k*, *DEM L_t*, *LEV L_t*, and *DUM L_t* for each trial type and both subjects.

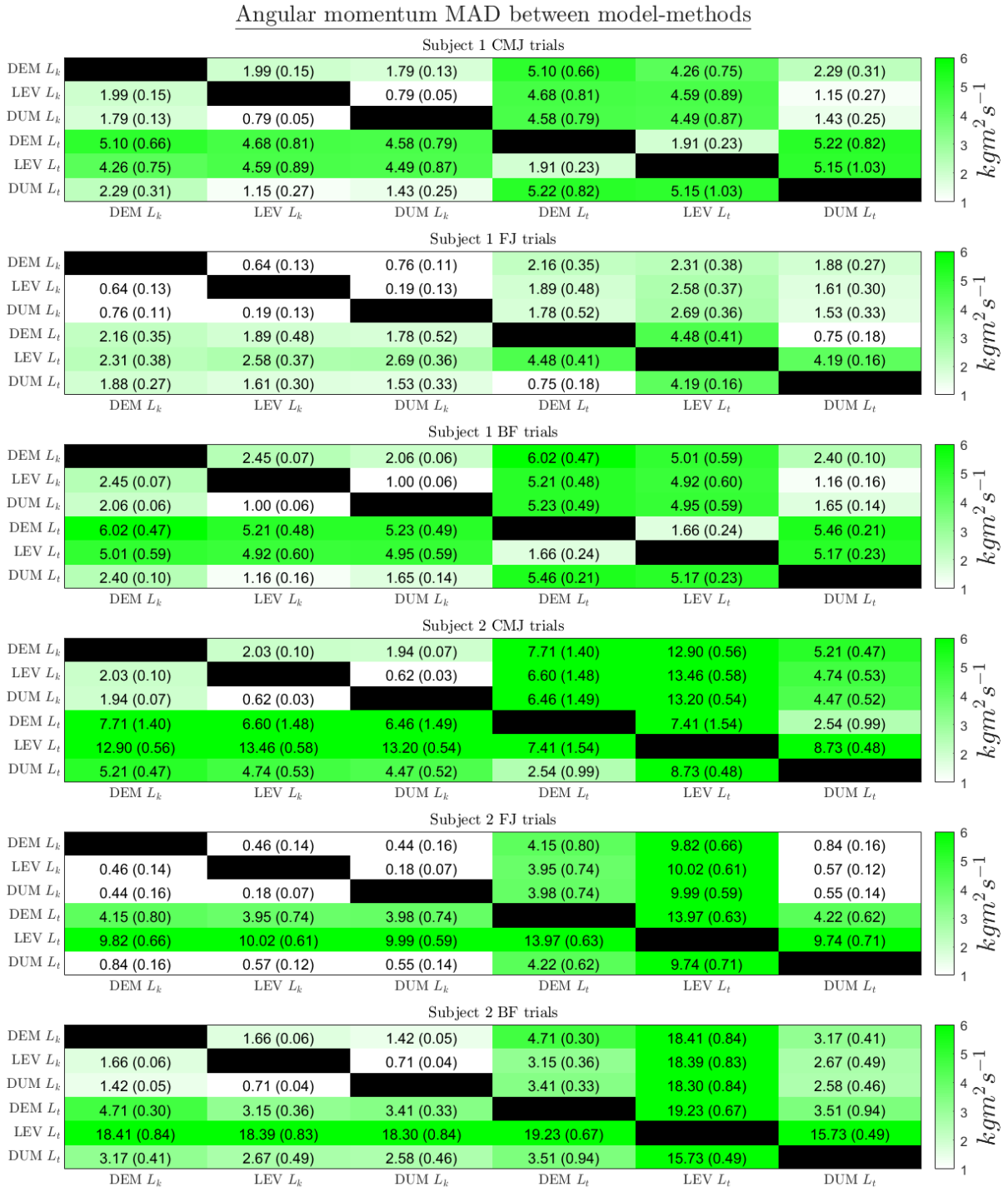

FIGURE 14. Average MAD (SD) between *DEM* L_k, *LEV* L_k, *DUM* L_k, *DEM* L_t, *LEV* L_t, and *DUM* L_t for each trial type. Rows and columns from 1 to 3 of each heatmap correspond to values obtained using the kinematic method, while rows and columns from 4 to 6 represent values from the impulse method. Darker shades of green indicate larger MADs. Black cells represent pairwise comparison of model-method combination to itself.

SPM paired t-test results, together with WBAM time series data across all trial types for both subjects, are presented in figures 15–20. At least one supra-threshold cluster was observed in each pairwise SPM t-test conducted, indicating significant differences between the model-methods at these points in time. Table 4 quantifies the coverage of supra-threshold cluster relative to the trial duration, reflecting the proportions of the trials during which significant differences were detected via the SPM paired t-test. 100 % refers that the values between model-methods were significantly different throughout the entire trial, while 0 % indicates no significant difference at any point. The percentages do not reflect on the effect size of the observed differences.

TABLE 4. Percentages of the total trial durations where supra-threshold clusters were observed via the SPM paired t-test.

Model-method comparison	Subj. 1 CMJ	Subj. 1 FJ	Subj. 1 BF	Subj. 2 CMJ	Subj. 2 FJ	Subj. 2 BF
DEM L_k - *LEV* L_k	82	86	83	65	22	40
DEM L_k - *DUM* L_k	86	90	81	77	16	56
DEM L_k - *DEM* L_t	41	90	72	72	71	53
DEM L_k - *LEV* L_t	68	98	77	98	99	99
DEM L_k - *DUM* L_t	73	100	62	56	49	44
LEV L_k - *DUM* L_k	59	1	51	25	16	29
LEV L_k - *DEM* L_t	61	98	66	37	79	34
LEV L_k - *LEV* L_t	100	100	100	100	100	100
LEV L_k - *DUM* L_t	7	56	35	62	37	60
DUM L_k - *DEM* L_t	60	97	73	37	85	39
DUM L_k - *LEV* L_t	100	98	100	100	100	100
DUM L_k - *DUM* L_t	8	51	40	59	40	42
DEM L_t - *LEV* L_t	90	100	83	100	100	100
DEM L_t - *DUM* L_t	81	83	100	61	100	61
LEV L_t - *DUM* L_t	100	100	100	100	100	100

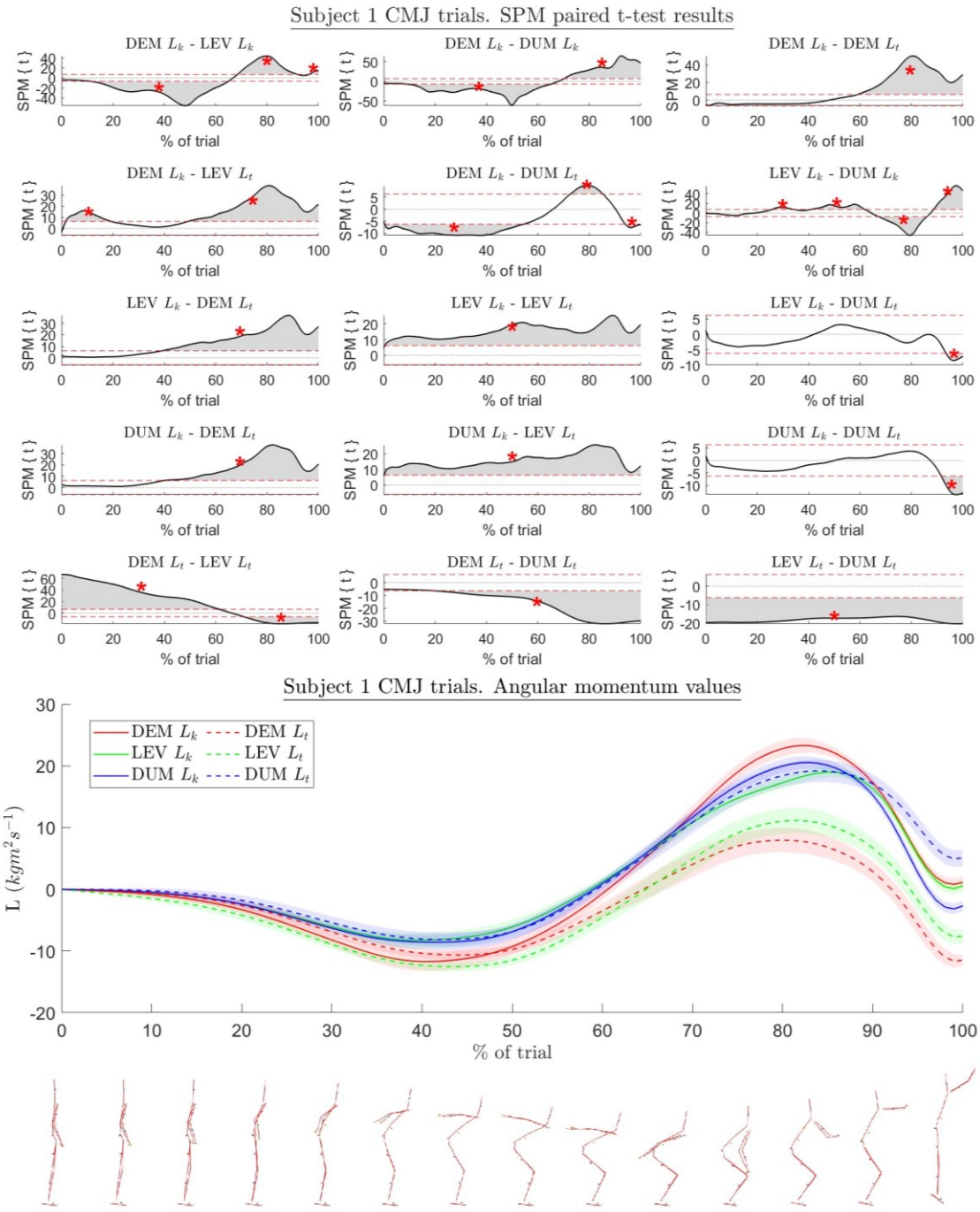

FIGURE 15. Top panel displays the results from all 15 pairwise SPM paired t-tests (α=0.05) for subject 1 during CMJ trials between the six model-method combinations. The dotted red line represents the threshold for statistically significant difference, while the grey area indicates a supra-threshold cluster that exceeds the threshold ($p<0.05$). All individual supra-threshold clusters are marked with a red asterisk. Below, WBAM time series data for each of the six model-method approaches are shown. A clouded area around each signal indicates the standard deviation. Stick figure illustration is provided for a visual representation of the trials performed by the subject.

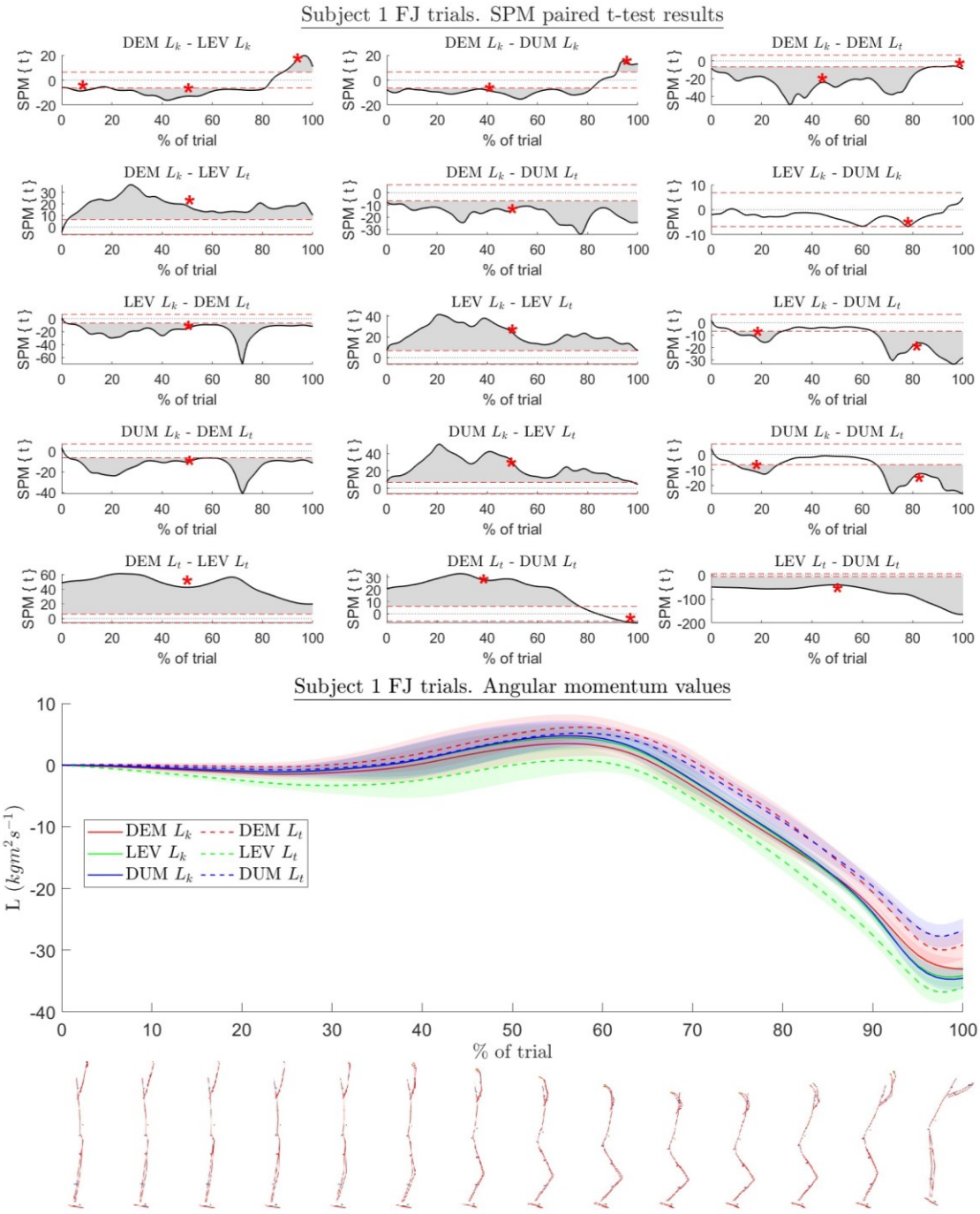

FIGURE 16. Top panel displays the results from all 15 pairwise SPM paired t-tests (α=0.05) for subject 1 during FJ trials between the six model-method combinations. The dotted red line represents the threshold for statistically significant difference, while the grey area indicates a supra-threshold cluster that exceeds the threshold ($p<0.05$). All individual supra-threshold clusters are marked with a red asterisk. Below, WBAM time series data for each of the six model-method approaches are shown. A clouded area around each signal indicates the standard deviation. Stick figure illustration is provided for a visual representation of the trials performed by the subject.

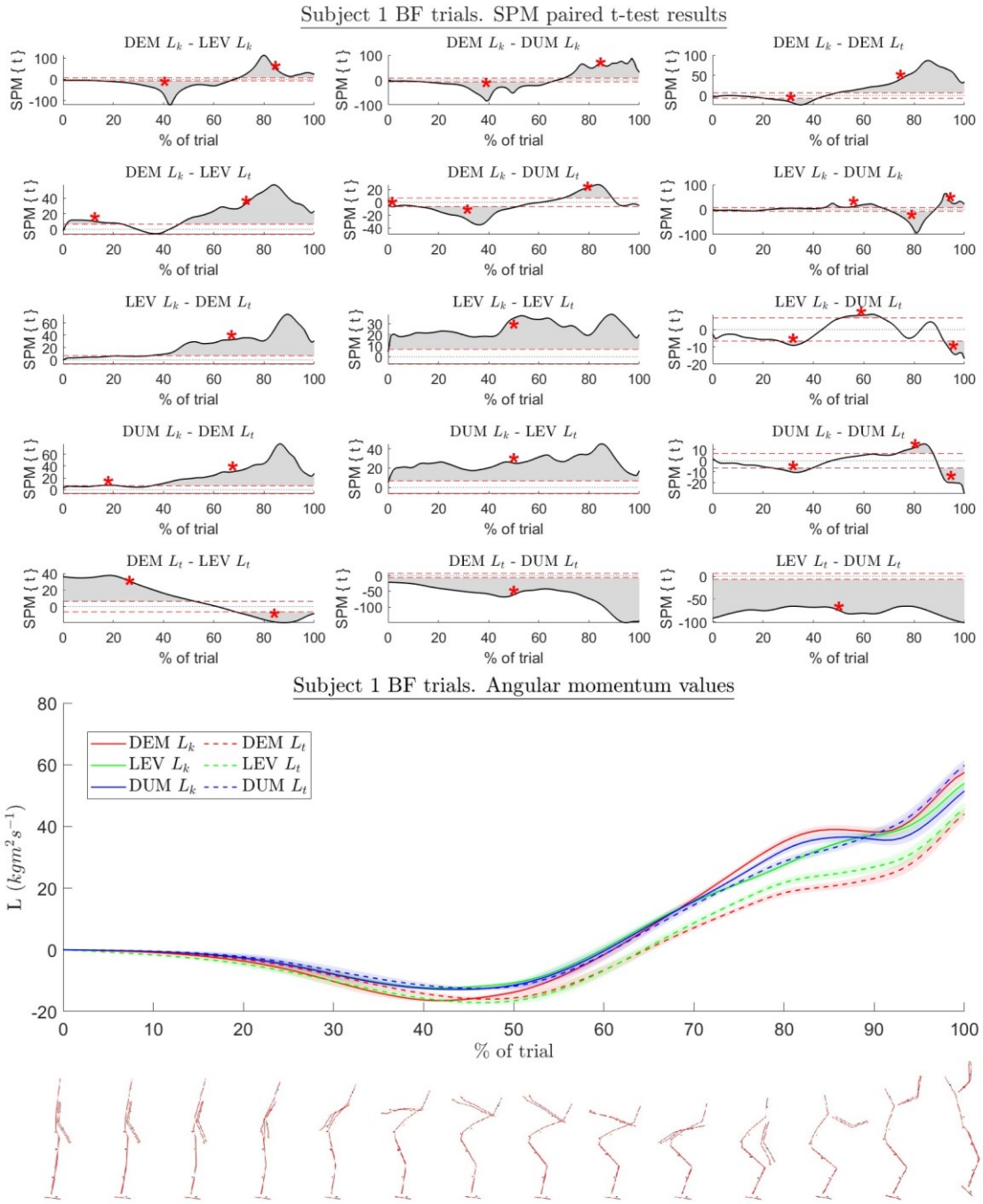

FIGURE 17. Top panel displays the results from all 15 pairwise SPM paired t-tests (α=0.05) for subject 1 during BF trials between the six model-method combinations. The dotted red line represents the threshold for statistically significant difference, while the grey area indicates a supra-threshold cluster that exceeds the threshold ($p<0.05$). All individual supra-threshold clusters are marked with a red asterisk. Below, WBAM time series data for each of the six model-method approaches are shown. A clouded area around each signal indicates the standard deviation. Stick figure illustration is provided for a visual representation of the trials performed by the subject.

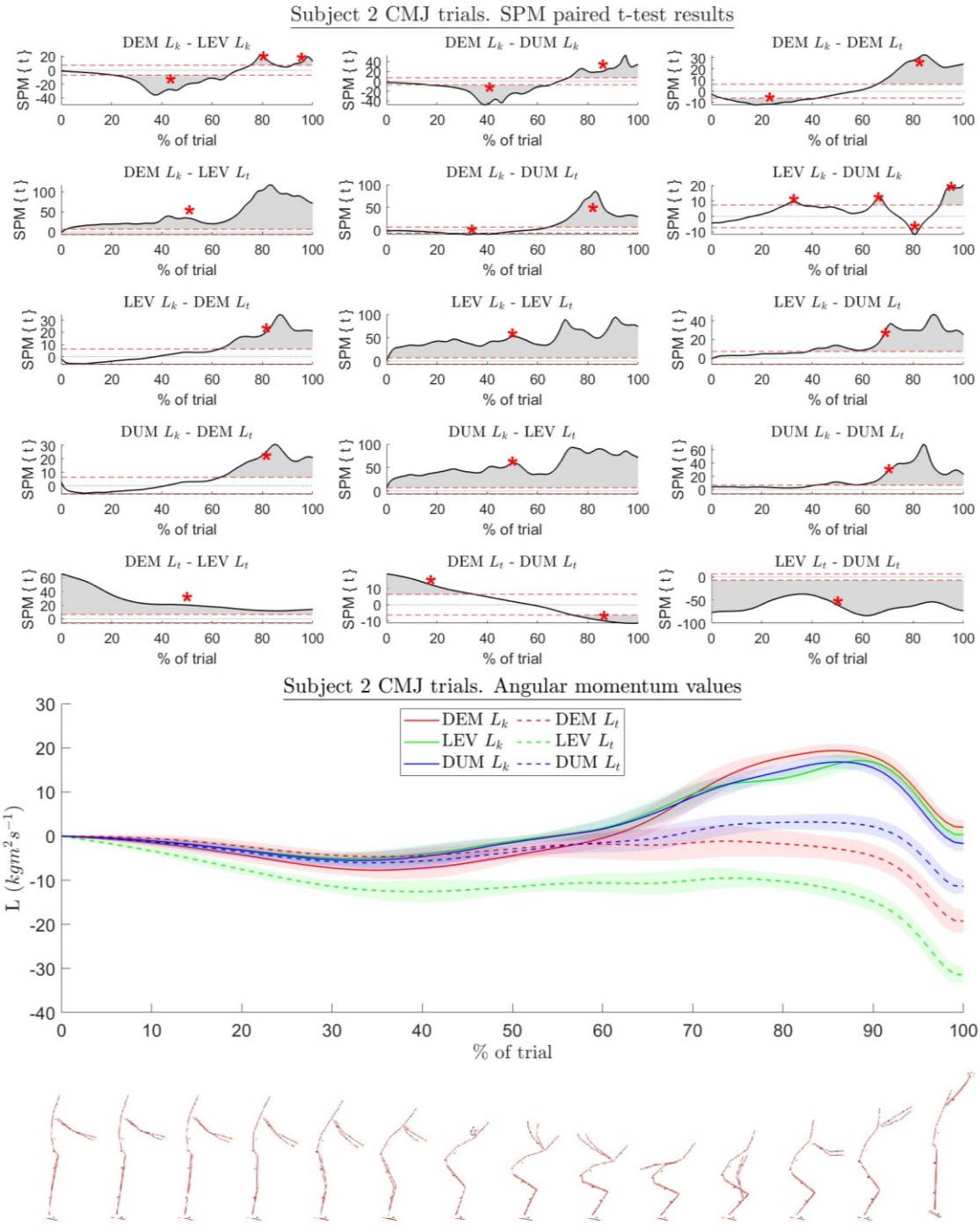

FIGURE 18. Top panel displays the results from all 15 pairwise SPM paired t-tests (α=0.05) for subject 2 during CMJ trials between the six model-method combinations. The dotted red line represents the threshold for statistically significant difference while the grey area indicates a supra-threshold cluster that exceeds the threshold ($p<0.05$). All individual supra-threshold clusters are marked with a red asterisk. Below, WBAM time series data for each of the six model-method approaches are shown. A clouded area around each signal indicates the standard deviation. Stick figure illustration is provided for a visual representation of the trials performed by the subject.

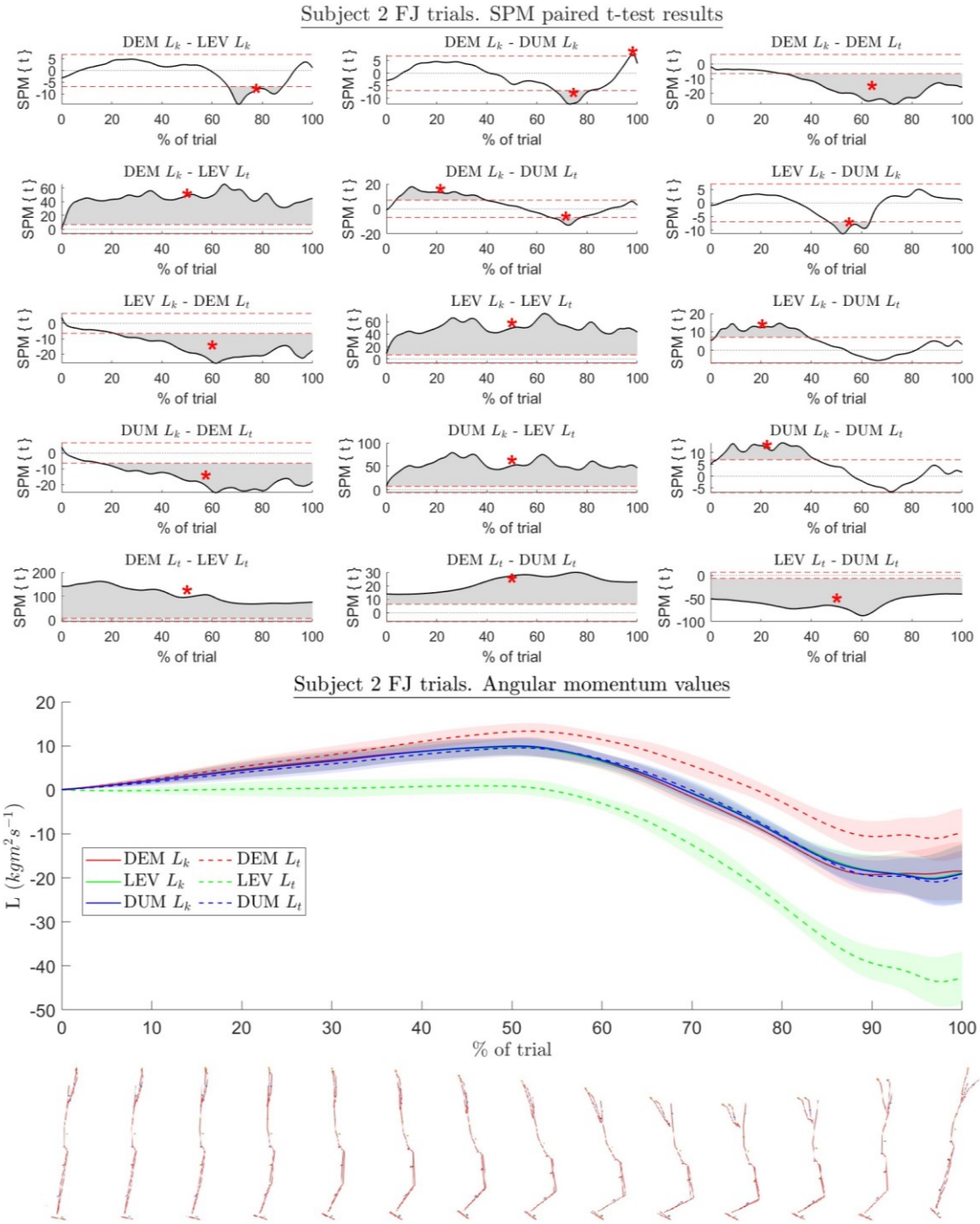

FIGURE 19. Top panel displays the results from all 15 pairwise SPM paired t-tests (α=0.05) for subject 2 during FJ trials between the six model-method combinations. The dotted red line represents the threshold for statistically significant difference, while the grey area indicates a supra-threshold cluster that exceeds the threshold ($p<0.05$). All individual supra-threshold clusters are marked with a red asterisk. Below, WBAM time series data for each of the six model-method approaches are shown. A clouded area around each signal indicates the standard deviation. Stick figure illustration is provided for a visual representation of the trials performed by the subject.

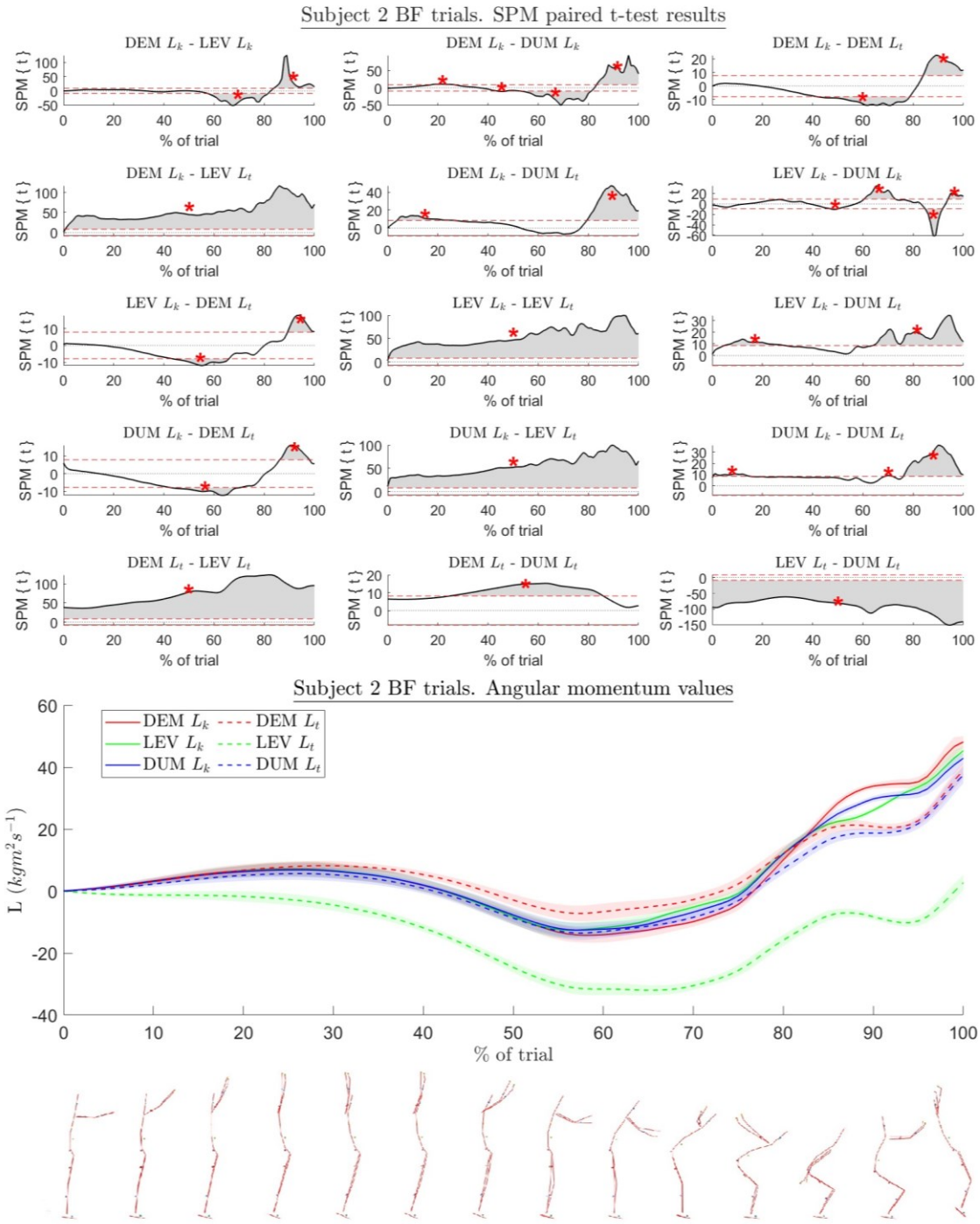

FIGURE 20. Top panel displays the results from all 15 pairwise SPM paired t-tests (α=0.05) for subject 2 during BF trials between the six model-method combinations. The dotted red line represents the threshold for statistically significant difference, while the grey area indicates a supra-threshold cluster that exceeds the threshold ($p<0.05$). All individual supra-threshold clusters are marked with a red asterisk. Below, WBAM time series data for each of the six model-method approaches are shown. A clouded area around each signal indicates the standard deviation. Stick figure illustration is provided for a visual representation of the trials performed by the subject.

Between *DEM* L_k and *DEM* L_{k3d} the MADs for subject 1 were: 0.01 for CMJ trials, 0.06 for FJ trials, and 0.01 for BF trials. Corresponding MADs for subject 2 were: 0.02 for CMJ trials, 0.02 for FJ trials, and 0.03 for BF trials.

SPM paired t-test (α=0.05) was conducted between *DEM* L_k and *DEM* L_{k3d} for subject 1 FJ trials where the largest MAD was observed. No supra-threshold cluster were observed exceeding the threshold (figure 21), indicating no statistically significant difference in WBAM values during these trials with or without the single plane assumption.

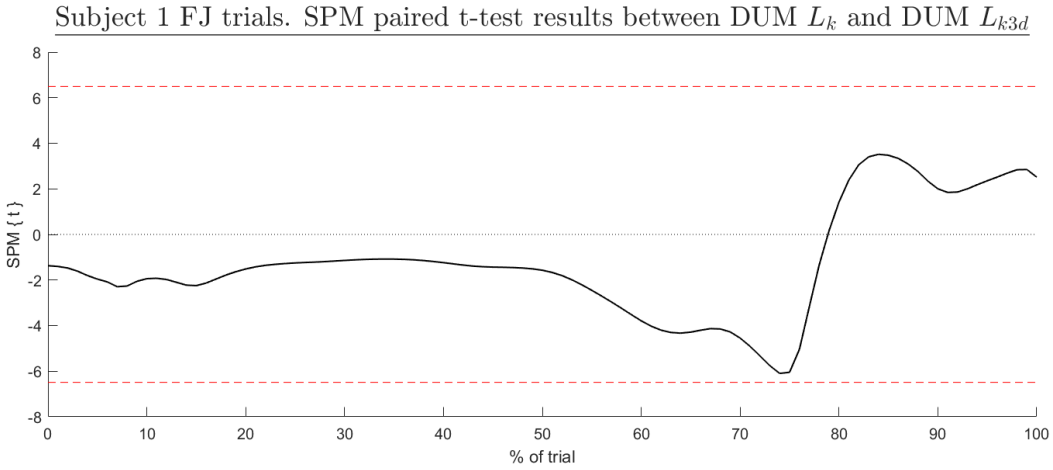

FIGURE 21. SPM paired t-test results (α=0.05) between *DEM* L_k and *DEM* L_{k3d} for subject 1 FJ trials. The dotted red line represents the threshold for statistically significant difference.

8 DISCUSSION

The first hypothesis in study was that the WBAM values derived from the kinematic and the impulse methods would yield to significantly different results if the same BSIP model was used, and that these differences between results would likely be influenced also by the choice of BSIP model. As hypothesized, significant methodological differences were observed in WBAM values between the calculation methods in each SPM paired t-tests when comparing kinematic and impulse derived WBAM values within the same BSIP models. Although significant differences were found during all trial types between all models, out of the three BSIP models used in the study, the DUM model demonstrated the lowest MADs (figure 14) and the shortest total duration of suprathreshold clusters in SPM paired t-tests for both subjects (table 4). This suggests better consistency between the kinematic and the impulse method within this BSIP model. The worst performance in terms of supra-threshold cluster duration was with the LEV model (100 % for all trial types for both subjects), and the LEV model performed the worst also on MAD metric for subject 2. For subject 1, the largest MAD was observed for the DEM model in CMJ and BF trials, but for FJ trials largest MAD was observed with the LEV model (figure 14).

The second research question was how the results of kinematic and impulse calculation methods vary across different BSIP models when the calculation methods are applied independently. As hypothesized, significant differences in WBAM values were also observed among the BSIP models based on the SPM paired t-tests (figures 15–20), with the magnitudes varying depending on which comparisons were made. Although both calculation methods demonstrated significant differences between the BSIP models, contrary to the hypothesis the kinematic method yielded on average more consistent WBAM values across the models based on MADs (figure 14) and the total supra-threshold cluster durations. While not a statistical outcome, the differences in MAD values between the calculation methods were evident.

For subject 1, the behavior of impulse based WBAM values varied across different trial types without a clear consistent pattern. During CMJ trials, *DEM* L_t and *LEV* L_t produced fairly consistent results, with MAD of 1.91. *DUM* L_t values aligned more closely with the kinematic results than with other impulse results in these trials. In contrast, during FJ trials *DEM* L_t and *DUM* L_t values were closely matched (MAD 0.75), but *LEV* L_t values were consistently more negative throughout the trials. During BF trials, however, *DEM* L_t and *LEV* L_t values showed better alignment, while *DUM* L_t values remained higher than these two throughout the trials.

Interestingly, for subject 2, the *LEV* L_t values were significantly lower than those of any other model-method combinations throughout all three trial types. The magnitudes of these differences were considerable, as apparent in figures 15–20 and in the figure 14 heatmaps. However, no clear trend was observed between *DEM* L_t and *DUM* L_t values across the three trial types for subject 2.

After take-off, no more WBAM can be generated as the only external force acting on the body is the gravitational force. Therefore, WBAM at take-off can be considered as the 'final' result of the calculations. In the SPM paired t-test at this time point, significant differences were observed between most comparisons (figures 15–20). However, the magnitudes of these differences varied. For certain model-method combinations (e.g. subject 1 FJ trials between *DEM* L_k and *LEV* L_k) although significant difference was observed at the moment of take-off, the absolute differences between the values were rather small (1 kgm^2s^{-1} between the mean values) considering the overall scale of the values (>33 kgm^2s^{-1} with both model-methods). Generally, the WBAM values at the take-off were more closely aligned when comparing the kinematic method values than the impulse method values (figures 12–13 and 15–20).

In this study it was assumed that the motion of the segments during the trials occurred purely parallel to the sagittal plane, with the medio-lateral axis being the principal axis of rotation. This assumption did not result in significant differences in the WBAM values for the trials performed in this study. The largest MAD observed between the *DUM* L_k and *DUM* L_{k3d} across all trial types was only 0.06, and no significant differences were found in SPM paired t-test. These results support the validity of this simplifying assumption for calculating comparable WBAM values within the scope of this study. However, this assumption was only tested using the DUM model, where the definitions of segment axes were suitable for 3D analysis of segments' orientations. It remains unclear how this assumption impacted the WBAM values with the DEM and LEV models. As this assumption can only affect the local terms of segmental angular momentum, it can be hypothesized to produce minimal errors for these models as well.

8.1 Insights based on the results

Kinematic method considerations. Based on the findings of this study, it seems that the kinematic method provided rather comparable WBAM values for both subjects, and the impulse

method results were generally more comparable for subject 1 trials than for subject 2 trials, where the impulse method produced erratic values especially for the LEV model. While the 'ground truth' remains unknown, it seems that the kinematic method could be the better approach in determining WBAM, at least in terms of consistency. As none of the three BSIP models used in this study were based on individualised data from the participants, it remains unknown how these two calculation methods would compare if an individualised BSIP model was used. Using individualised BSIP models could potentially lead to more consistent WBAM values between the kinematic and the impulse methods.

Generally, more distal segments contribute mainly to the remote terms of angular momentum rather than local terms (Kwon, 1996). Therefore, differences in mass estimates of these segments were likely a significant factor affecting the kinematic results across the BSIP models. The combined mass of the upper extremities (upper arms, forearms, and hands) is slightly higher in the DEM model (10 %) compared to the LEV model (9.88 %) and the DUM model (9.4 %). Also, for the DEM model, the head segment has notably larger mass than the LEV or DUM models (DEM 8.1 %, LEV 6.94 %, DUM 6.7 %). The largest difference in total mass between the segments is with the thigh segment, where the combined mass of both thighs for DEM is only 20 %, whereas it is 28.32 % for the LEV model and 24.6 % for the DUM model. The differences in trunk segment across the BSIP models are also notable. In the DEM model, the trunk segment accounts for 49.5 % of the total mass compared to only 43.46 % in the LEV model. The DUM model segments the trunk into three distinct parts (thorax, abdomen, and pelvis), with a combined mass of 45.7 %.

In Kwon's 1996 study, differences of up to 11.3 % were observed between various BSIP models in determining WBAM with the kinematic method during double somersault high bar dismounts. Similarly, in this study, the largest observed differences in mean WBAM values at the moment of take-off during BF trials also approximated 11.5 %, with the biggest variance noted between the DEM and DUM models. Schüler et al. (2016) reported the largest difference in mean values between individualised BSIP models and the Hanavan (2016) model during 1½ tucked back somersaults to be 14.5 % among the three participants of their study. Based on these findings, it seems that up to 15 % differences can be expected in kinematic based WBAM values during somersaulting tasks, depending on the choice of the BSIP model. During different types of tasks such as the CMJ trials of this study, the percentage-wise differences in WBAM

between the BSIP models tend to be significantly larger due to the smaller absolute values involved.

Overall kinematic method derived take-off WBAM values during BF trials in this study were smaller than those reported by Król et al. (2016) (57.9 – 63.4 kgm^2s^{-1}), and closer to those reported in Król et al. (2020) (53.1±8.2 kgm^2s^{-1}). However, COM vertical velocities at take-off in this study (2.89±0.11 ms^{-1} for subject 1 and 2.73±0.16 ms^{-1} for subject 2, as calculated using the DUM model) were higher than of those reported in both Król et al. (2014) (between 2.38 ms^{-1} and 2.52 ms^{-1}) and Krol et al. (2020) (2.32±0.21 ms^{-1}). These higher velocities, combined with individual differences and different BSIP estimation methods, can explain these lower WBAM values observed in this study.

On impulse method and COM estimates. The results for subject 2 raise concerns about the reliability of the impulse method for determining WBAM values. The absence of 'ground truth' WBAM values makes it difficult to estimate the accuracy of the results. However, it is clear for example that the mean WBAM of 2.7 kgm^2s^{-1} obtained for LEV model at take-off for backward somersaults would be insufficient for performing the necessary rotations required for the task. Also, the impulse method showed substantially larger variations than the kinematic method between all trial types for both subjects.

When results from different studies are compared, the reliability of the methods used for determining WBAM is important. The kinematic method seems to produce more consistent results than the impulse method, irrespective of the chosen BSIP model. Given the various BSIP estimates available and the often-unknown accuracy of these estimates, the kinematic method seems to be the better approach to determine the WBAM values, as potential differences between the BSIP estimates seems to have smaller impact on the outcomes with this method.

What could explain the differences in consistency between these two methods for determining WBAM? One key difference can be found in the formulas used to calculate WBAM with each method. With the kinematic method, WBAM is determined independently for each frame of the motion capture data, meaning the values are not dependent on previous ones. In contrast, the impulse method calculates WBAM by integrating the torque caused by external forces about the total body COM. This integration process means that the WBAM is viewed as the cumulative effect of the torque applied over a period of time. Consequently, the values are dependent

on previous values, and any errors in the data will accumulate, amplifying their effect on the final WBAM calculation.

To fully understand the potential magnitude of this effect, one can consider a scenario where an individual stands upright and stationary on a force plate. In this stance, the average torque caused by external forces about the body COM should theoretically be zero, as no angular momentum about the COM is generated. This implies that the GRF should be directed from the COP towards the individual's COM. However, if the total body COM is inaccurately estimated the GRF will not align correctly with the COM, resulting in a constant torque about the COM. When this torque is integrated over time to calculate change in WBAM, the resulting value will begin to drift, either in positive or negative direction depending on the COM estimation error, even when no actual angular momentum is generated. The longer the time considered, the greater the apparent change in WBAM. This effect can also take place due to errors in COP or GRF data. In contrast, using the kinematic method, the WBAM value will remain at zero as long as the individual maintains a stationary position, regardless of the duration of the observation.

This drift effect, resulting from incorrect COM, COP or GRF estimation, is illustrated in figure 22. This buildup is especially noticeable when a person stands still without actively generating any WBAM. However, the same principle also applies in scenarios where actual WBAM is being produced and the GRFs do not align with the COM. In such cases, any errors in COM, GRF, or COP data can lead to either a reduction or an increase in observed WBAM compared to actual values.

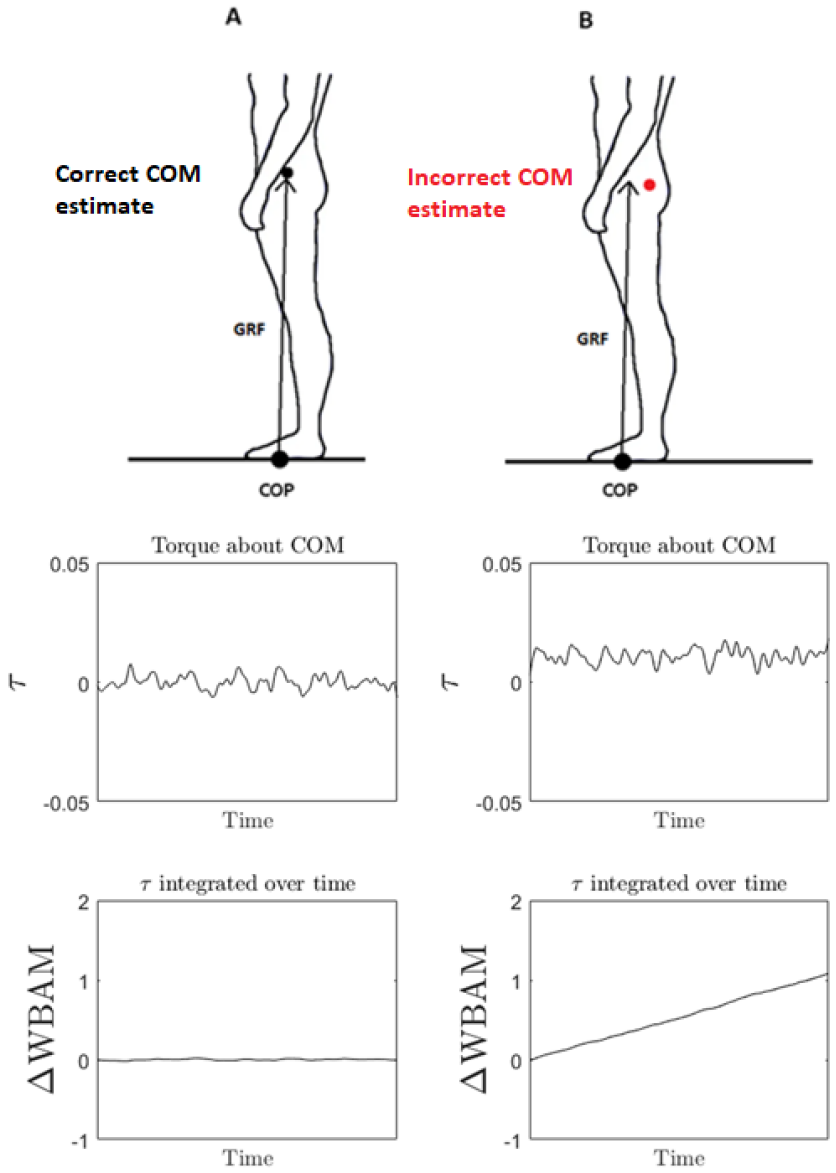

FIGURE 22. A) When COM, COP and GRF estimates are accurate, the average torque over a period of time is zero if no angular momentum is generated. Consequently, integrating this torque results in zero change in WBAM over this time period. B) Inaccuracies in COM, COP, or GRF estimates lead to a small but constant positive torque over a time period. Integrating this torque causes the change in WBAM to accumulate over time. Data and units in the figure are arbitrary, and a small amount of noise is added to the torque data to simulate postural sway.

Taking this drift effect into account, it is easy to understand how errors in COM estimates can lead to accumulating errors in WBAM values when using the impulse method. In the case of subject 2, the COM estimates derived from the LEV model were generally more anterior during the early phases of the trials compared to those from the DEM and DUM models (as shown in figure 11). This anterior shift explains why the WBAM values for the LEV model tended to

drift towards more negative values for subject 2 with the impulse method, particularly during these early phases of the trials. For subject 1, the LEV model also produced more anterior COM estimates during the early phases, but this effect was present for a much shorter duration compared to subject 2 (figure 11). Also, the longer duration of subject 2's trials allowed for any errors in COM estimations to accumulate, amplifying their impact on the final WBAM values.

There were also clear differences in vertical COM estimates between the BSIP models. However, these differences did not contribute as significantly to the observed differences in WBAM values with the impulse method in this study. In the trials performed, the horizontal GRFs were relatively small, and since the vertical COM estimate acts as the lever arm for horizontal GRF components, it had a reduced impact on the total torque about the COM.

In theory, while errors in COP and GRF data are also possible, such errors would have had a consistent effect on torque across all BSIP models and would influence them similarly. Therefore, any differences between impulse-derived WBAM values across the BSIP models can be attributed to differences in COM estimates rather than systematic errors in COP or GRF data. However, it is important to note that any errors in COP and GRF data might have contributed to the observed differences between the impulse and kinematic-derived WBAM values, as these errors would have affected only the impulse-derived values. Additionally, the possible effects of soft tissue artifacts, errors in marker placements or any other errors in the motion capture system cannot be neglected as possible sources of error in both impulse and kinematic-derived values.

While differences in COM estimates between the BSIP models can be attributed to the variations in the models themselves, the methods used for joint center estimations likely played a significant role in these differences. The determination of accurate joint centers is important to reliably calculate the endpoints of body segments, which in turn influences the COM positions of the segments and therefore also the total body COM position. While the total body COM position has influence on both the kinematic and impulse calculations, it can be considered to have more effect on the impulse method as this method relies solely on the total body COM position together with COP and GRFs

Determining the precise location of joint center, especially for ball joints like the hip joint center, is challenging. This complexity is due to the anatomical variability among individuals.

Many methods have been proposed to determine the hip joint centers (Bakke et al. 2023; Bell et al. 1989; Cappozzo 1991; Ehrig et al. 2006; Kainz et al. 2015), and significant differences in the outcomes of kinetic and kinematic analyses have been documented when different estimation techniques are used (Sinclair et al. 2014; Stagni et al. 2000). Medical imaging techniques can be used to accurately determine the joint centers, but they are not generally available or practical in research settings.

Anatomical landmark-based regression equations as provided in Dumas and Wojtusch (2018) were used to determine joint centers in this study (appendix 3) and same joint center positions were used between all three BSIP models to maintain consistency between these definitions. However, the International Society of Biomechanics (ISB) recommends using functional methods, instead of regression equations, to determine the hip joint center whenever feasible (Wu et al. 2002) and adapting to these recommendations could have provided different results with the impulse method WBAM values.

The regression equations were used to determine the inferior endpoints for both the LEV model's trunk segments and the DUM model's pelvis segments (appendix 3). In the DEM model, however, the inferior endpoint of the trunk segment was defined by the midpoint between the trochanter landmarks. Errors in the hip joint center estimates would most significantly affect the total body COM in the LEV model, where the trunk segments represent 43.46 % of the total body mass (table 2). For the DUM model, which segments the trunk into three parts, errors in hip joint center estimates would impact only the pelvis segment which accounts for only 14.2 % of the total body mass. Furthermore, any inaccuracies in hip join center estimates would also affect the COM estimates of the thigh segments, thereby compounding the overall error in the total body COM, as the hip join centers serve as the superior endpoints for the thigh segments both in the LEV and DUM models (appendix 3). In the DEM model, this misestimation would not influence the thigh segments, as their superior endpoints were determined by the trochanter landmarks, not the hip joint centers.

Although the results alone cannot determine the accuracy of the regression equations provided by Dumas and Wojtusch (2018) in estimating subject specific hop join center positions, they do suggest potential variability between the subjects. It is possible that the predictions for subject 1 were closer to the actual anatomical positions than those for subject 2. This variability could explain why the LEV model, when applied with the impulse method, produced outlier

WBAM values for subject 2, as any errors in these joint center predictions would have the greatest impact on this BSIP model.

Some studies have addressed the issue of misalignment of the total body COM relative to the COP by subtracting COP and COM offset in the anterior-posterior direction during a static phase of the trial, where these two should align (Ettema et al. 2020), to enhance the accuracy of WBAM calculations when using the impulse method. Also, different optimization methods can be used to improve the accuracy of BSIP estimates (Chen et al. 2011; Fritz et al. 2019) and therefore to improve COM estimates. However, in this study the comparisons were made without any additional corrections or optimizations.

During the trials performed in this study, the vertical components of the GRFs were the primary factors influencing the impulse method WBAM calculations. However, in trials where horizontal components are more pronounced, errors in the COM estimates in the vertical direction could play a greater role, potentially leading to significantly different results than the ones obtained in this study. Exploring how the two methods compare under such conditions could provide valuable insights into their applicability for analysing dynamic movements with significant horizontal forces.

Virmavirta and Isolehto (2014) reported that on average, the DEM model produces higher total body COM estimates in the longitudinal direction compared to the LEV model, with mean values of 57.03±0.79 % for DEM and 56.20±0.76 % for LEV in male subjects. A similar trend was observed in this study between these two BSIP models (figure 11). While it is impossible to determine which of the COM estimates in this study was closest to the true COM positions of the subjects, the differences in vertical COM estimates did have some, though limited, impact on the overall impulse method WBAM values due to non-zero horizontal GRFs throughout the trials. Findings by Virmavirta and Isolehto (2014) indicate that for gymnasts, the DEM model produces COM estimates in supine position that are close to those obtained using a high accuracy reaction board. While the longitudinal COM estimation by the DEM model may be more accurate for gymnasts in a supine position, this accuracy in one specific pose does not confirm the accuracy of the model in other body configurations, as noted by Virmavirta and Isolehto (2014). Therefore, the longitudinal COM estimates of the DEM model cannot be regarded as more reliable than those of the other BSIP models used in this study, despite the participants being gymnasts.

These variations in longitudinal and anterior-posterior COM estimations among the BSIP models emphasize the need to carefully select an appropriate BSIP model tailored to the characteristics of the participants. Also, attention should be given to the methodology used for estimating joint centers, particularly when the impulse method is used.

Considerations on modelling the trunk. Out of the three BSIP models used in this study, the DUM model provided the most comparable values between the kinematic and impulse methods. In this model, the trunk is segmented into three parts, and COMs of the segments are not assumed to lie solely on the longitudinal axes of the segments. This multi-segment approach to the trunk, as opposed to modelling it as a single segment, might have contributed to the closer agreement of the values. It has been demonstrated that modelling the trunk as a single segment might be an oversimplification (Kudo et al. 2020) that fails to account for the natural movements of the trunk. Given that the trunk represents the largest single segment in BSIP models, oversimplifying this body part can significantly influence the differences observed in the LEV and DEM models between the kinematic and impulse calculations.

8.2 Limitations of the study

There are multiple limitations to this study. Firstly, due to the small number of participants, the findings cannot be generalized, although they do offer some insights into the differences between the two WBAM calculation methods. It is uncertain what kind of WBAM differences would have been observed if the subject specific BSIP values had been used. It also remains unclear how accurate the three regression equation-based BSIP models used in this study represented the actual BSIPs of the subjects.

Another limitation in this study is the regression equations used to define the joint centers, particularly the hip joint centers. Using functional methods to estimate the hip joint centers could provide more accurate estimates, which may change the outcomes of the impulse method. Additionally, the accuracy of marker placements during the trials might have been affected by the lack of experience in palpating and placing reflective markers on anatomical landmarks, potentially introducing errors in the trajectory data and influencing the study's findings.

The use of customized definition for the onset of the trials may have introduced small errors into the data. Specifically, the initial angular momentum values for the impulse method were defined as the average angular momentum values at the trial onset across the three BSIP models, which were derived using the kinematic method. This caused a slight offset between the impulse and kinematic values at the start of the trials. The magnitudes of these differences were relatively small (less than 0.2 kgm^1s^{-1} for all trials), so they most likely did not significantly impact the overall results.

The application of DEM and LEV BSIP models in 3D motion capture presents certain challenges, as the endpoints and axes of the segments are not always directly defined or directly applicable to these analyses. Certain assumptions had to be made in defining some of these segments, which could have introduced some errors to the results. All assumptions and definitions used in this study are documented in the appendices, allowing readers to assess the appropriateness of the choices made for this study. It is worth noting that sometimes authors can be rather vague about how they apply these models in their analyses, and this is why this study aimed to be as transparent as possible with the applications of these BSIP models.

9 CONCLUSION

Based on the results of this study, significant methodological differences can be seen in whole body angular momentum values depending on the choice of calculation method and body segment inertial parameter model. By comparing Dempter (1955), de Leva (1996) and Dumas and Wojtusch (2018) body segment inertial parameter models, Dumas and Wojtusch (2018) model seemed to produce the most consistent results between the kinematic and the impulse methods. It was noted that the choice of calculation method had more effect on the differences in whole body angular momentum values than the choice of body segment inertial parameter model.

Overall, the kinematic method produced more consistent results than the impulse method, regardless of the chosen body segment inertial parameter model. Based on these findings, the kinematic method could be recommended as the preferred approach for determining whole body angular momentum in biomechanical studies to ensure better comparability between the findings. However, it remains unknown how these two calculation methods would compare if an individualised body segment inertial parameter model were used, rather than the regression equation-based models used in this study.

In the trials conducted in this study, the assumption that motion occurred parallel to the sagittal plane and that the medio-lateral axes of the segments were the principal axes of rotation did not result in significant differences in the obtained whole body angular momentum values. This finding supports the use of these assumptions to simplify the calculation of whole body angular momentum and suggests that they can be reliably applied in future biomechanical analyses for similar types of trials.

REFERENCES

Ackland, T. R., Blanksby, B. A. & Bloomfield, J. (1988). Inertial characteristics of adolescent male body segments. Journal of Biomechanics, 21(4), pp. 319–327. https://doi.org/10.1016/0021-9290(88)90261-8

Adler, R. J. & Taylor, E. J. (2007). Random Fields and Geometry. New York, NY: Springer. https://doi.org/10.1007/978-0-387-48116-6

Andrews, J. G. & Mish, S. P. (1996). Methods for investigating the sensitivity of joint resultants to body segment parameter variations. Journal of Biomechanics, 29(5), pp. 651–654. https://doi.org/10.1016/0021-9290(95)00118-2

Baca, A. (1996). Precise determination of anthropometric dimensions by means of image processing methods for estimating human body segment parameter values. Journal of Biomechanics, 29(4), pp. 563–567. https://doi.org/10.1016/0021-9290(95)00033-X

Bakke, D., Zhang, J., Hislop-Jambrich, J. & Besier, T. (2023). Hip centre regression progression: Same equations, better numbers. Journal of Biomechanics, 147, 111418. https://doi.org/10.1016/j.jbiomech.2022.111418

Bauer, J. J., Pavol, M. J., Snow, C. M. & Hayes, W. C. (2007). MRI-derived body segment parameters of children differ from age-based estimates derived using photogrammetry. Journal of Biomechanics, 40(13), pp. 2904–2910. https://doi.org/10.1016/j.jbiomech.2007.03.006

Begue, J., Peyrot, N., Lesport, A., Turpin, N. A., Watier, B., Dalleau, G. & Caderby, T. (2021). Segmental contribution to whole-body angular momentum during stepping in healthy young and old adults. Scientific Reports, 11(1). https://doi.org/10.1038/s41598-021-99519-y

Bell, A. L., Brand, R. A. & Pedersen, D. R. (1989). Prediction of hip joint centre location from external landmarks. Human Movement Science, 8(1), pp. 3–16. https://doi.org/10.1016/0167-9457(89)90020-1

Bennett, B. C., Russell, S. D., Sheth, P. & Abel, M. F. (2010). Angular momentum of walking at different speeds. Human Movement Science, 29(1), pp. 114–124. https://doi.org/10.1016/j.humov.2009.07.011

Browning, R. C. (2012). Locomotion Mechanics in Obese Adults and Children. Current Obesity Reports, 1(3), pp. 152–159. https://doi.org/10.1007/s13679-012-0021-z

Camomilla, V., Cereatti, A., Cutti, A. G., Fantozzi, S., Stagni, R. & Vannozzi, G. (2017). Methodological factors affecting joint moments estimation in clinical gait analysis: A systematic review. Biomedical Engineering Online, 16(1), 106. https://doi.org/10.1186/s12938-017-0396-x

Cappozzo, A. (1991). Three-dimensional analysis of human walking: Experimental methods and associated artifacts. Human Movement Science, 10(5), pp. 589–602. https://doi.org/10.1016/0167-9457(91)90047-2

Cappozzo. A., Catani, F., Groce, U. D. & Leardini, A. (1995). Position and orientation in space of bones during movement: anatomical frame definition and determination. Clinical Biomechanics, 10(4), pp. 171–178. https://doi.org/10.1016/0268-0033(95)91394-T

Cappozzo, A., Catani, F., Leardini, A., Benedetti, M. G. & Croce, U. D. (1996). Position and orientation in space of bones during movement: Experimental artefacts. Clinical Biomechanics, 11(2), pp. 90–100. https://doi.org/10.1016/0268-0033(95)00046-1

Chambers, A. J., Sukits, A. L., McCrory, J. L. & Cham, R. (2010). The effect of obesity and gender on body segment parameters in older adults. Clinical Biomechanics 25(2), 131. https://doi.org/10.1016/j.clinbiomech.2009.10.015

Chandler, R., Clauser, C., McConville, J., Reynolds, H. & Young, J. (1975). Investigation of Inertial Properties of the Human Body. AMRL Technical Report No. 74-137, Wright Patterson Air Force Base, OH.

Chen, S.-C., Hsieh, H.-J., Lu, T.-W. & Tseng, C.-H. (2011). A method for estimating subject-specific body segment inertial parameters in human movement analysis. Gait & Posture, 33(4), pp. 695–700. https://doi.org/10.1016/j.gaitpost.2011.03.004

Cheng, C. K., Chen, H. H., Chen, C. S., Chen, C. L. & Chen, C. Y. (2000). Segment inertial properties of Chinese adults determined from magnetic resonance imaging. Clinical Biomechanics (Bristol, Avon), 15(8), pp. 559–566. https://doi.org/10.1016/s0268-0033(00)00016-4

Chockalingam, N., Giakas, G. & Iossifidou, A. (2002). Do strain gauge force platforms need in situ correction? Gait & Posture, 16(3), pp. 233–237. https://doi.org/10.1016/S0966-6362(02)00017-6

Cicchella, A. (2020). Development of the Biomechanical Technologies for the Modeling of Major Segments of the Human Body: Linking the Past with the Present. Biology, 9, 399. https://doi.org/10.3390/biology9110399

Clauser, C. E., McConville, J. T. & Young, J. W. (1969). Weight, Volume and Center of Mass of Segments of the Human Body. AMRL Technical Report No. 69-70, Wright-Patterson Air Force Base, OH.

Conceição, F., Lewis, M., Lopes, H. & Fonseca, E. M. M. (2022). An Evaluation of the Accuracy and Precision of Jump Height Measurements Using Different Technologies and Analytical Methods. Applied Sciences, 12(1). https://doi.org/10.3390/app12010511

Costa Moreira, O., Patrocínio DE Oliveira, C. E., DE Matos, D. G., Mazini Filho, M. L., Fernandes DA Silva, S., Aidar, F. J. & DE Paz, J. A. (2021). The comparative measurement of body segment parameters using dual energy X-ray absorptiometry between sexes. The Journal of Sports Medicine and Physical Fitness, 61(12), pp. 1613–1619. https://doi.org/10.23736/S0022-4707.20.11978-9

Dapena, J. (1978). A method to determine the angular momentum of a human body about three orthogonal axes passing through its center of gravity. Journal of Biomechanics, 11(5), pp. 251–256. https://doi.org/10.1016/0021-9290(78)90051-9

de Leva, P. (1996). Adjustments to Zatsiorsky-Seluyanov's segment inertia parameters. Journal of Biomechanics, 29(9), pp. 1223–1230. https://doi.org/10.1016/0021-9290(95)00178-6

Dempster, W. T. (1955). Space requirements of the seated operator: Geometrical, kinematic, and mechanical aspects of the body, with special reference to the limbs. WADC Technical Report 55-159, Wright-Patterson Air Force Base, Ohio. Carpenter Litho & Printing Co., Springfield, Ohio.

Doane, J. E. & Quesada P. M. (2009). A new method for estimating subject specific body segment parameters using motion tracking data. Theoretical Issues in Ergonomics Science, 10(1), pp. 69–76. https://doi.org/10.1080/14639220701656716

Drillis, R., Contini, R. & Bluestein, M. (1964). Body segment parameters: a survey of measurement tehniques. Artificial Limbs, 8, pp. 44–66.

Dumas, R., Aissaoui, R., Mitton, D., Skalli, W. & de Guise, J. A. (2005). Personalized body segment parameters from biplanar low-dose radiography. IEEE Transactions on Bio-Medical Engineering, 52(10), pp. 1756–1763. https://doi.org/10.1109/TBME.2005.855711

Dumas, R., Chèze, L. & Verriest, J.-P. (2007). Adjustments to McConville et al. And Young et al. Body segment inertial parameters. Journal of Biomechanics, 40(3), pp. 543–553. https://doi.org/10.1016/j.jbiomech.2006.02.013

Dumas, R. & Wojtusch, J. (2018). Estimation of the Body Segment Inertial Parameters for the Rigid Body Biomechanical Models Used in Motion Analysis. In Müller, B., Wolf, S. I., Brueggemann, G.-P., Deng, Z., McIntosh, A., Miller, F. & Selbie, W. S. (Eds.) Handbook of Human Motion. Cham, Switzerland: Springer International Publishing, pp. 47–77.

Durkin, J. L. (2008). Measurement and estimation of human body segment parameters. In Hong, Y. & Bartlett, R. (Eds.) Handbook of Biomechanics and Human Movement Science. Routledge, Oxford, UK, pp. 197–213.

Durkin, J. L. & Dowling, J. J. (2003). Analysis of body segment parameter differences between four human populations and the estimation errors of four popular mathematical models. Journal of Biomechanical Engineering, 125(4), pp. 515–522. https://doi.org/10.1115/1.1590359

Durkin, J. L. & Dowling, J. J. (2006). Body segment parameter estimation of the human lower leg using an elliptical model with validation from DEXA. Annals of Biomedical Engineering, 34, pp. 1483–1493. https://doi.org/10.1007/s10439-006-9088-6

Durkin, J. L., Dowling, J. J. & Andrews, D. M. (2002). The measurement of body segment inertial parameters using dual energy X-ray absorptiometry. Journal of Biomechanics, 35(12), pp. 1575–1580. https://doi.org/10.1016/s0021-9290(02)00227-0

Ehrig, R. M., Taylor, W. R., Duda, G. N. & Heller, M. O. (2006). A survey of formal methods for determining the centre of rotation of ball joints. Journal of Biomechanics, 39(15), pp. 2798–2809. https://doi.org/10.1016/j.jbiomech.2005.10.002

Erdmann, W. S. (1997). Geometric and inertial data of the trunk in adult males. Journal of Biomechanics, 30(7), pp. 679–688. https://doi.org/10.1016/S0021-9290(97)00013-4

Ettema, G., Braaten, S., Danielsen, J. & Fjeld, B. E. (2020). Imitation jumps in ski jumping: Technical execution and relationship to performance level. Journal of Sports Sciences, 38(18), pp. 2155–2160. https://doi.org/10.1080/02640414.2020.1776913

Friston, K. J., Holmes, A. P., Worsley, K. J., Poline, J.-P., Frith, C. D. & Frackowiak, R. S. J. (1994). Statistical parametric maps in functional imaging: A general linear approach. Human Brain Mapping, 2(4), pp. 189–210. https://doi.org/10.1002/hbm.460020402

Fritz, J., Kröll, J. & Schwameder, H. (2019). Influence of body segment parameter estimation on calculated ground reaction forces in highly dynamic movements. Journal of Biomechanics, 84, pp. 11–17. https://doi.org/10.1016/j.jbiomech.2018.12.008

Ganley, K. J. & Powers, C. M. (2004). Determination of lower extremity anthropometric parameters using dual energy X-ray absorptiometry: The influence on net joint moments during gait. Clinical Biomechanics, 19(1), pp. 50–56. https://doi.org/10.1016/j.clinbiomech.2003.08.002

Gervais, P. & Dunn, J. (2003). Gymnastics: The double back salto dismount from the parallel bars. Sports Biomechanics, 2(1), pp. 85–101. https://doi.org/10.1080/14763140308522810

Hamill, J., Ricard, M. D. & Golden, D. M. (1986). Angular Momentum in Multiple Rotation Nontwisting Platform Dives. International Journal of Sport Biomechanics, 2(2), pp. 78–87. https://doi.org/10.1123/ijsb.2.2.78

Hanavan, E. P. (1964). A Mathematical Model of the Human Body. AMRL Technical Report-No. 64-102, Wright-Patterson Air Force Base, OH.

Hansen, C., Venture, G., Rezzoug, N., Gorce, P. & Isableu, B. (2014). An individual and dynamic Body Segment Inertial Parameter validation method using ground reaction forces. Journal of Biomechanics, 47(7), pp. 1577–1581. https://doi.org/10.1016/j.jbiomech.2014.03.004

Hatze, H. (1980). A mathematical model for the computational determination of parameter values of anthropomorphic segments. Journal of Biomechanics, 13(10), pp. 833–843. https://doi.org/10.1016/0021-9290(80)90171-2

Herr, H. & Popovic, M. (2008). Angular momentum in human walking. Journal of Experimental Biology, 211(4), pp. 467–481. https://doi.org/10.1242/jeb.008573

Hiley, M. J., Jackson, M. I. & Yeadon, M. R. (2015). Optimal technique for maximal forward rotating vaults in men's gymnastics. Human Movement Science, 42, pp. 117–131. https://doi.org/10.1016/j.humov.2015.05.006

Hiley, M. J. & Yeadon, M. R. (2003). Optimum Technique for Generating Angular Momentum in Accelerated Backward Giant Circles Prior to a Dismount. Journal of Applied Biomechanics, 19(2), pp. 119–130. https://doi.org/10.1123/jab.19.2.119

Hiley, M. J. & Yeadon, M. R. (2005). Maximal dismounts from high bar. Journal of Biomechanics, 38(11), pp. 2221–2227. https://doi.org/10.1016/j.jbiomech.2004.09.025

Ho, W.-H., Shiang, T.-Y., Lee, C.-C. & Cheng, S.-Y. (2013). Body Segment Parameters of Young Chinese Men Determined with Magnetic Resonance Imaging. Medicine & Science in Sports & Exercise, 45(9), pp. 1759–1766. https://doi.org/10.1249/MSS.0b013e3182923b2a

Hraski, Ž., Mejovsek, M. (2004). Production of angular momentum for backward somersault. IASTED International Conference on Biomechanics, Honolulu, Hawaii, USA.

Hwang, I., Seo, G. & Liu, Z. C. (1990). Takeoff Mechanics of the Double Backward Somersault. Journal of Applied Biomechanics, 6(2), pp. 177–186. https://doi.org/10.1123/ijsb.6.2.177

Irwin, G., Manning, M. & Kerwin, D. G. (2011). Kinematics and angular momentum contributions to the toe-on Tkachev on uneven bars in female gymnastics. ISBS - Conference Proceedings Archive. https://ojs.ub.uni-konstanz.de/cpa/article/view/4825

Jagadale, M., Agrawal, K. N., Mehta, C. R., Potdar, R. R. & Thakur, N. (2022). Estimation and Validation of Body Segment Parameters Using 3D Geometric Model of Human Body for Female Workers of Central India. Agricultural Research, 11(4), pp. 768–780. https://doi.org/10.1007/s40003-021-00608-1

Jensen, R. K. (1978). Estimation of the biomechanical properties of three body types using a photogrammetric method. Journal of Biomechanics, 11(8), pp. 349–358. https://doi.org/10.1016/0021-9290(78)90069-6

Kainz, H., Carty, C. P., Modenese, L., Boyd, R. N. & Lloyd, D. G. (2015). Estimation of the hip joint centre in human motion analysis: A systematic review. Clinical Biomechanics, 30(4), pp. 319–329. https://doi.org/10.1016/j.clinbiomech.2015.02.005

Kerwin, D. G., Webb, J. & Yeadon, F. R. (1998). Production of angular momentum in double somersaults. ISBS - Conference Proceedings Archive. https://ojs.ub.uni-konstanz.de/cpa/article/view/1618

Kim, D., Lewis, C. L. & Gill, S. V. (2022). The effect of obesity on whole-body angular momentum during steady-state walking. Gait & Posture, 94, pp. 93–101. https://doi.org/10.1016/j.gaitpost.2022.02.029

King, M. A. & Yeadon, M. R. (2004). Maximising somersault rotation in tumbling. Journal of Biomechanics, 37(4), pp. 471–477. https://doi.org/10.1016/j.jbiomech.2003.09.008

Köhler, H.-P., Schüler, A., Quaas, F., Fiedler, H., Witt, M. & Roemer, K. (2024). The influence of body segment estimation methods on body segment inertia parameters and joint moments in javelin throwing. Computer Methods in Biomechanics and Biomedical Engineering, 27(3), pp. 267–275. https://doi.org/10.1080/10255842.2023.2181039

Król, H., Klyszcz-Morciniec, M. & Bacik, B. (2020). The Structure of Selected Basic Acrobatic Jumps. Journal of Human Kinetics, 75, pp. 41–64. https://doi.org/10.2478/hukin-2020-0036

Król, H., Klyszcz-Morciniec, M., Sobota, G. & Nowak, K. (2016). The Complex Analysis of Movement in the Evaluation of the Backward Somersault Performance. Physical Activity Review, 4, pp. 28–39. https://doi.org/10.16926/par.2016.04.04

Kudo, S., Fujimoto, M., Sato, T. & Nagano, A. (2020). Determination of the optimal number of linked rigid-bodies of the trunk during walking and running based on Akaike's information criterion. Gait & Posture, 77, pp. 264–268. https://doi.org/10.1016/j.gaitpost.2020.02.009

Kudzia, P., Jackson, E. & Dumas, G. (2022). Estimating body segment parameters from three-dimensional human body scans. PLoS ONE, 17(1), e0262296. https://doi.org/10.1371/journal.pone.0262296

Kwon, Y.-H. (1996). Effects of the Method of Body Segment Parameter Estimation on Airborne Angular Momentum. Journal of Applied Biomechanics, 12(4), pp. 413–430. https://doi.org/10.1123/jab.12.4.413

Laschowski, B. & McPhee, J. (2016). Body segment parameters of Paralympic athletes from dual-energy X-ray absorptiometry. Sports Engineering, 19(3), pp. 155–162. https://doi.org/10.1007/s12283-016-0200-3

Lu, J.-M. & Wang, M.-J. J. (2008). Automated anthropometric data collection using 3D whole body scanners. Expert Systems with Applications, 35(1), pp. 407–414. https://doi.org/10.1016/j.eswa.2007.07.008

Mathiyakom, W., McNitt-Gray, J. L. & Wilcox, R. R. (2007). Regulation of angular impulse during two forward translating tasks. Journal of Applied Biomechanics, 23(2), pp. 149–161. https://doi.org/10.1123/jab.23.2.149

Mathiyakom, W., Wilcox, R. & McNitt-Gray, J. L. (2021). Regulation of Forward Angular Impulse in Tasks with Backward Translation. Journal of Applied Biomechanics, 37(6), pp. 601–610. https://doi.org/10.1123/jab.2021-0301

Mathiyakom, W., Wilcox, R. & McNitt-Gray, J. L. (2023). Generation of forward angular impulse with different initial conditions. Human Movement Science, 87, 103035. https://doi.org/10.1016/j.humov.2022.103035

McConville, J. T., Clauser, C. E., Churchill, T. D., Cuzzi, J. & Kaleps, I. (1980,). Anthropometric Relationships of Body and Body Segment Moments of Inertia. Technical Report AFAMRL-TR-80-119, Aerospace Medical Research Laboratory, Wright–Patterson Air Force Base, Dayton, Ohio. https://doi.org/10.21236/ADA097238

McNitt-Gray, J. L. (2018). 2016 American Society of Biomechanics Hay Award Lecture: Preparing for Impact—Biomechanical Inspirations From Olympic Sports. Journal of Applied Biomechanics, 34(4), pp. 249–257. https://doi.org/10.1123/jab.2017-0270

Merrill, Z., Perera, S., Chambers, A. & Cham, R. (2019). Age and body mass index associations with body segment parameters. Journal of Biomechanics, 88, pp. 38–47. https://doi.org/10.1016/j.jbiomech.2019.03.016

Miller, D. I., Hennig, E., Pizzimenti, M. A., Jones, I. C. & Nelson, R. C. (1989). Kinetic and Kinematic Characteristics of 10-m Platform Performances of Elite Divers: I. Back Takeoffs. Journal of Applied Biomechanics, 5(1), pp. 60–88. https://doi.org/10.1123/ijsb.5.1.60

Miller, D. I. & Munro, C. F. (1985). Greg Louganis' Springboard Takeoff: II. Linear and Angular Momentum Considerations. Journal of Applied Biomechanics, 1(4), pp. 288–307. https://doi.org/10.1123/ijsb.1.4.288

Mungiole, M. & Martin, P. E. (1990). Estimating segment inertial properties: Comparison of magnetic resonance imaging with existing methods. Journal of Biomechanics, 20(10), pp. 1039–1046. https://doi.org/10.1016/0021-9290(90)90319-X

Müller, W. (2006). The physics of ski jumping. Proceedings of European School of High-energy Physics, pp. 269–278.

Nagymáté, G. & Kiss, R. M. (2018). Motion capture system validation with surveying techniques. Materials Today: Proceedings, 5(13, part 2), pp. 26501–26506. https://doi.org/10.1016/j.matpr.2018.08.107

Negishi, T. & Ogihara, N. (2023a). Functional significance of vertical free moment for generation of human bipedal walking. Scientific Reports, 13. https://doi.org/10.1038/s41598-023-34153-4

Negishi, T. & Ogihara, N. (2023b). Regulation of whole-body angular momentum during human walking. Scientific Reports, 13. https://doi.org/10.1038/s41598-023-34910-5

Nikolova, G. S. & Dantchev, D. M. (2020). 3D mathematical model of the human body: Analytical results. AIP Conference Proceedings. https://doi.org/10.1063/5.0033607

Norton, J., Donaldson, N. & Dekker, L. (2002). 3D whole body scanning to determine mass properties of legs. Journal of Biomechanics, 35(1), pp. 81–86. https://doi.org/10.1016/S0021-9290(01)00161-0

Osis, S., Hettinga, B., Macdonald, S. & Ferber, R. (2016). Effects of Simulated Marker Placement Deviations on Running Kinematics and Evaluation of a Morphometric-Based Placement Feedback Method. PLoS ONE, 11(1). https://doi.org/10.1371/journal.pone.0147111

Pandis, P. & Bull, A. M. (2017). A low-cost three-dimensional laser surface scanning approach for defining body segment parameters. Proceedings of the Institution of Mechanical Engineers, Part H: Journal of Engineering in Medicine, 231(11), pp. 1064–1068. https://doi.org/10.1177/0954411917727031

Pearsall, D. J. & Costigan, P. A. (1999). The effect of segment parameter error on gait analysis results. Gait & Posture, 9(3), pp. 173–183. https://doi.org/10.1016/S0966-6362(99)00011-9

Pearsall, D. J. & Reid, J. G. (1994). The study of human body segment parameters in biomechanics. An historical review and current status report. Sports Medicine, 18(2), pp. 126–140. https://doi.org/10.2165/00007256-199418020-00005

Pearsall, D. J., Reid, J. G. & Livingston, L. A. (1996). Segmental inertial parameters of the human trunk as determined from computed tomography. Annals of Biomedical Engineering, 24(2), pp. 198–210. https://doi.org/10.1007/BF02667349

Peyer, K. E., Morris, M. & Sellers, W. I. (2015). Subject-specific body segment parameter estimation using 3D photogrammetry with multiple cameras. PeerJ, 3, e831. https://doi.org/10.7717/peerj.831

Pijnappels, M., Bobbert, M. F. & Dieën, J. H. van. (2005). Push-off reactions in recovery after tripping discriminate young subjects, older non-fallers and older fallers. Gait & Posture, 21(4), pp. 388–394. https://doi.org/10.1016/j.gaitpost.2004.04.009

Pijnappels, M., van der Burg, (Petra) J. C. E., Reeves, N. D. & van Dieën, J. H. (2008). Identification of elderly fallers by muscle strength measures. European Journal of Applied Physiology, 102(5), pp. 585–592. https://doi.org/10.1007/s00421-007-0613-6

Rao, G., Amarantini, D., Berton, E. & Favier, D. (2006). Influence of body segments' parameters estimation models on inverse dynamics solutions during gait. Journal of Biomechanics, 39(8), pp. 1531–1536. https://doi.org/10.1016/j.jbiomech.2005.04.014

Redfern, M. S., Cham, R., Gielo-Perczak, K., Grönqvist, R., Hirvonen, M., Lanshammar, H., Marpet, M., Pai IV, C. Y.-C. & Powers, C. (2001). Biomechanics of slips. Ergonomics, 44(13), pp. 1138–1166. https://doi.org/10.1080/00140130110085547

Reid, J. G. (1984). Physical properties of the human trunk as determined by computed tomography. Archives of Physical Medicine and Rehabilitation, 65(5), pp. 246–250.

Robertson, D. G. E., Caldwell, G. E., Hamill, J., Kamen, G. & Whittlesey, S. N. (2014). Research methods in biomechanics. 2nd edition. Champaign, IL: Human Kinetics.

Robertson, W. (2013). A modern take on the theoretical modelling of inertial properties of a human body for biomechanical simulations. In Piantadosi, J., Anderssen, R.S. and Boland J. (Eds.) MODSIM2013, 20th International Congress on Modelling and Simulation. Modelling and Simulation Society of Australia and New Zealand, December 2013. ISBN: 978-0-9872143-3-1. https://doi.org/10.36334/modsim.2013.C4.robertson

Rossi, M., Lyttle, A., El-Sallam, A., Benjanuvatra, N. & Blanksby, B. (2013). Body segment inertial parameters of elite swimmers using DXA and indirect methods. Journal of Sports Science and Medicine, 12(4), pp. 761–775. Scopus.

Sanders, R. H., Chiu, C.-Y., Gonjo, T., Thow, J., Oliveira, N., Psycharakis, S. G., Payton, C. J. & McCabe, C. B. (2015). Reliability of the Elliptical Zone Method of Estimating Body Segment Parameters of Swimmers. Journal of Sports Science & Medicine, 14(1), pp. 215–224.

Sanders, R. & Wilson, B. (1988). Angular Momentum Requirements of the Twisting and Nontwisting Forward 1 1/2 Somersault Dive. International Journal of Sport Biomechanics, 3, pp. 47–62. https://doi.org/10.1123/ijsb.3.1.47

Schmiedmayer, H. B. & Kastner, J. (1999). Parameters influencing the accuracy of the point of force application determined with piezoelectric force plates. Journal of Biomechanics, 32(11), pp. 1237–1242. https://doi.org/10.1016/s0021-9290(99)00109-8

Schueler, A., Fichtner, I. & Ueberschär, O. (2018). Using the 3D Body Scanner in Elite Sports. Proc. of 3DBODY.TECH 2018 - 9th Int. Conf. and Exh. on 3D Body Scanning and Processing Technologies, Lugano, Switzerland, 16-17 Oct. 2018, pp. 216–221. https://doi.org/10.15221/18.216

Schüler, A., Kerner, S. & Witt, M. (2015). A comparison of two body segment parameter models via angular momentum at takeoff in diving. ISBS - Conference Proceedings Archive. https://ojs.ub.uni-konstanz.de/cpa/article/view/6346

Schwameder, H. (2008). Biomechanics research in ski jumping, 1991-2006. Sports Biomechanics, 7(1), pp. 114–136. https://doi.org/10.1080/14763140701687560

Sheets, A. L., Corazza, S. & Andriacchi, T. P. (2009). An Automated Image-Based Method of 3D Subject-Specific Body Segment Parameter Estimation for Kinetic Analyses of Rapid Movements. Journal of Biomechanical Engineering, 132(011004). https://doi.org/10.1115/1.4000155

Silverman, A. K., Wilken, J. M., Sinitski, E. H. & Neptune, R. R. (2012). Whole-body angular momentum in incline and decline walking. Journal of Biomechanics, 45(6), pp. 965–971. https://doi.org/10.1016/j.jbiomech.2012.01.012

Sinclair, J., Atkins, S. & Vincent, H. (2014). Influence of Different Hip Joint Centre Locations on Hip and Knee Joint Kinetics and Kinematics During the Squat. Journal of Human Kinetics, 44, pp. 5–17. https://doi.org/10.2478/hukin-2014-0106

Smith, S. H. L. & Bull, A. M. J. (2018). Rapid calculation of bespoke body segment parameters using 3D infra-red scanning. Medical Engineering & Physics, 62, pp. 36–45. https://doi.org/10.1016/j.medengphy.2018.10.001

Stagni, R., Leardini, A., Cappozzo, A., Grazia Benedetti, M. & Cappello, A. (2000). Effects of hip joint centre mislocation on gait analysis results. Journal of Biomechanics, 33(11), pp. 1479–1487. https://doi.org/10.1016/s0021-9290(00)00093-2

Takei, Y., Dunn, J. H. & Blucker, E. (2003). Gymnastics: Techniques used in high-scoring and low-scoring 'roche' vaults performed by elite male gymnasts. Sports Biomechanics, 2(2), pp. 141–162. https://doi.org/10.1080/14763140308522814

van der Kruk, E. & Reijne, M. M. (2018). Accuracy of human motion capture systems for sport applications; state-of-the-art review. European Journal of Sport Science, 18(6), pp. 806–819. https://doi.org/10.1080/17461391.2018.1463397

Virmavirta, M. (2017). Ski Jumping: Aerodynamics and Kinematics of Take-Off and Flight. In Müller, B., Wolf, S. I., Brueggemann, G.-P., Deng, Z., McIntosh, A., Miller, F. & Selbie, W. S. (Eds.) Handbook of Human Motion. Cham, Switzerland: Springer International Publishing, pp. 1681–1701

Virmavirta, M. & Isolehto, J. (2014). Determining the location of the body′s center of mass for different groups of physically active people. Journal of Biomechanics, 47(8), pp. 1909–1913. https://doi.org/10.1016/j.jbiomech.2014.04.001

Whittaker, R. L., Vidt, M. E., Lockley, R. M. E., Mourtzakis, M. & Dickerson, C. R. (2021). Upper extremity and trunk body segment parameters are affected by BMI and sex. Journal of Biomechanics, 117, 110230. https://doi.org/10.1016/j.jbiomech.2021.110230

Winter, D. A. (2009). Biomechanics and Motor Control of Human Movement. 4th edition. Hoboken, NJ: John Wiley & Sons, Inc.

Winter, S. L., Forrest, S. M., Wallace, J. & Challis, J. H. (2018). A Dual X-Ray Absorptiometry Validated Geometric Model for the Calculation of Body Segment Inertial Parameters of Young Females. Journal of Applied Biomechanics, 34(2), pp. 89–95. https://doi.org/10.1123/jab.2016-0307

Wu, G., Siegler, S., Allard, P., Kirtley, C., Leardini, A., Rosenbaum, D., Whittle, M., D'Lima, D. D., Cristofolini, L., Witte, H., Schmid, O. & Stokes, I. (2002). ISB recommendation on definitions of joint coordinate system of various joints for the reporting of human joint motion—part I: Ankle, hip, and spine. Journal of Biomechanics, 35(4), pp. 543–548. https://doi.org/10.1016/S0021-9290(01)00222-6

Yeadon, M. R. (1990). The simulation of aerial movement—II. A mathematical inertia model of the human body. Journal of Biomechanics, 23(1), pp. 67–74. https://doi.org/10.1016/0021-9290(90)90370-I

Yeadon, M. R. (1993). The biomechanics of twisting somersaults. Part III: Aerial twist. Journal of Sports Sciences, 11(3), pp. 209–218. https://doi.org/10.1080/02640419308729987

Yeadon, M. R. (2017). Airborne Movements: Somersaults and Twists. In Müller, B., Wolf, S. I., Brueggemann, G.-P., Deng, Z., McIntosh, A., Miller, F. & Selbie, W. S. (Eds.) Handbook of Human Motion. Cham, Switzerland: Springer International Publishing, pp. 1661–1680.

Young, J. W., Chandler, R. F., Snow, C. C., Robinette, K. M., Zehner, G. F. & Lofberg, M. S. (1983). Anthropometric and mass distribution characteristics of the adult female. Article FAA-AM-83-16, FAA Civil Aeromedical Institute, Oklahoma City.

Yu, B. & Hay, J. G. (1995). Angular Momentum and Performance in the Triple Jump: A Cross-Sectional Analysis. Journal of Applied Biomechanics, 11(1), pp. 81–102. https://doi.org/10.1123/jab.11.1.81

Zatsiorsky, V. (1998). Kinematics of Human Motion. Champaign, IL: Human Kinetics.

Zatsiorsky, V. (2002). Kinetics of Human Motion. Champaign, IL: Human Kinetics.

Zatsiorsky, V. & Seluyanov, V. (1983). The mass and inertia characteristics of the main segment of human body. In Matsui, H. & Kobayashi K. (Eds.) Biomechanics VIII-B. Champaign, IL: Human Kinetics, pp. 1152–1159.

Zatsiorsky, V. & Seluyanov, V. (1985). Estimation of the mass and inertia characteristics of the human body by means of the best predictive regression equations. Biomechanics IX-B. Champaign, IL: Human Kinetics, pp. 233–239.

Zatsiorsky, V., Seluyanov V. & Chugunova, L. (1990a). Methods of determining mass-inertial characteristics of human body segments. In Chernyi, G.G. & Regirer, S.A. (Eds) Contemporary Problems of Biomechanics. Boston, MA: CRC Press, pp. 272–291.

Zatsiorsky, V., Seluyanov, V. & Chugunova, L. (1990b). In vivo body segment inertial parameters determination using a gamma-scanner method. Biomechanics of human movement: Applications in rehabilitation, sports and ergonomics, pp. 187–202.

APPENDIX 1. Marker names, abbreviations, and anatomical positions

Marker anatomical positions as defined in Dumas et al. (2007).

Marker (abbreviation)	**Marker position**
Head vertex (VERT)	Most cranial point of the head when the head is oriented in the Frankfort plane
Sellion (SEL)	Greatest indentation of the nasal root depression in the mid-sagittal plane
7th cervical vertebra (C7)	Superior tip of the spine of the 7th cervical vertebra
Right acromion (RACRO)	Most lateral point on the lateral edge of the acromial process of scapula
Left acromion (LACRO)	Most lateral point on the lateral edge of the acromial process of scapula
Suprasternale (STERN)	Lowest point in the notch in the upper edge of the breastbone
8th thoracic vertebra (TH8)	Superior tip of the spine of the 8th thoracic vertebra
12th thoracic vertebra (TH12)	Superior tip of the spine of the 12th thoracic vertebra
Right posterior superior iliac spine (RPSIS)	Most prominent point on the posterior superior spine of right ilium
Left posterior superior iliac spine (LPSIS)	Most prominent point on the posterior superior spine of left ilium
Right anterior superior iliac spine (RASIS)	Most prominent point on the anterior superior spine of right ilium
Right anterior left iliac spine (LASIS)	Most prominent point on the anterior superior spine of left ilium
Right greater trochanter (RTROC)	Superior point on the right greater trochanter
Left greater trochanter (LTROC)	Superior point on the left greater trochanter
Right lateral femoral epicondyle (RLATKNEE)	Most lateral point of the lateral epicondyle of right femur
Left lateral femoral epicondyle (LLATKNEE)	Most lateral point of the lateral epicondyle of left femur
Right medial femoral epicondyle (RMEDKNEE)	Most medial point of the medial epicondyle of right femur
Left medial femoral epicondyle (LMEDKNEE)	Most medial point of the medial epicondyle of left femur
Right lateral malleolus (RLATANK)	Most lateral point of the lateral malleolus of right ankle

Left lateral malleolus (RLATANK)	Most lateral point of the lateral malleolus of left ankle
Right medial malleolus (RMEDANK)	Most medial point of the medial malleolus of right ankle
Left medial malleolus (LMEDANK)	Most medial point of the medial malleolus of left ankle
Right heel (RHEEL)	Most posterior point of the right heel
Left heel (LHEEL)	Most posterior point of the left heel
Right 5th metatarsal head (RMET5)	Lateral point of the head of fifth metatarsus on right foot
Left 5th metatarsal head (LMET5)	Lateral point of the head of fifth metatarsus on left foot
Right 1st metatarsal head (RMET1)	Medial point of the head of first metatarsus on right foot
Left 1st metatarsal head (LMET1)	Medial point of the head of first metatarsus on left foot
Right 2nd toe tip (RTOETIP)	Anterior point of the second toe on right foot
Left 2nd toe tip (LTOETIP)	Anterior point of the second toe on left foot
Right lateral humeral epicondyle (RLATELB)	Most lateral point on the lateral epicondyle of right humerus
Left lateral humeral epicondyle (LLATELB)	Most lateral point on the lateral epicondyle of left humerus
Right medial humeral epicondyle (RMEDELB)	Most medial point on the medial epicondyle of right humerus
Left medial humeral epicondyle (LMEDELB)	Most medial point on the medial epicondyle of left humerus
Right radial styloid (RLATWRIST)	Most distal point of right radius
Left radial styloid (LLATWRIST)	Most distal point of left radius
Right ulnar styloid (RMEDWRIST)	Most distal point of right ulna
Left ulnar styloid (LMEDWRIST)	Most distal point of left ulna
Right 2nd metacarpal head (RHAND2)	Lateral prominent point on the lateral surface of second metacarpal on right hand

Left 2nd metacarpal head (LHAND2)	Lateral prominent point on the lateral surface of second metacarpal on left hand
Right 5th metacarpal head (RHAND5)	Medial prominent point on the medial surface of fifth metacarpal on right hand
Left 5th metacarpal head (LHAND5)	Medial prominent point on the medial surface of fifth metacarpal on left hand
Right 3rd metacarpal head (RHAND3)	A point on the dorsal sulcus between the tip of the third metacarpal (knuckle) and the base of the third finger on right hand.
Left 3rd metacarpal head (LHAND3)	A point on the dorsal sulcus between the tip of the third metacarpal (knuckle) and the base of the third finger on right left.

APPENDIX 2. Virtual marker definitions

Virtual marker location (abbreviation)	**Calculation method (see Appendix 3 for segment reference frame definitions)**
Cervical joint center (V_CJC)	From C7, on a direction forming an angle of 8° in the sagittal plane of head segment with the vector from C7 to STERN at 55 % of the distance between C7 to STERN. *
Thoracic joint center (V_TJC)	From TH12, on a direction forming an angle of -94° in the sagittal plane of thorax segment with the vector from TH12 to TH8 at 52 % of the distance between C7 to STERN. *
Lumbar joint center (V_LJC)	In the pelvis reference plane with origin translated at midpoint between LASIS and RASIS, V_LJC at -33.5 %, 3.2 % and 0 % of the distance between LASIS and RASIS about the anterior-posterior, superior-inferior, and medial-lateral axes, respectively. *
Right hip joint center (V_RHJC)	In the pelvis reference frame with origin translated at midpoint between LASIS and RASIS, V_RHJC at -9.5 %, -37.0 %, and +36.1 % about the anterior-posterior, superior-inferior, and medial-lateral axes, respectively. *
Left hip joint center (V_LHJC)	In the pelvis reference frame with origin translated at midpoint between LASIS and RASIS, V_LHJC at -9.5 %, -37.0 %, and -36.1 % about the anterior-posterior, superior-inferior, and medial-lateral axes, respectively. *
Mid hip (V_MIDHIP)	Midpoint between V_RHJC and V_LHJC. *
Mid trochanter (V_MIDTROC)	Midpoint between RTROC and LTROC. *
Right knee joint center (V_RKJC)	Midpoint between RMEDKNEE and RLATKNEE*
Left knee joint center (V_LKJC)	Midpoint between LMEDKNEE and LLATKNEE*
Right ankle joint center (V_RAJC)	Midpoint between RMEDANK and RLATANK*
Left ankle joint center (V_LAJC)	Midpoint between LMEDANK and LLATANK*
Right glenohumeral joint center (V_RGJC)	From RACRO, on a direction forming an angle of -11° in the sagittal plane of thorax segment with the vector from C7 to STERN at 33 % of the distance between C7 to STERN. *

Left glenohumeral joint center (V_LGJC)	From LACRO, on a direction forming an angle of -11° in the sagittal plane of thorax segment with the vector from C7 to STERN at 33 % of the distance between C7 to STERN. *
Right elbow joint center (V_REJC)	Midpoint between RMEDELB and RLATELB*
Left elbow joint center (V_LEJC)	Midpoint between LMEDELB and LLATELB*
Right wrist joint center (V_RWJC)	Midpoint between RMEDWRIST and RLATWRIST*
Left wrist joint center (V_LWJC)	Midpoint between LMEDWRIST and LLATWRIST*

*Joint center definition from Dumas & Wojtusch (2018)

APPENDIX 3. Segment reference frame definitions

Reference frames for each segment for Dempster (1955), de Leva (1996) and Dumas & Wojtusch (2018). For Dumas & Wojtusch (2018) all three axes are defined, as they are necessary for the calculations of segmental COM positions which do not always lie on longitudinal axis of the segment. For Dempster (1955) and de Leva (1996), only longitudinal axis is defined as the segment COM is assumed to lie on this axis. Longitudinal axis for each segment is Y-axis, except for foot segment where X-axis is the longitudinal axis.

X-axis is anterior-posterior axis, Y-axis is superior-inferior, and Z-axis is medial-lateral axis. The unit vectors $\hat{\boldsymbol{x}}$, $\hat{\boldsymbol{y}}$ and $\hat{\boldsymbol{z}}$ refer to 3D vectors parallel to the X-axis, Y-axis, and Z-axis of the segments, respectively. The segment reference frame definitions are provided for the right-side segments only but they were applied similarly to the left-side segments.

Segment	**Dempster (1955)**	**de Leva (1996)**	**Dumas & Wojtusch (2018)**
Head and neck	Y-axis from V_CJC to VERT. Origin at V_CJC, endpoint VERT.	Assumed Y-axis from V_CJC to VERT. Origin at V_CJC, endpoint VERT. Y-axis is not defined in de Leva (1996), as noted in Dumas & Wojtusch (2018).	Y-axis from V_CJC to VERT. Z-axis normal to plane containing V_CJC, VERT and SEL landmarks, pointing to the right. X-axis is the cross product of $\hat{\boldsymbol{y}}$ and $\hat{\boldsymbol{z}}$. Origin at V_CJC, endpoint VERT.
Trunk	Y-axis from V_MIDTROC to V_CJC. Origin at V_MIDTROC, endpoint V_CJC.	Y-axis from V_MIDHIP to V_CJC. Origin at V_MIDHIP, endpoint V_CJC.	
Thorax			Y-axis from V_TJC to V_CJC. Z-axis normal to plane containing C7, TH12 and STERN landmarks, pointing to the right. X-axis is the cross product of $\hat{\boldsymbol{y}}$ and $\hat{\boldsymbol{z}}$. Origin at V_CJC, endpoint V_TJC.
Abdomen			Y-axis from V_LJC to V_TJC. X-axis and Z-axis same as in pelvis reference frame (no axial rotation assumed). Origin at V_TJC, endpoint V_LJC.
Pelvis			Z-axis from LASIS to RASIS. Y-axis normal to plane containing RASIS, LASIS and mid-point between RPSIS and LPSIS landmarks, pointing superiorly. X-axis is the cross product of $\hat{\boldsymbol{y}}$ and $\hat{\boldsymbol{z}}$. Origin at V_LJC, endpoint V_MIDHIP.

Upper arm	Y-axis from V_REJC to V_RGJC. Origin at V_RGJC, endpoint V_REJC.	Y-axis from V_REJC to V_RGJC. Origin at V_RGJC, endpoint V_REJC.	Y-axis from V_REJC to V_RGJC. X-axis normal to plane containing V_GJC, RMEDELB, and RLATELB, pointing anteriorly. Z-axis is the cross product of $\hat{\boldsymbol{x}}$ and $\hat{\boldsymbol{y}}$ Origin at V_RGJC, endpoint V_REJC.
Forearm		Y-axis from V_RWJC to V_REJC. Origin at V_REJC, endpoint V_RWJC.	Y-axis from V_RWJC to V_REJC. X-axis normal to plane containing V_REJC, RMEDWRIST and RLATWRIST, pointing anteriorly. Z-axis is the cross product of $\hat{\boldsymbol{x}}$ and $\hat{\boldsymbol{y}}$. Origin at V_REJC, endpoint V_RWJC.
Forearm and hand	Y-axis from V_RWJC to V_REJC. Origin at V_REJC, endpoint V_RWJC.		
Hand		Assumed Y-axis from RHAND3 to V_RWJC. Origin at V_RWJC, endpoint V_RHAND3. Y-axis is not defined in de Leva (1996), as noted in Dumas & Wojtusch (2018).	Y-axis from midpoint between RHAND2 and RHAND5 to R_WJC. X-axis normal to plane containing RHAND2, RHAND5, and V_RWJC landmarks, pointing anteriorly. Z-axis is the cross product of $\hat{\boldsymbol{x}}$ and $\hat{\boldsymbol{y}}$**.** Origin at V_RWJC, endpoint between RHAND2 and RHAND5.
Thigh	Y-axis from V_RKJC to RTROC. Origin at RTROC, endpoint V_RKJC.	Y-axis from V_RKJC to V_RHJC. Origin at V_RHJC, endpoint V_RKJC.	Y-axis from V_RKJC to V_RHJC. X-axis normal to plane containing V_RHJC, RMEDKNEE, and RLATKNEE landmarks, pointing anteriorly. Z-axis is the cross product of $\hat{\boldsymbol{x}}$ and $\hat{\boldsymbol{y}}$. Origin at V_RHJC, endpoint V_RKJC.
Shank	Y-axis from V_RAJC to V_RKJC. Origin at V_RKJC, endpoint V_RAJC.	Y-axis from V_RAJC to V_RKJC. Origin at V_RKJC, endpoint V_RAJC.	Y-axis from V_RAJC to V_RKJC. Origin at V_RKJC. X-axis normal to plane containing RMEDKNEE, RLATKNEE, and V_RAJC landmarks pointing anteriorly. Z-axis is the cross product of $\hat{\boldsymbol{x}}$ and $\hat{\boldsymbol{y}}$. Origin at V_RKJC, endpoint V_RAJC. Note that no axial rotation between thigh and shank is assumed in this study, and fibula head landmarks are not used.
Foot	X-axis from RHEEL to RTOETIP. Origin at RHEEL, endpoint RTOETIP.	X-axis from RHEEL to RTOETIP. Origin at RHEEL, endpoint RTOETIP. Note that tip of 2nd toe skin landmark is used instead of tip of longest toe skin landmark as defined in de Leva (1996).	X-axis from RHEEL to midpoint between RMET1 and RMET5 landmarks. Y-axis normal to plane containing RMET1, RMET5 and RHEEL landmarks, pointing superiorly. Z-axis is the cross product of $\hat{\boldsymbol{x}}$ and $\hat{\boldsymbol{y}}$. Origin at V_RAJC, endpoint midpoint between RMET1 and RMET5 landmarks.

APPENDIX 3. WBAM calculation methods

COM calculations. For DEM and LEV models, the 3D position of COM of each segment in GCS was calculated as follows:

$$COM_s = O_s + L_s COM_y \hat{y}$$

where COM_s is the position of the segment's COM in GCS, O_s is the origin of the segment in GCS, L_s is the length of the segment (Euclidean distance between segments origin and end-point), COM_y is the segment's COM position relative to segment's length, and $\hat{y}$ is the unit vector in the direction of the longitudinal axis of the segment in GCS (see appendix 3).

For the calculation of segment COM position for DUM model, rotation matrices, R_s, where first formed to describe the orientation of the segment in GCS for each segment based on the X-, Y-, and Z-axes of the segments in following manner:

$$R_s = \begin{bmatrix} \hat{x}_x & \hat{y}_x & \hat{z}_x \\ \hat{x}_y & \hat{y}_y & \hat{z}_y \\ \hat{x}_z & \hat{y}_z & \hat{z}_z \end{bmatrix}$$

where the elements in first row represent the X-components of the unit vectors parallel to the X-, Y-, and Z-axes of the segment, respectively, projected in GCS. Similarly, second row represents the Y-components, and third row the Z-components of these unit vectors. Segment COM position in segment reference frame, COM_{ref}, was obtained from:

$$COM_{ref} = [COM_x L_s, COM_y L_s, COM_z L_s]$$

where COM_x, COM_y, and COM_z are the COM position X, Y, and Z values relative to segment length in segment reference frame. And finally segments COM position in GCS, COM_s,was calculated as:

$$COM_s = O_s + R_s COM_{ref}$$

For left side segments the Z-axis was mirrored to account for that the Z-axis points medio-laterally for right side segments and latero-medially for left side segments. To account for this, following formula was used for left side segments:

$$COM_s = O_s + SR_s S' COM_{ref}$$

where *S* is a symmetry matrix:

$$S = \begin{bmatrix} 1 & 0 & 0 \\ 0 & 1 & 0 \\ 0 & 0 & -1 \end{bmatrix}$$

and S' is the transpose of *S*. Segment mass, m_s was for all BSIP models was calculated as $m_s = p_s M$, where p_s is the percentage of the total body mass *M*. Three dimensional total body COM, *COM*, in GCS for all models was then obtained by calculating the weighted average of the segments with the following equation:

$$COM = \frac{\sum_{s=1}^{n} m_{s_i} COM_{s_i}}{\sum_{s=1}^{n} m_{s_i}}$$

where n is the number of segments, m_{s_i} is the mass of the segment *i* in kg, COM_{s_i} is the COM position of the segment *i* in GCS.

Calculation of kinematic method WBAM with the single plane assumption. The velocity of each segment in GCS sagittal plane (X, Y) for a given frame was calculated using finite difference calculus:

$$v_s = \frac{s_{i+1} - s_{i-1}}{2(\Delta t)}$$

In this formula, v_s denotes the velocity components in the X and Y directions of the segment's COM. The terms s_{i+1} and s_{i-1} refer to the COM's position components in the X and Y directions at frames *i+1* and *i -1*, respectively, and *i* refers to the frame the value is calculated at. The term

Δt represents the time interval between frames, which was 200^{-1} s in this study. Angular velocity about COM in sagittal plane for each segment was calculated using formula:

$$\omega_s = \frac{\theta_{i+1} - \theta_{i-1}}{2(\Delta t)}$$

where ω_s represents the sagittal plane angular velocity of the segment in frame *i*, while θ_{i+1} and θ_{i-1} are the sagittal plane angular positions of the segment's longitudinal axis in frames *i+1* and *i*-1, respectively. Centroidal moment of inertia for rotations about the center of gravity, I_{cg}, for each segment was calculated in the sagittal plane using equations described in (7) and (8). Z-axis K_{cg} values presented in table 3 were used, and length of segment was calculated as the distance between segments origin and endpoint projections in the sagittal plane. The kinematics based sagittal plane WBAM values for DEM, LEV, and DUM models were then calculated for each frame using equation described in chapter 3 equation 3:

$$L_k = \sum_{s=1}^{n} I_s \omega_s + [\vec{r_s} \times m_s \vec{v_s}]$$

Testing the single plane movement assumption. The single plane assumption proposed that all movements occurred exclusively within the sagittal plane, with the body segments arranged such that their primary axis of rotation was along the Z-axis. To verify this, a detailed analysis for the DUM model was conducted, where the actual orientations of the segments in GCS were considered. Angular velocities of the segments were calculated in three dimensions, and inertia tensors were considered in their true orientation, rather than assuming a simplified alignment of rotation along the Z-axis. Complete 3x3 moment of inertia tensors, $\bar{I}$, for the segments were formed from the data in table 3 in following format:

$$\bar{I} = \begin{bmatrix} I_x & P_{xy} & P_{xz} \\ & I_y & P_{YZ} \\ sym. & & I_z \end{bmatrix}$$

where I_x, I_y, and I_z are the K_{cg} values from table 3, and P_{xy}, P_{xz}, and P_{yz} are the sagittal, transverse, and frontal products of inertia from table 3. Three-dimensional angular velocity (3x1 vector), ω_{3d}, at frame *i* was calculated by differentiating the rotation matrix using finite difference.

Rotation matrix describing segments rotation from frame i-1 to frame i+1, ΔR, was calculated by multiplying rotation matrix of the segment in frame i+1 by the transpose of rotation matrix in frame i-1. From there, ω_{3d} was obtained using by:

$$|\omega_{3d}| = \frac{\delta}{2\Delta t}$$

where:

$$\delta = cos^{-1}\left(\frac{\Delta R_{11} + \Delta R_{22} + \Delta R_{33} - 1}{2}\right)$$

Axis of rotation, $\hat{v}$, was obtained by from:

$$\hat{v} = \frac{\begin{bmatrix}\Delta R_{32} - \Delta R_{23} \\ \Delta R_{13} - \Delta R_{31} \\ \Delta R_{21} - \Delta R_{12}\end{bmatrix}}{2sin\delta}$$

And finally, angular velocity was calculated as:

$$\omega_{3d} = |\omega_{3d}|\hat{v}$$

Inertia tensors of segments were rotated in each frame to the GCS frame to match segments orientation by following equation:

$$\bar{I}_{gcs} = R\bar{I}R'$$

where $\bar{I}_{gcs}$ is the segments inertia tensors in GCS, R is the rotation matrix of the segment, and R' is the transpose of the rotation matrix R. For the left side segment rotated inertia tensor was defined as:

$$\bar{I}_{gcs} = RS\bar{I}S'R'$$

From here, three-dimensional angular momentum was calculated again according to chapter 3 equation 3 where $\bar{I}_{gcs}$ and ω_{3d} values were used in local term for each segment:

$$L_{k3d} = \sum_{s=1}^{S} \bar{I}_{gcs}\, \omega_{3d} + [\vec{r}_s \times m_s \vec{v}_s]$$

from which only scalar components of the sagittal plane were considered.